

Electrochemistry of large bandgap chemically resistant semiconductors

Electrochemistry of large bandgap chemically resistant semiconductors

**Electrochemie van grote bandgap
chemisch bestendige halfgeleiders**

(met een samenvatting in het Nederlands)

PROEFSCHRIFT

TER VERKRIJGING VAN DE GRAAD VAN DOCTOR AAN DE
UNIVERSITEIT UTRECHT OP GEZAG VAN DE RECTOR
MAGNIFICUS, PROF. DR. H. O. VOORMA, INGEVOLGE HET
BESLUIT VAN HET COLLEGE VOOR PROMOTIES IN HET
OPENBAAR TE VERDEDIGEN OP MAANDAG 7 SEPTEMBER
1998 DES MORGENS TE 10.30 UUR

DOOR

JAO VAN DE LAGEMAAT

GEBOREN OP 8 MEI 1972 TE SCHOONHOVEN

PROMOTOR: Prof. Dr. J.J. Kelly
CO-PROMOTOR: Dr. D. Vanmaekelbergh

Faculteit Scheikunde
Universiteit Utrecht

CIP-GEGEVENS KONINKLIJKE BIBLIOTHEEK, DEN HAAG

Lagemaat, Jao van de

Electrochemistry of large bandgap chemically resistant semiconductors
Jao van de Lagemaat. - Utrecht : Universiteit Utrecht,
Faculteit Scheikunde, Debye Instituut
Proefschrift Universiteit Utrecht. Met samenvatting in het Nederlands.
ISBN 90-393-1687-2

*"Your poem must eternal be,
Dear sir! it cannot fail,
For 'tis incomprehensible,
And without head or tail."*

comment on the Ancient Mariner,
S.T. Coleridge

Aan Ris

The work described in this thesis was supported by the Netherlands Foundation for Chemical Research (SON), with financial aid from the Netherlands Organization for Scientific Research (NWO).

Contents

1	Introduction	9
1.1	Materials	10
1.2	Photoelectrochemistry of large bandgap semiconductors	13
1.2.1	Double layers at the semiconductor/electrolyte interface . .	13
1.2.2	Electron transfer	16
1.2.3	Interaction with light: the dead layer model	20
1.3	Outline of this thesis	23
	References	24
2	Electrochemistry of homoepitaxial CVD diamond. Part I	29
2.1	Introduction	30
2.2	Experimental	32
2.3	Results and Discussion	34
2.3.1	The interfacial capacitance	34
2.3.2	Current-potential characteristics in indifferent electrolyte solution	37
2.3.3	Electrochemical processes with simple redox systems	38
2.4	Conclusions	42
	References	42
3	Electrochemistry of homoepitaxial CVD diamond. Part II	45
3.1	Introduction	46
3.2	Results	47
3.3	Discussion	50
3.4	Conclusions	55
	Appendix A: Calculation of the Electrochemical Impedance	57
	References	63
4	Photoelectrochemical characterization of 6H-SiC	65
4.1	Introduction	66
4.2	Experimental	68
4.3	Results and Discussion	69

4.3.1	Electrical Impedance Spectroscopy	69
4.3.2	Photoelectrochemical measurements	73
4.3.3	IMPS-Measurements	74
4.3.4	Photocurrent quantum yield	76
4.4	Conclusions	79
	References	80
5	Photoelectrochemistry of porous 6H-SiC	83
5.1	Introduction	84
5.2	Experimental	84
5.3	Results	85
5.4	Discussion	88
5.5	Conclusions	91
	References	91
6	Excitonic effects in the photoluminescence of GaN studied at the semi-conductor/electrolyte interface	93
6.1	Introduction	94
6.2	Experimental	95
6.3	Photoluminescence characterization of the GaN samples	97
6.4	Photoelectrochemical characterization of the GaN/electrolyte interface	99
6.5	Excitonic effects in the luminescence of GaN electrodes	104
6.6	Conclusions	110
	Appendix: porous GaN	111
	References	113
	Samenvatting	115
	List of publications	119
	Tenslotte	121
	Curriculum Vitae	127

Chapter 1

Introduction

Devices made from semiconductors have had an enormous influence on the development of society in the last decades. Silicon based microprocessors are found in a wide variety of home appliances (microwave ovens, TVs, washing machines etc.), in cars, cellular phones and many more. The most striking example of the semiconductor “revolution” is, of course, the personal computer. Increasing miniaturization of logic circuits has made possible PCs that are as powerful as the supercomputers of ten years ago. Another very important application of semiconductors is in solar energy conversion. There is a considerable drive to replace fossil fuel by cleaner alternatives, that can be found in semiconductor based solar cells.

Despite the enormous variety of its applications, silicon has its disadvantages. Its small indirect bandgap (1.1 eV) makes it unsuitable for light emitting devices and operation at high temperatures. It is also prone to chemical attack. Better materials are needed for devices that operate in aggressive environments. Recent advances in crystal growth techniques have made available a number of wide bandgap semiconductors that are chemically very stable, like diamond, silicon carbide (SiC), III-V nitrides (GaN, AlN, InN) and transition metal oxides (TiO₂, ZnO). Already, a CCD (Charge Coupled Device) has been demonstrated in SiC [1]. NASA has reported a SiC based rectifier diode that operates at 600 °C [2]. For some time now, blue light emitting diodes based on SiC have been commercially available. One of the most promising applications for diamond appears to be as

cold cathode in flat panel displays [3, 4]. The III-V nitrides offer the possibility of making stable blue and UV diode lasers.

The chemical stability of these materials, while an advantage for device operation, makes processing (cleaning, etching, polishing and metallization) difficult. Clearly, more information on the physical properties and surface chemistry of these materials is needed. This thesis describes a broad (photo)electrochemical study of such topics for three large bandgap chemically resistant semiconductors: diamond, silicon carbide and gallium nitride, with bandgaps of 5.54, 3.02, and 3.41 eV respectively.

1.1 Materials

Diamond

The title of the famous James Bond movie “*Diamonds are forever*” is a little misleading. Given enough time, diamond will transform into a thermodynamically more stable allotrope of carbon (graphite). Fortunately, the time this takes at room temperature is estimated to be 10^{90} years [5]. Diamond is well known for its material properties. It is extremely hard, has a very high thermal conductivity ($2600 \text{ W m}^{-1} \text{ K}^{-1}$ [6]) and is, in pure form, optically transparent. In its undoped form, it is an excellent insulator with a bandgap of 5.54 eV. Because of its hardness, diamond is used traditionally as an abrasive agent. Since the discovery of CVD diamond [7], many more applications are possible such as heat sinks in electronics, wear resistant layers on tools and anti-corrosion layers on metals [8, 9].

Charge carriers in diamond are known to have high mobilities, for electrons : $1800 \text{ cm}^2 \text{ V}^{-1} \text{ s}^{-1}$, and holes $1200 \text{ cm}^2 \text{ V}^{-1} \text{ s}^{-1}$ [10] (compare these values to the mobilities in silicon: 1300 and 500 respectively). Consequently, high speed electronic devices are being considered. Devices utilizing diamond could potentially be operated at high temperature, in corrosive media and in radioactive environments [11]. Furthermore, the observation of negative electron affinity (NEA) of specially pretreated surfaces [3, 4, 12–14], makes diamond an excellent choice as electron emitter in flat-panel displays.

There is a growing interest in the electrochemical properties of diamond [9, 11, 12, 15–30] which may prove important in industrial applications, for instance for electroanalytical or electrosynthetic purposes [9, 11, 17, 20, 21, 23, 24]. Diamond is also an interesting electrode material for more fundamental re-

search, including the study of electron transfer processes. In contrast to many semiconductors and metals, it does not form an interfacial (oxide) layer when brought into contact with an aqueous solution. Moreover, it does not dissolve anodically or cathodically. Most of the results reported so far deal with polycrystalline diamond electrodes of widely varying quality and with moderate or high acceptor concentration. It has been found that, while a depletion layer is present at the diamond/electrolyte interface [11, 15, 19, 23, 27–30] and diamond has a huge bandgap, current-voltage curves in aqueous solutions of simple (one-electron) redox systems appear metallic [9, 11, 16, 20, 23–26]. This is an intriguing result, since diode characteristics are expected under these conditions.

Silicon carbide

The use of silicon carbide (SiC) as a semiconductor can be traced back to 1907, when scientists from the Marconi company observed electroluminescence from the material [31, 32]. However, it was not until 1955, when Lely devised a growth process with which he obtained (for the first time) pure SiC crystals [33], that research began to thrive, with a boom in the last decade.

SiC is the only chemically stable form of silicon and carbon [32]. Crystalline SiC can be seen as a close-packed stacking of double layers of Si and C atoms. Each Si or C atom is surrounded by four C or Si atoms arranged in a tetrahedron. The simplest forms are hexagonal wurtzite (AB stacking of the double layers), and cubic zinc blende (ABC stacking). There are about 50 known stacking sequences [10] called polytypes. For example, the polytype known as 393R (rhombohedral symmetry) has a primitive cell with $a = 3.079 \text{ \AA}$ and $c = 989.6 \text{ \AA}$. The most common polytypes are 6H (stacking ABCACB), 4H (ABAC) and 3C (ABC). Because of this wide variety of crystal structures, SiC is deemed a classic example of polytypism.

Many applications have been proposed for SiC, and some have been realized, e.g. UV detectors, ultrafast electronics (a joint research project of Motorola Inc. and Cree Research Inc. yielded FETs made of SiC with operation frequencies of 12.6 GHz [32]), light emitting diodes in the blue (these are even commercially available [34]), radiation hard electronics and X-ray masks. Devices made of SiC are suitable for high temperature applications, and for operation in nuclear reactors and deep space [35]. SiC is an excellent substrate for epitaxial growth of III-V nitrides [36, 37].

Research on the photoelectrochemistry of SiC has focussed mainly on photocatalysis [38, 39], water splitting [40, 41], photoetching of microstructures [42–44], chemomechanical polishing [45], and fundamental studies of electron exchange reactions [46]. Because of the possible application in microelectronics, there is a need for etching methods for SiC [39, 47, 48]; to date, no open circuit wet-chemical method is known [32]. Shor et al. showed that, using appropriate masking techniques and laser illumination, *n*-type SiC can be etched photoanodically yielding microstructures suitable for electronic applications [42]. The same authors and others showed, that by (photo)anodic etching in HF solutions, SiC can be made highly porous, and that, as a result, the photoluminescence intensity of the material improves by orders of magnitude [49–51].

Gallium nitride

Although GaN was grown in the 1960s, it is only in the past few years that high quality material has become available. Previously, GaN was “cursed” with high background carrier concentrations and stress caused by the substrate [36]. Also *p*-type doping could not be achieved. At present, good quality material can be grown using MBE (Molecular Beam Epitaxy), and MOVPE (Metal Organic Vapor Phase Epitaxy). Like SiC, GaN can crystallize in many polytypes. The 2H (wurtzite) and the 3C (zinc blende) forms are those most commonly observed.

GaN shares many excellent material properties with diamond and SiC. Devices made of GaN are expected to be radiation hard, chemically and physically stable, and suitable for high power operation [36]. Light emitting GaN diodes were demonstrated already in 1970 [52, 53]. Recently, a “stable” UV laser diode based on GaN that operated for up to 6 hours at room temperature at 17 mW has been reported [54]. Blue and UV lasers are essential for the next generation of information storage media.

Since the material is relatively new, there has not been much research on the photoelectrochemistry of GaN. As for diamond and SiC, no open circuit wet chemical etching method is known. A few authors have tried to photoetch GaN with UV light [55–58]. In general, highly anisotropic etching with μm sized features can be obtained. Kocha *et al.* [59] have conducted a fairly complete photoelectrochemical investigation of GaN. They showed that the pH dependence of the flat band potential is close to Nernstian (60mV/unit pH), indicating the presence of an oxide layer at the surface. The photocurrent spectrum was also measured, yielding a bandgap energy as expected from other experiments.

1.2 Photoelectrochemistry of large bandgap semiconductors

The brief discussion of the semiconductor/electrolyte interface, given in this section, is aimed at providing the background needed to understand the other chapters in this thesis. In section 1.2.1 the potential distribution at the interface is discussed. In section 1.2.2 it is shown how charge is exchanged between a semiconductor and an electrolyte solution. Section 1.2.3 includes the fundamentals of the interaction of the semiconductor/electrolyte interface with light. More elaborate texts are available on these topics [60].

1.2.1 Double layers at the semiconductor/electrolyte interface

When a solid is brought into contact with a solution, the electrochemical potential of the electrons in the two phases is generally different. Electron exchange occurs across the interface until, at equilibrium, the Fermi level in both phases is the same. The Fermi level in solution is related to the redox potential. Such electron exchange leads to the formation of an electrical double layer both in the solid and in solution [61]. Fig 1.1 shows a majority carrier depletion layer within the semiconductor and the Helmholtz and Gouy layers in solution. The latter two are also present at metal/electrolyte interfaces. The Helmholtz layer is essentially the region between the plane of closest approach for ions from the solution to the surface and the semiconductor surface. Since the thickness of this layer is typically of the order of a few Å and the potential drop over it is of the order of 0.1 to 1V, the electric field is very large ($\approx 10^9$ V/m). The potential drop is directly proportional to the surface charge. This surface charge can be caused by both adsorbed protons or hydroxyl ions (in the case of aqueous solutions) or charge stored in surface states.

The Gouy layer is located outside the Helmholtz layer, in the electrolyte. It is a region in which the concentrations of anions and cations differ from their bulk values. At electrolyte concentrations above 0.1 M, the thickness of this layer is only a few Å so that the Gouy layer will be indistinguishable from the Helmholtz double layer [60]. Because of this, it is generally not considered.

The majority carrier depletion region, is a region in which a space charge exists because of ionized donor ions (in the case of *n*-type semiconductors) or acceptor ions (*p*-type semiconductors). Because of the electric field, the concentration of majority carriers is considerably lower than that in the bulk phase.

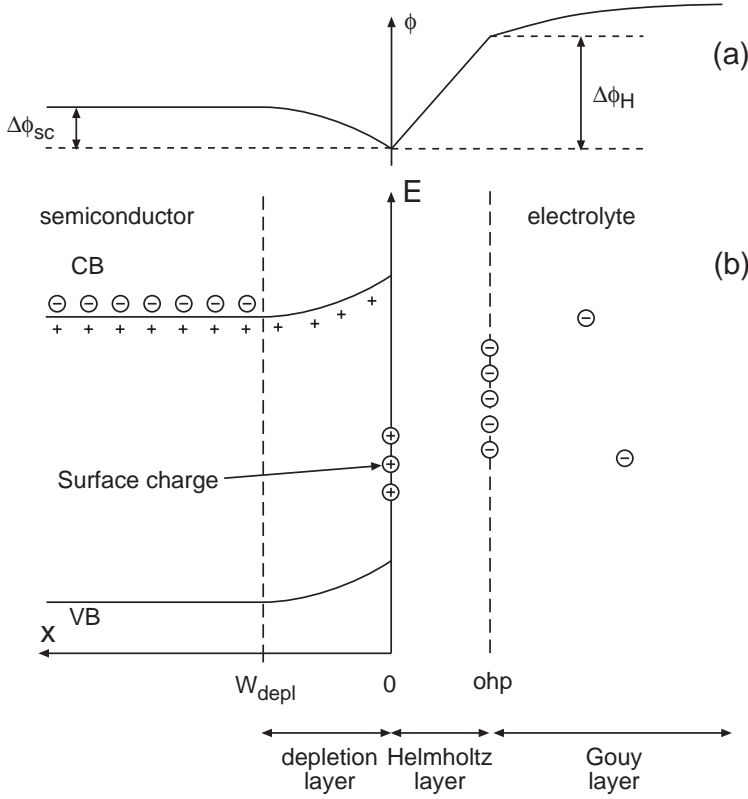


FIGURE 1.1. Overview of the semiconductor/electrolyte interface for a solution with a low electrolyte concentration. The situation is sketched for an n -type semiconductor. (a) potential distribution (b) band diagram. The Helmholtz and Gouy layers are not drawn to scale.

It is illustrative to calculate the thickness of the depletion layer (W_{depl}). From the Poisson equation and using Fermi statistics we obtain (for an n -type semiconductor):

$$\Delta\phi_{sc} - \frac{k_B T}{e} = \frac{e N_{sc}}{2\epsilon\epsilon_0} (W_{depl})^2 \quad (1.1)$$

where $\Delta\phi_{sc}$ is the potential drop over the depletion layer, N_{sc} is the density of ionized dopant atoms and $\epsilon\epsilon_0$ is the dielectric constant of the semiconductor. From this equation we can calculate the width of a typical depletion layer to be around 100 nm, for a moderately doped semiconductor ($\approx 10^{17} \text{ cm}^{-3}$).

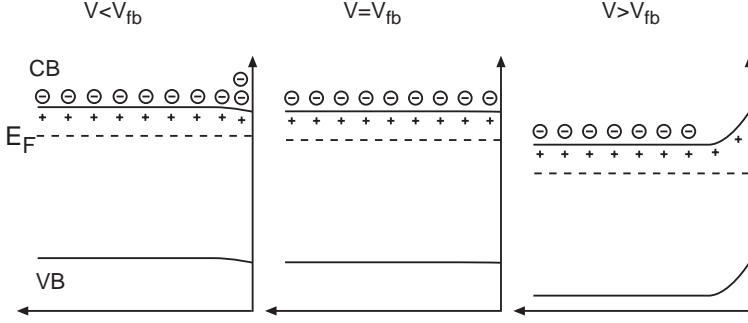


FIGURE 1.2. Typical situations occurring at the n -type semiconductor/electrolyte interface. Since the capacitance of the depletion layer is much smaller than that of the Helmholtz layer, the energetic positions of the bands at the surface are effectively fixed. A change in potential leads to a change of the bulk Fermi level. Three situations are shown. When $V > V_{fb}$, a depletion layer is observed inside the semiconductor. When $V = V_{fb}$, the electrode is in the flat band condition. When $V < V_{fb}$, an accumulation region will be formed. Electrons will be effectively driven to the surface. The properties of the accumulation layer will not be discussed in this thesis.

This space charge region (like every double layer) has an associated capacitance $C_{sc} = \frac{dQ}{d\Delta\phi_{sc}}$.

$$C_{sc} = \frac{dQ}{d\Delta\phi_{sc}} = eN_{sc} \frac{dW_{depl}}{d\Delta\phi_{sc}} = \sqrt{\frac{e\epsilon\epsilon_0 N_{sc}}{2}} \left(\Delta\phi_{sc} - \frac{k_B T}{e} \right)^{-1/2} \quad (1.2)$$

This relationship is known as the Mott-Schottky equation, and relates the capacitance of the depletion layer to the potential drop across the layer [60].

A change in the electrode potential results in a change of the potential drop over the semiconductor/electrolyte interface which is distributed over the solid phase (depletion layer) and the Helmholtz layer in a ratio determined by the relative capacitances of these layers. The capacitance of the Helmholtz layer is generally much larger than that of the depletion layer ($C_H \approx 10^{-5} \text{ Fcm}^{-2}$, $C_{sc} \approx 10^{-8} \text{ Fcm}^{-2}$). In the ideal case almost all of the potential change will occur inside the semiconductor. The electrode potential at which $\Delta\phi_{sc} = 0$ is called the flat-band potential (V_{fb}). This means that we can write $\Delta\phi_{sc}$ as $V - V_{fb}$.

Equation 1.1 can thus be written as:

$$W_{depl} = \sqrt{\frac{2\epsilon\epsilon_0}{eN_{sc}}(V - V_{fb} - k_B T/e)} \quad (1.3)$$

and equation 1.2 becomes:

$$C_{sc}^{-2} = \frac{e\epsilon\epsilon_0 N_{sc}}{2} (V - V_{fb} - k_B T/e) \quad (1.4)$$

From a plot of C_{sc}^{-2} vs V we can determine the doping density of the semiconductor, and V_{fb} ; various examples are discussed throughout this thesis (Figs. 2.2, 2.3, 4.1, 4.2, 5.3, and 6.5).

Although equation 1.4 is often obeyed, there are situations in which the observed capacitance-potential plot may differ markedly from that predicted by theory. In some cases, charging of surface states can occur. This may lead to considerable changes in the Helmholtz potential. Deviations from equation 1.4 may also occur when the density of donor (or acceptor) ions in the semiconductor is so large that the depletion layer capacitance becomes comparable to the Helmholtz capacitance. In this case the slope of a (C_p^{-2}, V) -plot will still be linear and show the correct doping density, but the x -axis intercept is shifted by an amount $\frac{\epsilon\epsilon_0 e N_{sc}}{2C_H^2}$ [62]. This shift is normally negligibly low, but can be substantial if the semiconductor has a high dielectric constant (for example TiO_2).

Figure 1.2 shows some situations that can occur at the semiconductor electrolyte interface. The properties of the accumulation layer will not be discussed in this thesis

1.2.2 Electron transfer

In this section electron transfer between the semiconductor and a redox couple in solution is considered. We will discuss two important cases: direct exchange with one of the bands, and exchange mediated by surface states. For more information, the reader is referred to a series of papers by Vanmaekelbergh [63, 64].

According to the fluctuating energy level model as developed by Gerischer [65–67], the redox couple is described by Gaussian distributions of electron energy states, the empty and filled states corresponding to the oxidised and reduced species, respectively (see Fig. 1.3). The distribution of electron energy levels around the two most probable states E_{Red} and E_{Ox} is caused by temporal fluctuations in the surroundings of the redox ion. The densities of states of the reduced and the oxidised form of the redox couple are given by [60]:

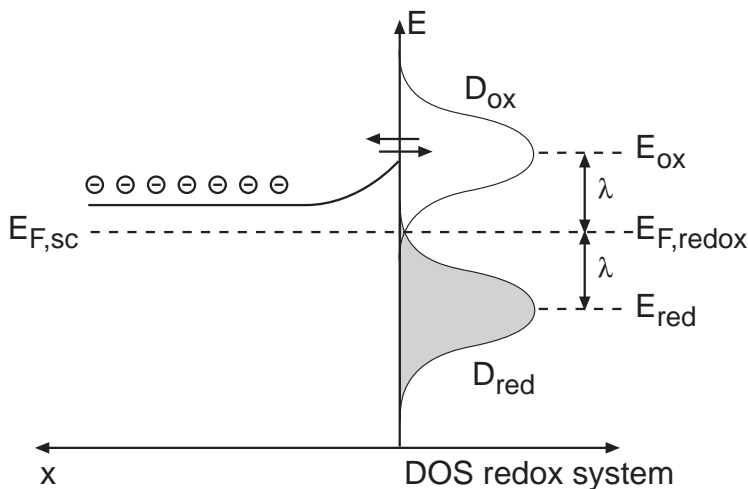


FIGURE 1.3. Direct exchange of electrons between the conduction band of an n -type semiconductor and a redox couple. Exchange occurs at energies above the conduction band edge at the surface. The reduced form injects electrons into the conduction band, the oxidised form is reduced by surface electrons. For the case shown the semiconductor is in equilibrium with the redox-couple, so that their Fermi-levels are the same.

$$D_{red}(E) = c_{red} \frac{1}{\sqrt{4\pi k_B T \lambda}} \exp \left(-\frac{[E - E_{red}]^2}{4k_B T \lambda} \right) \quad (1.5)$$

$$D_{ox}(E) = c_{ox} \frac{1}{\sqrt{4\pi k_B T \lambda}} \exp \left(-\frac{[E - E_{ox}]^2}{4k_B T \lambda} \right) \quad (1.6)$$

λ in this equation is the reorganization energy of the redox couple ($(E_{ox} - E_{red})/2 = \lambda$). $(E_{ox} + E_{red})/2$ is the Fermi energy of the redox system $E_{F,redox}$ at equal concentrations of reduced and oxidised forms (c_{red} and c_{ox} , respectively).

direct exchange

Direct exchange occurs when electrons tunnel directly between energy levels in the redox system and states in the conduction or the valence band of the semiconductor. Figure 1.3 shows a typical case of an n -type semiconductor. Electrons are only exchanged at energies above the conduction band edge at the surface ($E_{C,s}$).

The current-voltage relationship can be derived from the model in a very simple way. Consider the two exchange reactions:



k_{red} , and k_{ox} are rate constants which depend on the properties of the redox system and the potential drop over the Helmholtz-layer. If a change of the electrode potential results in a change of the band bending only, k_{red} , and k_{ox} can be taken as constants, independent of V .

The total current is:

$$j = j_{red} + j_{ox} = -ek_{red}c_{ox}n_s + ek_{ox}c_{red} \quad (1.9)$$

in which n_s , the surface concentration of electrons, is related to the bulk concentration n_b by $n_s = n_b \exp(-\frac{e\Delta\phi_{sc}}{k_B T})$. At equilibrium $j_{ox} = -j_{red}$ so that we can define an exchange current density $j_{exc} = j_{ox,eq} = -j_{red,eq}$. If we assume that a change of the electrode potential only changes $\Delta\phi_{sc}$, the only potential dependent variable is n_s , so the current will become:

$$j = j_{eq} \left[1 - \exp\left(-\frac{e(V - V_{eq})}{k_B T}\right) \right] \quad (1.10)$$

Note that this is the same equation as is found for the current through a semiconductor/metal Schottky junction [68]. It predicts that at potentials negative of the equilibrium potential, the current will be negative and vary exponentially with potential, and that positive of V_{eq} the current will be positive and independent of electrode potential. Deviations from equation 1.10 are expected when part of the potential drop occurs inside the depletion layer. In this case the current at positive potentials will depend on potential. A thorough analysis of the expected current-voltage plots can be found in Ref. [63].

Surface state mediated exchange

When the difference between $E_{F,redox}$ and $E_{C,s}$ (the conduction band edge at the surface) is so large that the energetic overlap between states in the conduction

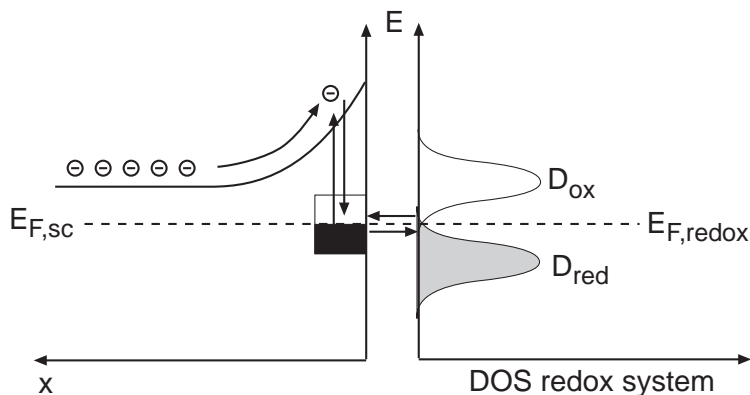


FIGURE 1.4. Mediation of electron transfer by surface states. The arrows indicate the direction of electron transfer.

band and states in the redox system is low, the fluctuating energy level model predicts that the exchange current will be very small. Surprisingly, this is almost never observed. In this case, transfer of electrons can be mediated by surface states that are in equilibrium with the majority carrier band, and with the redox system [63, 69, 70]. It can be shown that for a surface state density of 10^{10} cm^{-2} surface state mediated transfer dominates over direct exchange if $E_{F,redox}$ is only 0.25 eV below $E_{C,s}$ [63]. Since the charge of the surface state depends on the kinetics of the various processes involved in filling and emptying the states, part of an applied potential drop will fall inside the Helmholtz layer. Because of this, the bandedges at the surface shift with respect to the levels of the redox system as a function of potential. This severely complicates the calculation of the current-voltage relationship. Since this text is only introductory, we will not attempt this, and refer the reader to Ref. [63] for a complete analysis.

It is possible to distinguish between a surface state mediated mechanism and a direct mechanism via electrical impedance measurements [60, 71]. Van-maekelbergh calculated the impedance response due to surface state mediated electron transfer [64]. The expected impedance scheme is shown in fig. 1.5b. Fig. 1.5a shows the scheme for direct exchange. In chapter 3 this result is used for the analysis of the impedance of diamond electrodes in solutions of redox systems.

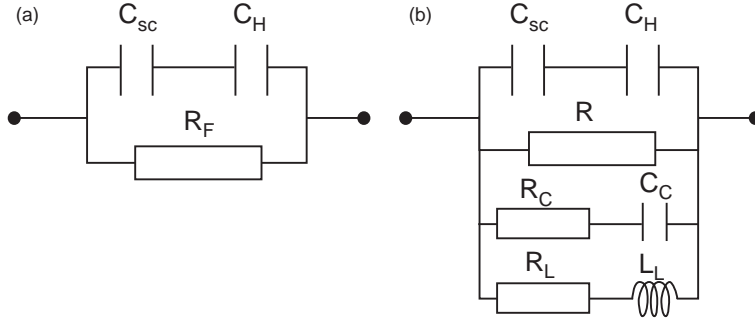


FIGURE 1.5. (a): Impedance scheme expected for direct exchange. (b) Impedance scheme expected for surface state mediated exchange. The $R_C C_C$, and $R_L L_L$ branches are caused by relaxation of the electron occupation in surface states and have the same time constants.

1.2.3 Interaction with light: the dead layer model

In this section we deal with the absorption of light by the semiconductor/electrolyte interface region and calculate the resulting photocurrent and the photoluminescence intensity.

Figure 1.6 shows an n -type semiconductor/electrolyte interface, illuminated from the electrolyte side. When the photons are of high enough energy, electrons from the valence band can be promoted to the conduction band, yielding a free electron and hole. The optical generation rate of free electrons and holes at a depth x is given by $-d\phi/dx$ where $\phi(x) = \phi(0) \exp(-\alpha x)$ (The Lambert-Beer law); $\phi(0)$ is the photon flux at the surface ($x = 0$) corrected for reflection, $\phi(x)$ is the flux at depth x and α is the absorption coefficient. The penetration depth of the light is given by $1/\alpha$. We can distinguish two processes that contribute to charge separation. Electron-hole pairs, created within the depletion layer, are separated by the strong electric field (typically 10^7 V m^{-1}). The minority carriers (holes) migrate to the surface, the majority carriers to the bulk of the semiconductor; this occurs extremely fast, on a ps time scale [72, 73]. To calculate the photocurrent quantum yield, the width of the space charge layer W_{depl} , determined by the band bending $V - V_{fb}$ (see equation 1.3), will be important. Because of the effective charge separation within the depletion layer, the concentration of minority carriers at the bulk edge of this layer is low. Minority carriers that are generated within a diffusion length L_p of the edge can reach the depletion layer by diffusion

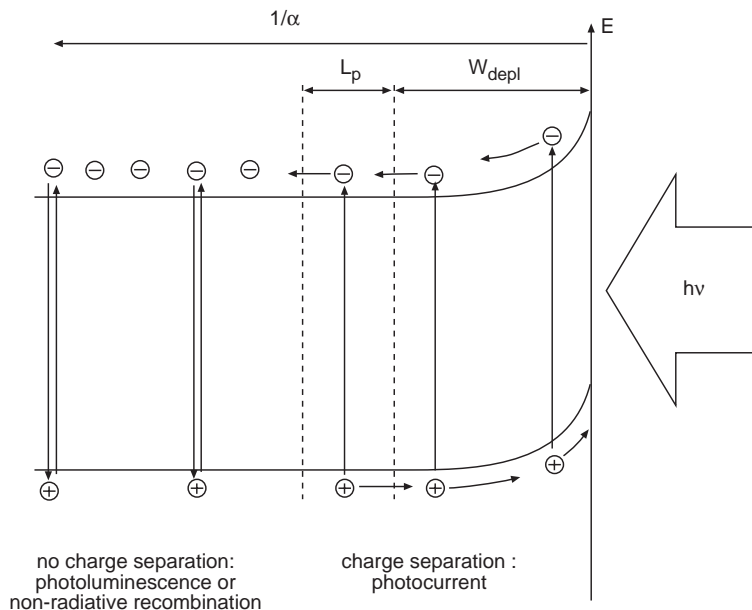


FIGURE 1.6. Charge separation at the *n*-type semiconductor/electrolyte interface. Electron-hole pairs generated within the depletion layer (thickness W_{depl}) and in the diffusion layer for minority carriers (thickness L_p) are separated by the electric field or by diffusion and cause a photocurrent. Electron-hole pairs generated deeper inside the semiconductor recombine either radiatively or non-radiatively.

and so contribute to the current. L_p is related to the minority carrier lifetime τ by $L_p = \sqrt{D_p \tau}$. D_p is the diffusion constant of the minority carriers given by the Einstein equation: $D_p = \mu_p \frac{k_B T}{e}$, in which μ_p is their mobility. The distance $W = W_{depl} + L_p$ is therefore the width of the layer within which charge separation occurs. Electrons and holes due to photons absorbed deeper in the solid recombine and do not contribute to the photocurrent. Recombination in the bulk can either be radiative or non-radiative.

The steady state current has been calculated by Gärtner [74], and later Butler [75], and Ginley [76]. Albery and coworkers have calculated minority carrier concentration profiles for a semiconductor/electrolyte interface under illumination [77]. For the case in which surface recombination is unimportant the photocurrent quantum yield is given by:

$$\frac{j}{e\phi(0)} = 1 - \frac{\exp(-\alpha W_{depl})}{1 + \alpha L_p} \quad (1.11)$$

in which $j/e\phi(0)$ is the absolute quantum yield (number of electrons measured in the external circuit divided by the number of absorbed photons (we assume that $1/\alpha$ is smaller than the thickness of the sample such that all non-reflected photons are absorbed)). The Gärtner equation (1.11) implies that a plot of $-\ln(1 - j/e\phi(0))$ vs W_{depl} should yield a straight line with slope α and abscissa at $W_{depl} = 0$ of $\ln(1 + \alpha L_p)$. The absorption coefficient and L_p can thus be determined from a measurement of the photocurrent vs voltage, since W_{depl} is directly related to electrode potential by equation 1.3. The above result is used several times in this thesis (see figures 4.4 and 6.6 on pages 74 and 102). In chapter 4 it is used to determine the absorption spectrum of SiC as a function of photon energy (Fig. 4.7, page 77).

As already stated, photons that are absorbed outside the charge separation layer do not yield photocurrent. Instead, the electron-hole pairs recombine either radiatively (to give photons) or non-radiatively (giving phonons). We can therefore easily calculate the photoluminescence intensity from equation 1.11 [74, 78–80].

$$I_{PL} = \frac{\phi(0)\kappa}{1 + \alpha L_p} \exp(-\alpha W_{depl}) \quad (1.12)$$

κ in this equation is the ratio of the rates of radiative and non-radiative recombination. Unfortunately, it is extremely difficult to measure the absolute photoluminescence quantum yield. It is more practical to relate the photoluminescence intensity to the maximum intensity, that is observed at the flat-band potential. Since W_{depl} at $V = V_{fb}$ is 0, equation 1.12 then becomes:

$$\frac{I_{PL}}{I_{PL,max}} = \left(\frac{\phi(0)\kappa}{1 + \alpha L_p} \exp(-\alpha W_{depl}) \right) / \left(\frac{\phi(0)\kappa}{1 + \alpha L_p} \right) = \exp(-\alpha W_{depl}) \quad (1.13)$$

A plot of $-\ln(I_{PL}/I_{PL,max})$ vs W_{depl} should therefore give a straight line through the origin with slope α . Figure 6.8 (page 103) shows such a plot for the *in-situ* photoluminescence of GaN. Unfortunately, by normalising the photoluminescence intensity, we lose information on L_p . It is, however, possible to determine L_p by using two different excitation wavelengths (λ_1, λ_2) for which the

semiconductor has different (known!) absorption coefficients. Assuming $\phi(0)$ to be the same for both wavelengths, we can write:

$$\begin{aligned} \frac{I_{PL,\lambda_1}}{I_{PL,\lambda_2}} &= \frac{1 + \alpha_2 L_p}{1 + \alpha_1 L_p} \exp(-(\alpha_1 - \alpha_2)W_{depl}) \\ \Rightarrow L_p &= \frac{\frac{I_{PL,\lambda_1}}{I_{PL,\lambda_2}} + \exp(-(\alpha_1 - \alpha_2)W_{depl})}{\alpha_1 \frac{I_{PL,\lambda_1}}{I_{PL,\lambda_2}} + \alpha_2 \exp(-(\alpha_1 - \alpha_2)W_{depl})} \end{aligned} \quad (1.14)$$

To use this relation effectively, accurate data on α are needed, since the difference of the absorption coefficients appears in an exponential term.

1.3 Outline of this thesis

This thesis is devoted to an electrochemical study of large band gap chemically stable semiconductors. The main focus is on the photoelectrochemical characterization and on interfacial charge transfer kinetics.

Chapter 2 describes the electrode kinetics observed with single crystal diamond electrodes prepared from homo-epitaxial layers of CVD diamond in solutions of simple (one electron) redox species. Since diamond has a very large bandgap (5.54 eV), charge transfer kinetics are expected to be severely impeded. This does not appear to be the case; current-potential curves resemble those of metal electrodes. It is proposed that charge transfer at diamond electrodes is mediated by surface states. In chapter 3 the results of electrical impedance measurements are used to develop a model for electron transfer at diamond electrodes.

Chapter 4 presents a photoelectrochemical study of SiC electrodes in aqueous solutions. Results of capacitance-voltage measurements yield the doping density with high accuracy. Measurements of the flat band potential as a function of pH provide insight into the surface chemistry of SiC. It is shown that Si-OH groups, present at the surface, can either donate protons to or capture protons from solution. This results in an interesting pH dependence of the flat band potential. Furthermore, results are shown of photocurrent-voltage and IMPS (Intensity Modulated Photocurrent Spectroscopy) measurements from which the minority carrier diffusion length is determined. Moreover, we show that it is possible to determine very accurately the absorption spectrum of SiC from an analysis of the photocurrent spectrum.

In chapter 5 we describe measurements on anodically prepared porous SiC. SEM(Scanning Electron Microscopy) micrographs show a highly porous layer having structures with dimensions of about 50 nm. The photocurrent quantum yield of a porous SiC/electrolyte diode is enhanced spectacularly with respect to that of a flat diode for light absorbed in the indirect bandgap and for sub-bandgap light.

Finally, in chapter 6 we describe results of photoelectrochemical measurements on GaN electrodes. First, the electrodes are characterized in photoluminescence and photoelectrochemical experiments. From these measurements the potential distribution at the semiconductor/electrolyte interface is obtained. These results form the basis for understanding *in-situ* photoluminescence excitation spectra of the GaN/electrolyte diode. These spectra provide clear evidence for excitonic absorption at room temperature. The properties of the semiconductor/electrolyte system are shown to be instrumental in separating excitonic absorption processes from band-band absorption.

References

- [1] S. T. Sheppard, M. R. Melloch, and J. J. A. Cooper, IEEE Elec. Dev. Lett. **43**, 1 (1996), see the device at: <http://yake.ecn.purdue.edu/~shepman/SiC.CCD.html>.
- [2] <http://www.lerc.nasa.gov/WWW/SiC/SiC.html>.
- [3] P. Ball, Nature **381**, 116 (1996).
- [4] K. Okano, S. Koizumi, S. R. P. Silva, and G. A. J. Amaratunga, Nature **381**, 140 (1996).
- [5] G. Janssen, *Homoepitaxial diamond synthesized by CVD processes* (Thesis University of Nijmegen, Nijmegen, 1984).
- [6] W. N. Wang, N. A. Fox, J. W. Steeds, S. R. Lin, and J. E. Butler, J. Appl. Phys. **80**, 6809 (1996).
- [7] R. C. DeVries, Ann. Rev. Mater. Sci. **17**, 161 (1987).
- [8] P. M. Natishan and A. Morrish, Mater. Lett. **8**, 269 (1989).
- [9] G. M. Swain, J. Electrochem. Soc. **141**, 3382 (1994).
- [10] C. Kittel, *Introduction to Solid State Physics* (John Wiley & Sons, New York, 1976).
- [11] G. M. Swain, Adv. Mater. **6**, 388 (1994).
- [12] C. Bandis and B. B. Pate, Phys. Rev. B **52**, 12056 (1995).
- [13] L. Diederich, O. Küttel, E. Schaller, and L. Schlapbach, Surf. Sci. **349**, 176 (1996).
- [14] P. E. Pehrsson, J. P. Long, M. J. Marchywka, and J. E. Butler, Appl. Phys. Lett. **67**, 3414 (1995).
- [15] Y. V. Pleskov, A. Y. Sakharova, M. D. Krotova, L. L. Bouilov, and B. V. Spitsyn, J. Electroanal. Chem. **228**, 19 (1987).

- [16] A. Y. Sakharova, L. Nyikos, and Y. V. Pleskov, *Electrochim. Acta* **37**, 973 (1992).
- [17] R. Tenne, K. Patel, K. Hashimoto, and A. Fujishima, *J. Electroanal. Chem.* **347**, 409 (1993).
- [18] J. van de Lagemaat, G. Z. Cao, G. Jansen, D. Vanmaekelbergh, and J. J. Kelly, *Electrochem. Soc. Proc.* **95-21**, 103 (1995).
- [19] A. Y. Sakharova, Y. V. Pleskov, F. D. Quarto, S. Piazza, C. Sunseri, I. G. Teremetskaya, and V. P. Varnin, *J. Electrochem. Soc.* **142**, 2704 (1995).
- [20] N. Vinokur, B. Miller, Y. Avyigal, and R. Kalish, *J. Electrochem. Soc.* **143**, L238 (1996).
- [21] H. B. Martin, A. Argoitia, U. Landau, A. B. Anderson, and J. C. Angus, *J. Electrochem. Soc.* **144**, L133 (1996).
- [22] Y. V. Pleskov, V. P. Varnin, I. G. Teremetskaya, and A. V. Churikov, *J. Electrochem. Soc.* **144**, 175 (1997).
- [23] S. Alhashem, F. Chambers, J. W. Strojek, G. M. Swain, and R. Ramesham, *Anal. Chem.* **67**, 2812 (1995).
- [24] J. Xu, M. C. Granger, Q. Chen, J. W. Strojek, T. E. Lister, and G. M. Swain, *Anal. Chem. News & Feat.* **Oct. 1**, 591A (1997).
- [25] Y. V. Pleskov, A. D. Modestov, Y. E. Evstefeeva, and V. M. Mazin, *Electrochem. Soc. Meeting Abstracts* **97-2**, 1953 (1997).
- [26] A. D. Modestov, Y. E. Evstefeeva, Y. U. Pleskov, V. M. Mazin, V. P. Varnin, and I. G. Teremetskaya, *J. Electroanal. Chem.* **431**, 211 (1997).
- [27] L. Boonma, T. Yano, D. A. Tryk, K. Hashimoto, and A. Fujishima, *J. Electrochem. Soc.* **144**, L145 (1997).
- [28] Y. V. Pleskov, V. Y. Mishuk, M. A. Abatur, V. V. Elkin, M. D. Krotova, V. P. Varnin, and I. G. Teremetskaja, *J. Electroanal. Chem.* **396**, 227 (1995).
- [29] Y. V. Pleskov, V. V. Elkin, M. A. Abatur, M. D. Krotova, V. Y. Mishuk, V. P. Varnin, and I. G. Teremetskaja, *J. Electroanal. Chem.* **413**, 105 (1996).
- [30] A. Y. Sakharova, Y. V. Pleskov, F. D. Quarto, S. Piazza, C. Sunseri, I. G. Teremetskaja, and V. P. Varnin, *Russ. J. Electrochem.* **31**, 169 (1995).
- [31] H. J. Round, *Electr. World* **19**, 309 (1907).
- [32] G. L. Harris, *Properties of Silicon Carbide* (INSPEC EMIS Datareviews No13, Exeter, 1995).
- [33] J. A. Lely, *Ber. Deutsch. Keram. Ges.* **32**, 229 (1955).
- [34] <http://www.cree.com>.
- [35] R. Allen, *New Scientist* 14 june, 34 (1997).
- [36] S. Strite and H. Morkoç, *J. Vac. Sci. Techn. B* **10**, 1237 (1992).
- [37] H. Morkoç, S. Strite, G. B. Gao, M. E. Lin, B. Sverdlov, and M. Burns, *J. Appl. Phys.* **76**, 1363 (1994).
- [38] T. Inoue, A. Fujishima, and S. Konishi, *Nature* **277**, 638 (1979).
- [39] I. Lauermann, R. Memming, and D. Meissner, *J. Electrochem. Soc.* **144**, 73 (1997).
- [40] J. O. M. Bockris and K. Uosaki, *J. Electrochem. Soc.* **124**, 1348 (1977).

- [41] T. Inoue and T. Yamase, Chem. Lett 869 (1985).
- [42] J. S. Shor and A. D. Kurtz, J. Electrochem. Soc. **141**, 778 (1994).
- [43] J. S. Shor and R. M. Osgood, J. Electrochem. Soc. **140**, L133 (1993).
- [44] J. S. Shor, X. G. Zhang, and R. M. Osgood, J. Electrochem. Soc. **139**, 1213 (1992).
- [45] L. Zhou, V. Audurier, P. Pirouz, and J. A. Powell, J. Electrochem. Soc. **144**, L161 (1997).
- [46] M. Gleria and R. Memming, J. Electroanal. Chem. **65**, 163 (1975).
- [47] A. Manivannan, A. Fujishima, and G. V. Subba Rao, Ber. Bunsenges. Phys. Chem. **92**, 1522 (1988).
- [48] H. Morisaki, H. Ono, and K. Yazawa, J. Electrochem. Soc. **131**, 2081 (1984).
- [49] J. S. Shor, I. Grimberg, B.-Z. Weiss, and A. D. Kurtz, Appl. Phys. Lett. **62**, 2836 (1993).
- [50] T. Matsumoto, J. Takahashi, T. Tamaki, T. Futiga, and H. Mimura, Appl. Phys. Lett. **64**, 226 (1994).
- [51] A. O. Konstantinov, C. I. Harris, and E. Janzén, Appl. Phys. Lett. **65**, 2699 (1994).
- [52] J. I. Pankove, E. A. Miller, and J. E. Berkeyheiser, RCA Rev. **32**, 383 (1970).
- [53] G. Fasol, Science **272**, 1751 (1996).
- [54] M. P. Mack, A. C. Abare, M. Aizcorbe, P. Kozodoy, S. Keller, U. Mishra, L. A. Col-dren, and S. P. DenBaars, Mater. Res. Soc. Internet J. **2**, Article 41 (1997), available at : <http://nsr.mij.mrs.org/2/41/>.
- [55] S. Yoshida, J. Cryst. Growth **181**, 293 (1997).
- [56] M. Ohkubo, Jpn. J. Appl. Phys. **36**, L955 (1997).
- [57] C. Youtsey, I. Adesida, and G. Bulman, Appl. Phys. Lett. **71**, 2151 (1997).
- [58] C. Youtsey, I. Adesida, and G. Bulman, Electron. Lett. **33**, 2 (1997).
- [59] S. S. Kocha, M. W. Peterson, D. J. Arent, J. M. Redwing, M. A. Tischler, and J. A. Turner, J. Electrochem. Soc. **142**, L238 (1995).
- [60] S. R. Morrison, *Electrochemistry at semiconductor and oxidized metal electrodes* (Plenum, New York, 1980).
- [61] Y. V. Pleskov, Prog. Surf. Membrane Sci. **7**, 57 (1973).
- [62] R. de Gryse, W. P. Gomes, F. Cardon, and J. Vennik, J. Electrochem. Soc. **122**, 711 (1975).
- [63] D. Vanmaekelbergh, Electrochim. Acta **42**, 1121 (1997).
- [64] D. Vanmaekelbergh, Electrochim. Acta **42**, 1135 (1997).
- [65] H. Gerischer, Z. Phys. Chem. N. F. **26**, 223 (1960).
- [66] H. Gerischer, Z. Phys. Chem. N. F. **27**, 48 (1961).
- [67] H. Gerischer, J. Phys. Chem. **95**, 1356 (1991).
- [68] M. A. Green, *Solar Cells* (The University of New South Wales, Kensington, 1992).
- [69] S. N. Frank and A. J. Bard, J. Am. Chem. Soc. **97**, 7427 (1975).
- [70] P. A. Kohl and A. J. Bard, J. Am. Chem. Soc. **99**, 7531 (1977).
- [71] P. M. Hoffmann, G. Oskam, and P. C. Searson, J. Appl. Phys. **83**, 4309 (1998).
- [72] F. Willig, K. Bitterling, K.-P. Charlé, and F. Decker, Ber. Bunsenges. Phys. Chem. **88**, 374 (1984).

-
- [73] F. Willig, *Ber. Bunsenges. Phys. Chem.* **92**, 1312 (1988).
 - [74] W. W. Gärtner, *Phys. Rev.* **116**, 84 (1959).
 - [75] M. A. Butler, *J. Appl. Phys.* **48**, 1914 (1977).
 - [76] D. S. Ginley and M. A. Butler, *J. Appl. Phys.* **48**, 2019 (1977).
 - [77] W. J. Albery, P. N. Bartlett, A. Hamnett, and M. P. Dare-Edwards, *J. Electrochem. Soc.* **128**, 1492 (1981).
 - [78] G. Chmiel and H. Gerischer, *J. Phys. Chem.* **94**, 1612 (1990).
 - [79] A. A. Burk, P. B. Johnson, W. S. Hobson, and A. B. Ellis, *J. Appl. Phys.* **59**, 1094 (1986).
 - [80] G. H. Schoenmakers, D. Vanmaekelbergh, and J. J. Kelly, *J. Phys. Chem.* **100**, 3215 (1996).

Chapter 2

Electrochemistry of homoepitaxial CVD diamond. Part I

Energetics and electrode kinetics in aqueous electrolytes

Abstract

The current-potential characteristics and the electrical impedance of two crystallographic faces of single crystalline CVD grown diamond with a high acceptor concentration were investigated. The interfacial capacitance obeys the Mott-Schottky relationship in a considerable potential range and can hence be assigned to a depletion layer in the diamond crystal. The energetic position of the valence band edge is about 4 V vs. NHE for (100) diamond and about 2.5 V vs. NHE for (110) oriented diamond. Oxygen and hydrogen evolution exhibit large overpotentials, in contrast to one-equivalent 'simple' redox reactions. The rate of the latter is determined by the reorganization energy of the redox system, and not by the band bending in the diamond crystal. Surface states are believed to play an important role in the charge transfer kinetics.

2.1 Introduction

Diamond exhibits several remarkable properties of technological interest: it is very dense and extremely hard, it has a large thermal conductivity and free carriers with a high mobility. In its undoped form, diamond is an insulator with a bandgap of 5.5 eV; *p*-type conductivity and semi-metallic behavior can be achieved by boron incorporation [1]. These properties and the chemical inertness make CVD grown diamond a promising material for (opto)electronic devices operating at high temperature and pressure and under extreme chemical conditions. Furthermore, the observation of negative electron affinity (NEA) at specially pretreated surfaces [2–6], makes it an excellent choice as electron emitter in flat-panel displays.

There is a growing interest in the electrochemical properties of diamond [4, 7–25] which may prove important in industrial applications, for instance for electroanalytical or electrosynthetic purposes [10–12, 15, 16, 18, 19]. Diamond is also an interesting electrode material for more fundamental research, including the study of electron transfer processes. In contrast to many semiconductors and metals, it does not form an interfacial (oxide) layer when brought into contact with an aqueous solution. Moreover, it does not dissolve anodically or cathodically.

Most of the results reported so far deal with polycrystalline diamond electrodes of widely varying quality and with moderate or high acceptor concentration. Electrochemical impedance measurements were used to determine the capacitance of the diamond/aqueous electrolyte interface. Generally, the values reported for the interfacial capacitance were large; electrodes from good quality material with a faceted surface have a smaller interfacial capacitance than those from less well-defined material with a “cauliflower” surface morphology and surface regions consisting of *sp*² carbon [11]. In some cases, the results indicated that the interfacial capacitance is determined by a majority carrier depletion layer [7, 11, 13, 18, 22–25]; the capacitance-voltage plot agrees with the Mott-Schottky relationship in a limited potential range (between 0.2 and 0.7 V vs NHE). The flat-band potential was generally found at +0.7 vs. NHE. This would place the bottom of the conduction band at very high energy (+4.6 eV vs. NHE). Since this is above the vacuum level, these surfaces should exhibit NEA. However, NEA is only observed at specially pretreated surfaces [6], or nitrogen-doped diamond [3].

The current-potential characteristics in aqueous electrolytes also depend strongly on the quality of the diamond [7, 16]. With good quality polycrystalline electrodes, water oxidation and hydrogen evolution occur at considerable overpotential (about 1 volt) [16]; the current is negligible in a large potential window (about 3 V). With material of lower quality (higher sp^2 -carbon content), a much smaller potential window is observed [7, 16]. Rather surprisingly, with simple redox systems such as $\text{Fe}(\text{CN})_6^{3-/4-}$, $\text{Fe}^{3+/2+}$, and $\text{Ru}(\text{NH}_3)_6^{3+/2+}$ good quality electrodes exhibit reversible electrochemical reduction and oxidation kinetics around the equilibrium potential of the redox system [8, 11, 12, 15, 18–21]. This has been attributed to “semimetallic” properties, or to direct exchange between the redox system and the valence band [20, 21]. The latter is, however, unlikely. If the reported value of 0.7 V (vs. NHE) is taken for the flat-band potential, then the valence band edge at the surface is at +1V. This means that, at equilibrium, electron exchange with $\text{Fe}(\text{CN})_6^{3-/4-}$ ($V_{eq}=0.4$ volt), occurs at 0.6 eV below $E_{F,redox}$. Hence, electron exchange is expected to be very slow, in contrast to the relatively high exchange rates at equilibrium and the nearly reversible electrode kinetics that are observed. Furthermore, exchange via the valence band implies diode-like current-potential characteristics, since the rate of oxidation of the reduced form of the redox system depends on the applied potential, but the reduction reaction does not (assuming that a change in potential only influences the potential drop over the depletion layer inside the semiconductor). Pleskov and Modestov also noted that the observed ‘metallic-like behaviour’ is in conflict with their assumption of exchange via the valence band. They suggested that surface states caused by point-defects could mediate the reaction [20, 21]. Alhashem *et al.* in an early paper on redox electrochemistry at polycrystalline diamond [18] ascribed their results to the presence of non-diamond carbon impurities at the surface.

There are two intriguing aspects to the electrochemistry of polycrystalline diamond in aqueous solutions: (i) the relatively negative value of the flat band potential places the conduction band edge of the semiconductor above vacuum level; (ii) there is a discrepancy between the diode characteristics observed in impedance measurements and the “metallic” properties of diamond found in redox electrochemistry. This led us to reinvestigate the mechanism of electron exchange reactions at diamond surfaces. To avoid possible problems with multifaceted surfaces, grain boundaries and non-diamond carbon impurities we used high quality homoepitaxial layers grown on (100) and (110) oriented single crystal natural diamond [1, 26]. This approach allowed us to investigate the

influence of crystallographic orientation on the electrode properties. The interfacial capacitance was studied over a wide potential range. In addition, the electrochemical kinetics of electron transfer were investigated with $\text{Fe}(\text{CN})_6^{3-/4-}$, $\text{Fe}^{3+/2+}$, and $\text{Ce}^{4+/3+}$ as redox systems. In chapter 3 of this thesis (page 45), a more detailed analysis of the electrochemical kinetics on the basis of electrical impedance measurements is presented.

2.2 Experimental

The samples used in this study were homoepitaxial layers (5 μm thick) grown on (100) or (110) oriented natural diamond (type IIa or IIb, 5x5 mm \square) in a conventional hot-filament CVD reactor [1, 26–30]. The growth conditions used were as follows: nominal filament temperature: 2500 °C; nominal substrate temperature: 700 - 900 °C; distance between the filament and the substrates: 10 mm; total gas flow of a mixture of 2 % methane in hydrogen : 300 sccm; and the total pressure in the reactor: 50 mbar. The filament was made of tantalum carbide. The dopant source was boron oxide (B_2O_3) placed in a Mo crucible on the substrate holder beside the diamond substrates. The boron concentration in the gas phase could be controlled by varying the substrate holder temperature. The dopant density was $10^{19} - 10^{20} \text{ cm}^{-3}$, as measured by infrared absorption and Hall effect measurements [1, 30]. Prior to the diamond growth the substrates were first cleaned in a boiling mixture of NaNO_3 and H_2SO_4 , then in a boiling mixture of HCl and HNO_3 , rinsed with deionized water and finally with isopropanol. The layers obtained in this way are smooth homoepitaxial films with few dislocations. Fig. 2.1 shows a SEM image of a representative CVD diamond layer. Further evidence for the monocrystalline nature of the diamond layers was obtained from X-ray diffraction and the symmetry of the growth patterns on the surfaces [27].

Prior to the contacting procedure the samples were boiled in $\text{H}_2\text{SO}_4 + \text{NaNO}_3$ solution and heated in HCl/HNO_3 3:1, to remove metal and sp^2 -carbon impurities. This pretreatment will give an “oxidized” surface. Ohmic contacts were prepared by microwave sputtering of Ti/Pt/Au (20/10/300 nm) on the edges of the samples, followed by a rapid thermal anneal at 500 °C. The samples were glued on copper rods. A thin copper wire and silver paste was used to connect the Ohmic contacts on top of the diamond samples to the copper rod. This assembly was mounted in PVC holders that could be used as rotating disk electrodes. The contacts and the copper were protected from the electrolyte solution by Apiezon

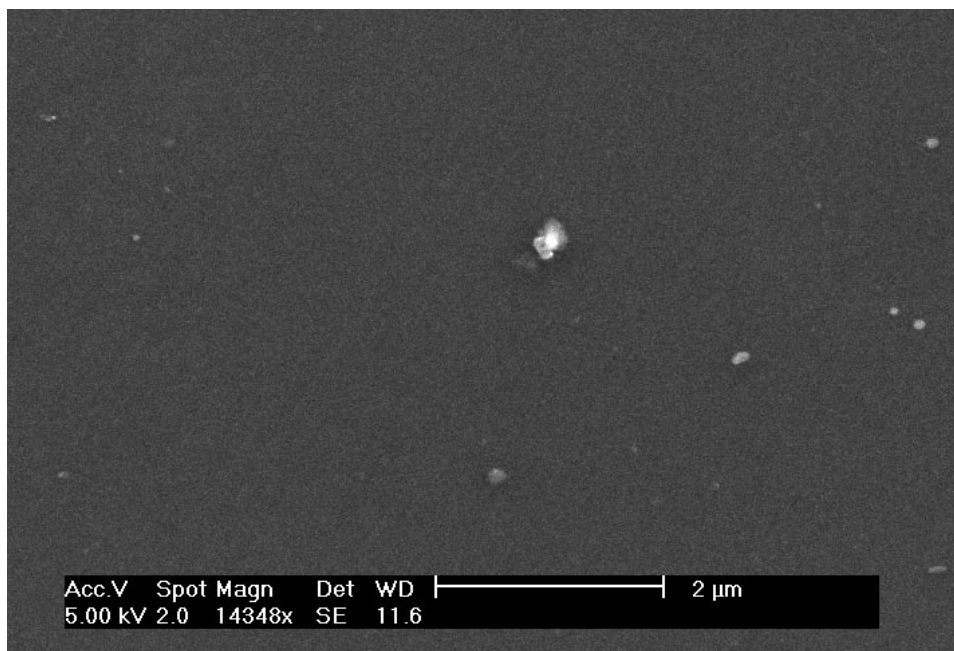


FIGURE 2.1. SEM image of a homoepitaxial CVD diamond layer grown on a type Ib substrate. The orientation of the layer is (100), its thickness $5\text{ }\mu\text{m}$. The doping density was 10^{19} cm^{-3} . The white feature is a dust particle that was used to focus the electron microscope. It is clear from this micrograph that no grain boundaries are present in the layer.

resin, leaving about 5 mm^2 diamond exposed. This assembly was mounted as a working electrode in a conventional three electrode electrochemical cell with Ag/AgCl or SCE (Saturated Calomel Electrode) as a reference electrode, which was connected in parallel to a platinum wire through a 20pF capacitance to minimise high frequency phase shift errors [31]. A large area platinum sheet served as a counter electrode. All potentials are given with respect to the normal hydrogen electrode (NHE). The cell was controlled by means of an EG&G PAR273A or a PAR283 potentiostat. The electrical impedance measurements were performed using a Solartron SI1255 FRA in conjunction with the previous set-up.

The solutions were prepared from analytical grade reagents and doubly distilled water. Prior to the measurements the solutions were deaerated by nitrogen or argon bubbling. The samples were cleaned before each measurement by dipping in 37 % HCl.

2.3 Results and Discussion

2.3.1 The interfacial capacitance

In Fig. 2.2, the parallel equivalent capacitance C_p measured with a (100) oriented sample in aqueous 1M KOH solution is plotted as C_p^{-2} vs. the electrode potential V . The results are shown for three different measuring frequencies (214, 2140 and 21400 Hz). In fig. 2.3, similar results are presented for a (110) oriented electrode in 0.5 M H_2SO_4 solution. Plots of the steady-state current density j vs. V measured under the same conditions are presented in Fig. 2.4.

The (C_p^{-2}, V) plots are linear between +1 V and -0.4 V, the potential range in which no current flows (see Fig. 2.4). C_p is about 10^{-7} F cm^{-2} , which is typical for the depletion layer of a highly doped semiconductor. From the slope of the plot measured with a voltage modulation of 214 Hz, a concentration of free carriers (holes in the valence band) of $5 \times 10^{19} cm^{-3}$ is found for the (100) electrode, in agreement with the results obtained from IR absorption and Hall effect measurements [30]. The slopes of the (C_p^{-2}, V) plots are frequency dependent, but in-

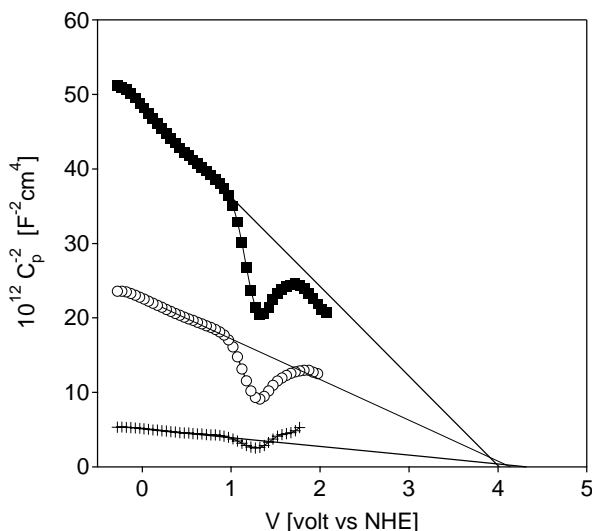


FIGURE 2.2. Plot of C_p^{-2} vs. V for a (100)-oriented diamond electrode in 1 M KOH solution (pH=14). Three measuring frequencies are shown; 21.4 kHz (■), 2.14 kHz (○), and 214 Hz (+)

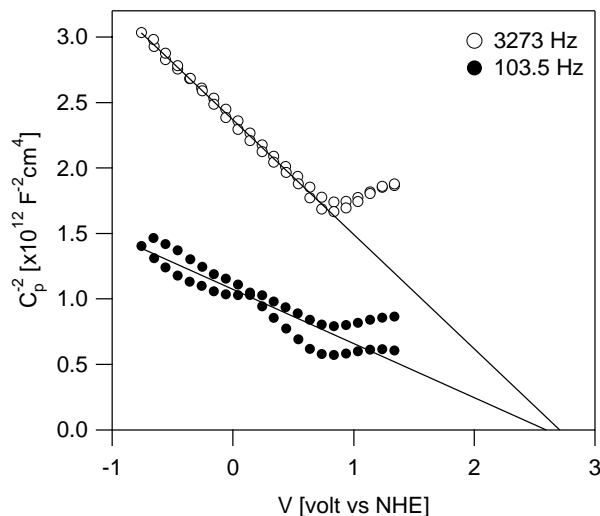


FIGURE 2.3. Plot of C_p^{-2} vs. V for a (110)-oriented diamond electrode in 0.5 M H_2SO_4 solution. Two measuring frequencies are shown; 3273 (\circ), and 103.5 Hz (\bullet)

intersect the potential axis at about + 4 V vs. NHE for the (100)-oriented electrode and +2.5 V vs. NHE for the (110)- oriented electrode. These values were independent of solution pH. It is clear that extrapolation over a large potential range gives values that are not very exact. It is, however, important to note that the potential range of interest for the charge transfer experiments described below and in chapter 3 of this thesis corresponds to strong depletion (the Mott-Schottky relationship holds and the flat band potential is found at very positive values).

Deviations from linearity in the (C_p^{-2}, V) are observed at potentials more positive than + 1 V and more negative than - 0.4 V. No hysteresis is observed as long as the electrode potential is kept positive of -0.4 V. The results of impedance measurements become irreproducible if hydrogen is evolved at the electrode. This is probably caused by a change in the surface chemistry from oxygen to hydrogen termination [6, 16]. The surface can be “repaired” by a short treatment with hot nitric acid.

Although the slope of the (C_p^{-2}, V) plots depended on the measuring frequency, linear fits converge to a point on the potential axis. A frequency dependent capacitance is often found for semiconductor/electrolyte interfaces. In fact, it is more the rule than the exception. Various explanations have been given to

account for such results [32]. Frequency dispersion can be due to a combination of surface roughness, with dimensions typical of the width of the depletion layer, and the resistance of the electrochemical cell [33]. Since the impedance measurements were performed with high concentrations of salt in the solution and since the specific resistance of our diamond electrodes is not large, we believe that surface roughness plays only a minor role in these results. Frequency dispersion in the (C_p^{-2}, V) plots has also been ascribed to dielectric relaxation phenomena in the depletion layer of the semiconductor giving rise to a frequency dependent dielectric constant [32]. Since the diamond crystals have a high acceptor concentration and a large density of localized impurity states, dielectric relaxation phenomena could contribute to the frequency dispersion. Pleskov and coworkers also suggested this hypothesis to account for the frequency dependent impedance of polycrystalline diamond electrodes [24]. Another possible reason for the observed frequency dispersion is that contacts to the epitaxial layers were located at the edge of the electrode surface. As a result, the series resistance associated with current flow through the thin diamond layer is not uniform over the exposed surface (the maximum resistance was about 50 Ω). It can be shown that this effect yields a considerable frequency dependence of the measured capacitance. It should be mentioned that both effects are not expected to shift the flat-band potential.

The (C_p^{-2}, V) plots converge to a common point $[V(C_p^{-2}=0)]$ on the potential axis. For semiconductors with low or moderate acceptor concentration ($N_A < 10^{18} \text{ cm}^{-3}$) this potential corresponds to the flat-band value V_{fb} . However, with highly doped semiconductors, the uncompensated negative charge in the space charge influences the distribution of the interfacial potential drop over the depletion and Helmholtz layers. This leads to deviations from the Mott-Schottky theory. It has been shown that, if the Helmholtz capacitance C_H does not depend on the potential drop over the double layer, a plot of the interfacial capacitance as C_p^{-2} versus V is still linear [32, 34]. However, the extrapolation point on the potential axis is shifted by an amount $(e\epsilon\epsilon_0 N_A)/2C_H^2$. It then follows with N_A being about 10^{20} cm^{-3} and assuming a value of $10^{-5} \text{ F cm}^{-2}$ for C_H , and a value of 5.5 for ϵ , that the extrapolation point of the (C_p^{-2}, V) plots might be up to 0.1 V more positive than the true flat-band potential. Because there is a considerable uncertainty in the value of C_H , it must be concluded that with highly doped semiconductors there is uncertainty in the determination of the flat-band potential from Mott-Schottky plots. Nevertheless, it should be noted that the value of $V(C_p^{-2}=0)$ found here is 3 volts more positive than the values reported for polycrystalline

diamond in the literature. This indicates that in our case the energies of the conduction and valence band edges are lower than those reported by other groups. The chemical nature of the diamond surface should influence the position of the bandedges. In hydrogen plasma pretreated and reconstructed diamond, the energetic position of the bandedges is very high, so that hydrogen terminated diamond may even exhibit a NEA [4, 5, 35]. In our case, the diamond surface was subjected to a strongly oxidizing pretreatment which leads to partial C-OH and C=O termination of the surface [6, 9]. This is expected to shift the band-edges to lower energies (i.e. to more positive potentials), because of the dipole character of these groups. A completely H-terminated (100) oriented diamond has $3.16 \times 10^{15} \text{ cm}^{-2}$ surface C-H bonds. Using the tabulated values for the dipole moment of t-butyl alcohol ($\mu_D \approx 1.6 \times 3.36 \cdot 10^{-30} \text{ C m}^{-1}$), one calculates from $\Delta V = \frac{\mu_D c}{\epsilon \epsilon_0}$ (c is the number of groups per cm^2), that a shift of 3 volts corresponds to about 16% coverage of the surface with hydroxyl-units. This may explain why the values for the flat-band potential presented in this chapter are more positive than those found for H-terminated polycrystalline diamond. Furthermore, the same percentage for (110)-oriented diamond leads to a somewhat smaller shift (about 2.1 volts) because of the lower density of C-H bonds ($2.23 \times 10^{15} \text{ cm}^{-2}$). This would correlate with the flat-band potential of (110) electrodes which is less positive than that of (100)-oriented electrodes.

2.3.2 Current-potential characteristics in indifferent electrolyte solution

In Fig. 2.4, the current density j is plotted vs. the electrode potential V , for a (100) oriented sample in aqueous electrolytes of pH = 0, 6.3, and 14. In 1 M KOH solution, oxygen evolution sets in at a potential of + 1.5 V. A small current plateau before this onset was also observed with polycrystalline diamond [16]. XPS measurements indicate that this is probably linked to oxidation of the surface [16]. The overpotential for oxygen evolution is more than 1 V since the Nernst potential of the $\text{O}_2/\text{H}_2\text{O}$ system is 0.39 V in an aqueous solution of pH = 14. In 0.5 M H_2SO_4 solution, an overpotential of about 0.5 V is found. The overpotential for hydrogen evolution is -1 V at all pH values studied here. Similar results have been reported for the oxygen and hydrogen evolution with polycrystalline diamond. Miller and co-workers also observed large overpotentials for the oxidation of halides [15]. As for hydrogen and oxygen evolution, these processes involve adsorbed intermediates and ionic and molecular transfer across

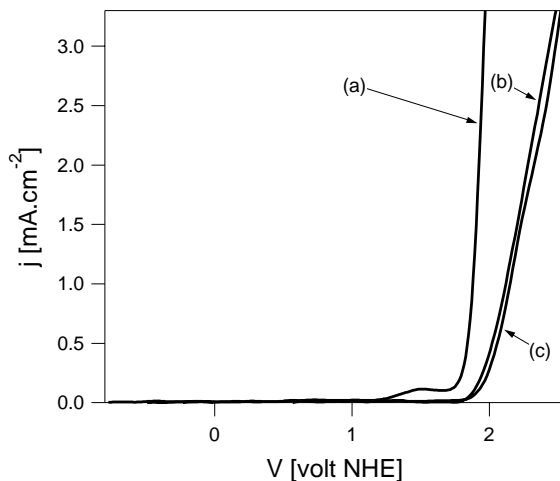


FIGURE 2.4. j - V curves of (100)-oriented diamond in three different solutions. (a) 1M KOH, (b) 0.5 M K_2SO_4 , (c) 0.5 M H_2SO_4 .

the Helmholtz-layer [36, 37]. The large overpotentials for multi-equivalent electrochemical reactions which require chemical reorganization are typical for diamond electrodes and are in marked contrast to the nearly reversible electrode kinetics observed for outer sphere electron transfer with simple redox systems [15] (see following section).

2.3.3 Electrochemical processes with simple redox systems

In Figs. 2.5, 2.6 and 2.7, the current density j is plotted vs. the electrode potential V for a (100) oriented electrode in aqueous solutions containing $Fe(CN)_6^{3-/4-}$ (pH=14), $Fe^{3+/2+}$ (pH=1), and $Ce^{4+/3+}$ (pH=1); the equilibrium potentials (V_{eq}) of these systems are 0.4, 0.77 and 1.3 V vs. NHE, respectively. In the inserts, the logarithm of the current density is plotted vs. the overpotential $V - V_{eq}$. It can be seen that the current goes to zero at V_{eq} , and that cathodic reduction and anodic oxidation of the redox system are observed at negative and positive overpotentials, respectively. In all cases, except for the oxidation of Ce^{3+} which occurs together with oxygen evolution, the current becomes diffusion limited above a given overpotential. The $Fe(CN)_6^{3-/4-}$ system shows the most reversible and $Ce^{4+/3+}$ the least reversible electrode kinetics. Furthermore, the plots show some hysteresis.

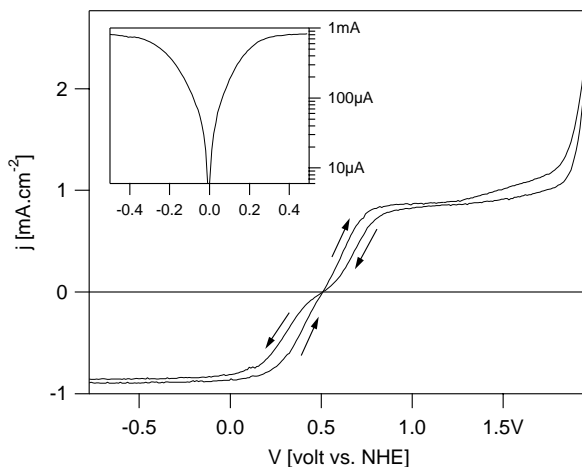


FIGURE 2.5. j - V curve of (100)-oriented diamond in a solution containing 0.01M Fe(CN)_6^{3-} / 0.01M Fe(CN)_6^{4-} in 1M KOH. The arrows indicate the direction of the scan. The scanrate was 50 mV.s^{-1} . The inset shows the current on a log axis vs. overpotential.

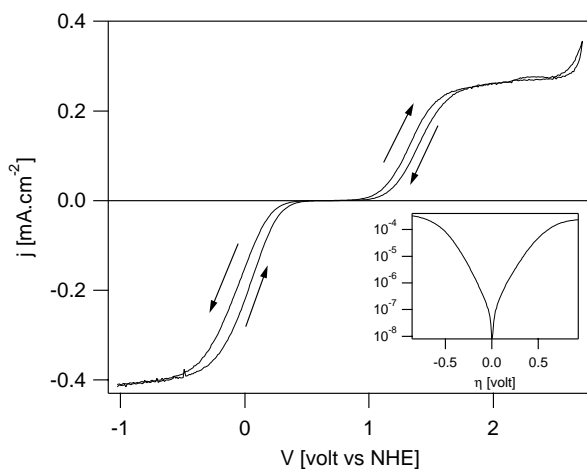


FIGURE 2.6. j - V curve of (100)-oriented diamond in a solution containing 0.01M Fe^{3+} / 0.01M Fe^{2+} in 0.5M H_2SO_4 . The inset shows the current on a log axis vs. overpotential.

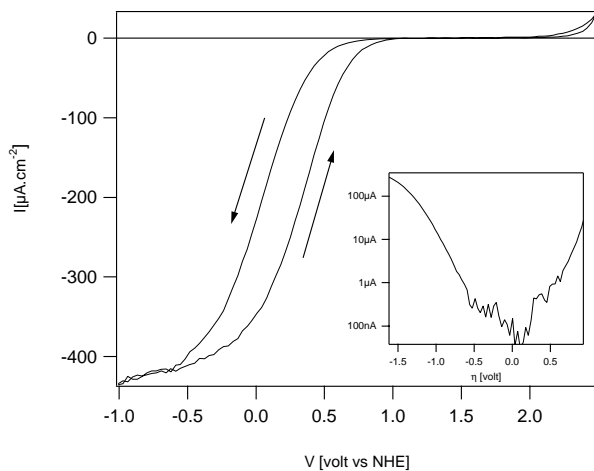


FIGURE 2.7. j - V curve of (100)-oriented diamond in a solution containing 0.01M Ce^{4+} /0.01M Ce^{3+} in 0.5M H_2SO_4 . The inset shows the current on a log axis vs. overpotential.

Comparable results are found with (110) oriented diamond. In this case, however, a larger overpotential is needed to obtain diffusion limitation, and a slightly lower exchange current density is found. Similar results were found with polycrystalline electrodes [8, 11, 12, 15, 18–21].

These results are striking, considering that we are dealing with a semiconductor with a huge bandgap and that in the vicinity of the equilibrium potential of the redox systems, the diamond surface is strongly depleted of majority carriers. Nevertheless, diode properties are not observed; both cathodic and anodic reactions occur at a significant rate, as for a reversible reaction at a metal electrode. With the diamond electrodes used here, direct exchange via the valence band cannot occur since the difference between the equilibrium potentials of the redox systems and the valence band edge is much too large (several volts). To account for charge transfer, one must invoke mediation by surface states.

Electron transfer has been investigated using impedance spectroscopy (chapter 3 of this thesis (page 45)). The results are consistent with a mechanism in which electron exchange between these redox systems and diamond occurs in two steps, and is mediated by bandgap states at the surface. Exchange between the valence band and the surface states occurs by a tunneling pro-

TABLE 2.1. Rate constant at equilibrium for electron transfer at diamond and platinum electrodes.

$k^\ominus [\text{cm s}^{-1}]$	Pt	diamond (100)	diamond (110)
$\text{Fe}(\text{CN})_6^{3-/4-}$	10^{-1}	10^{-5}	10^{-6}
$\text{Fe}^{3+/2+}$	5×10^{-3}	10^{-7}	10^{-7}
$\text{Ce}^{4+/3+}$	4×10^{-4}	10^{-8}	

cess through the depletion layer, probably mediated by localized bulk states (e.g. states in the dopant “band”). Electron exchange between the solid and the redox system occurs by isoenergetic tunneling across the Helmholtz-layer. That electron exchange involves at least two steps can also be inferred from the current-potential plots with the three redox systems. As the Nernst-potential of $\text{Fe}(\text{CN})_6^{3-/4-}$ is about 1 volt more negative than that of $\text{Ce}^{4+/3+}$, the surface region of the electrode is more strongly depleted at V_{eq} of $\text{Fe}(\text{CN})_6^{3-/4-}$ than at V_{eq} of $\text{Ce}^{4+/3+}$. Hence, electron tunneling across the depletion layer should be slower with $\text{Fe}(\text{CN})_6^{3-/4-}$. In fact, $\text{Fe}(\text{CN})_6^{3-/4-}$ is the most reversible redox system, as at metal electrodes. This indicates that the rate is determined by electron exchange across the Helmholtz-layer; this depends on the reorganization energy of the redox system. Independent results show that this reorganization energy is smaller for $\text{Fe}(\text{CN})_6^{3-/4-}$ than for $\text{Ce}^{4+/3+}$ so that electron exchange at the equilibrium potential and small overpotentials is faster with $\text{Fe}(\text{CN})_6^{3-/4-}$. Electron exchange between the bulk and surface states probably occurs by a (inelastic) multi-step tunneling process, mediated by localised states in the depletion layer [38]. Table 2.1 compares the rate constant for electron transfer at the equilibrium potential (as determined from the $j - V$ curves) with the values observed at platinum electrodes [39]. The rate constant is consistently lower for diamond ($10^4 \times$) than for platinum. This rate is influenced by, among other factors, the density of states at the Fermi level. Obviously, this density is much higher for the metal than for diamond. The $\text{Fe}(\text{CN})_6^{3-/4-}$ couple has also been studied at polycrystalline diamond electrodes [18, 20, 21]. The rate constants found were slightly larger than we observed at single crystal surfaces. Comparison of the values reported for polycrystalline diamond [20, 21] shows the same trend as in table 2.1.

2.4 Conclusions

C_p^{-2} vs. V plots of homoepitaxial layers of CVD diamond obey the Mott-Schottky relationship in a rather wide potential range. The flat-band potential was found at 4 V vs. NHE for (100) oriented diamond, and at 2.5 V vs. NHE for (110) oriented diamond. The difference between these values and those reported for polycrystalline material may be due to the presence of surface hydroxyl or carbonyl groups. The difference between the two faces shows that we are really dealing with single crystalline layers. The doping density obtained from the plots is comparable to that found using IR absorption and Hall-measurements.

As at polycrystalline electrodes, the redox electrochemistry is similar to that observed at metals. In the present case, because of the location of the valence band edge, direct electron exchange between the valence band and the redox system is precluded. Mediation by surface states is the only possible explanation.

Because of the reversible electrode kinetics, and the large potential window (in contrast to metal electrodes) diamond may be very suitable for electroanalytical and electrosynthetic applications. The chemical nature of the surface is very important for the kinetics of charge transfer.

References

- [1] G. Janssen, W. J. P. van Enckevort, W. Vollenberg, and L. J. Giling, *Diam. and Rel. Mat.* **1**, 789 (1992).
- [2] P. Ball, *Nature* **381**, 116 (1996).
- [3] K. Okano, S. Koizumi, S. R. P. Silva, and G. A. J. Amaratunga, *Nature* **381**, 140 (1996).
- [4] C. Bandis and B. B. Pate, *Phys. Rev. B* **52**, 12056 (1995).
- [5] L. Diederich, O. Küttel, E. Schaller, and L. Schlapbach, *Surf. Sci.* **349**, 176 (1996).
- [6] P. E. Pehrsson, J. P. Long, M. J. Marchywka, and J. E. Butler, *Appl. Phys. Lett.* **67**, 3414 (1995).
- [7] Y. V. Pleskov, A. Y. Sakharova, M. D. Krotova, L. L. Bouilov, and B. V. Spitsyn, *J. Electroanal. Chem.* **228**, 19 (1987).
- [8] A. Y. Sakharova, L. Nyikos, and Y. V. Pleskov, *Electrochim. Acta* **37**, 973 (1992).
- [9] L. M. Struck and M. P. D'Evelyn, *J. Vac. Sci. Technol. A* **11**, 1992 (1993).
- [10] R. Tenne, K. Patel, K. Hashimoto, and A. Fujishima, *J. Electroanal. Chem.* **347**, 409 (1993).
- [11] G. M. Swain, *Adv. Mater.* **6**, 388 (1994).
- [12] G. M. Swain, *J. Electrochem. Soc.* **141**, 3382 (1994).

- [13] A. Y. Sakharova, Y. V. Pleskov, F. D. Quarto, S. Piazza, C. Sunseri, I. G. Teremetskaya, and V. P. Varnin, *J. Electrochem. Soc.* **142**, 2704 (1995).
- [14] J. van de Lagemaat, G. Z. Cao, G. Jansen, D. Vanmaekelbergh, and J. J. Kelly, *Electrochem. Soc. Proc.* **95-21**, 103 (1995).
- [15] N. Vinokur, B. Miller, Y. Avyigal, and R. Kalish, *J. Electrochem. Soc.* **143**, L238 (1996).
- [16] H. B. Martin, A. Argoitia, U. Landau, A. B. Anderson, and J. C. Angus, *J. Electrochem. Soc.* **144**, L133 (1996).
- [17] Y. V. Pleskov, V. P. Varnin, I. G. Teremetskaya, and A. V. Churikov, *J. Electrochem. Soc.* **144**, 175 (1997).
- [18] S. Alhashem, F. Chambers, J. W. Strojek, G. M. Swain, and R. Ramesham, *Anal. Chem.* **67**, 2812 (1995).
- [19] J. Xu, M. C. Granger, Q. Chen, J. W. Strojek, T. E. Lister, and G. M. Swain, *Anal. Chem. News & Feat.* **Oct. 1**, 591A (1997).
- [20] Y. V. Pleskov, A. D. Modestov, Y. E. Evstefeeva, and V. M. Mazin, *Electrochem. Soc. Meeting Abstracts* **97-2**, 1953 (1997).
- [21] A. D. Modestov, Y. E. Evstefeeva, Y. U. Pleskov, V. M. Mazin, V. P. Varnin, and I. G. Teremetskaya, *J. Electroanal. Chem.* **431**, 211 (1997).
- [22] L. Boonma, T. Yano, D. A. Tryk, K. Hashimoto, and A. Fujishima, *J. Electrochem. Soc.* **144**, L145 (1997).
- [23] Y. V. Pleskov, V. Y. Mishuk, M. A. Abaturov, V. V. Elkin, M. D. Krotova, V. P. Varnin, and I. G. Teremetskaja, *J. Electroanal. Chem.* **396**, 227 (1995).
- [24] Y. V. Pleskov, V. V. Elkin, M. A. Abaturov, M. D. Krotova, V. Y. Mishuk, V. P. Varnin, and I. G. Teremetskaja, *J. Electroanal. Chem.* **413**, 105 (1996).
- [25] A. Y. Sakharova, Y. V. Pleskov, F. D. Quarto, S. Piazza, C. Sunseri, I. G. Teremetskaja, and V. P. Varnin, *Russ. J. Electrochem.* **31**, 169 (1995).
- [26] W. J. P. van Enckevort, G. Janssen, W. Vollenberg, M. Chermin, L. J. Giling, and M. Seal, *Surf. Coat. Techn.* **47**, 39 (1991).
- [27] G. Janssen, W. J. P. van Enckevort, W. Vollenberg, and L. J. Giling, *J. Crystal Growth* **148**, 355 (1995).
- [28] W. J. P. van Enckevort, G. Janssen, J. J. Schermer, and L. J. Giling, *Diam. and Rel. Mater.* **4**, 250 (1995).
- [29] W. J. P. van Enckevort, G. Janssen, W. Vollenberg, and L. J. Giling, *J. Crystal Growth* **148**, 365 (1995).
- [30] E. P. Visser, G. J. Bauhuis, G. Janssen, W. Vollenberg, W. J. P. van Enckevort, and L. J. Giling, *J. Phys.: Condens. Matt.* **4**, 7365 (1992).
- [31] F. Mansfeld, S. Lin, C. Chen, and H. Shih, *J. Electrochem. Soc.* **135**, 906 (1988).
- [32] W. P. Gomes and F. Cardon, *Progress in Surface Science* **12**, 155 (1982).
- [33] G. Oskam, D. Vanmaekelbergh, and J. J. Kelly, *J. Electroanal. Chem.* **315**, 65 (1991).
- [34] R. de Gryse, W. P. Gomes, F. Cardon, and J. Vennik, *J. Electrochem. Soc.* **122**, 711 (1975).

-
- [35] Z. Zhang, M. Wensell, and J. Bernholc, Phys. Rev. B **51**, 5291 (1995).
 - [36] W. Schmickler, Chem. Phys. Lett. **237**, 152 (1995).
 - [37] M. T. M. Koper and W. Schmickler, Chem. Phys. **211**, 123 (1996).
 - [38] W. Schmickler, Ber. Bunsenges. Phys. Chem. **82**, 477 (1978).
 - [39] R. Tamamushi, *Kinetic Parameters of Electrode Reactions of Metallic Compounds* (IUPAC additional Publication Butterworths, London, 1975).

Chapter 3

Electrochemistry of homoepitaxial CVD diamond. Part II

Mechanism of electron exchange with simple redox systems

Abstract

The mechanism of electron exchange between (100) and (110) oriented homoepitaxial layers of CVD-grown diamond and simple one-equivalent redox systems was investigated using electrochemical impedance spectroscopy. The results are consistent with a model in which electron exchange occurs in two steps, mediated by interfacial band gap states. Electron exchange between the bulk diamond and the interfacial bandgap states occurs by a multistep tunneling process, while exchange between the interfacial states and the redox system occurs by isoenergetic tunneling across the Helmholtz-layer.

3.1 Introduction

In chapter 2 of this thesis (page 29), we described the current-potential characteristics of highly doped single crystalline CVD diamond electrodes in aqueous electrolytes. It was observed that the overpotentials for both the oxidation of water to form oxygen and the reduction to form hydrogen were large (≈ 1 V), leading to a large potential range in which the current is negligibly low. This is in agreement with reports of other groups who used good quality polycrystalline diamond [1–9].

Remarkably, when a simple outer sphere redox system such as $\text{Fe}(\text{CN})_6^{3-/4-}$, $\text{Fe}^{3+/2+}$, or $\text{Ce}^{4+/3+}$ is added to the electrolyte solution, large anodic and cathodic currents were observed in the potential range around the Nernst-potential, the current becoming mass-transport limited at sufficiently large anodic or cathodic overpotential. This is in agreement with previous reports of nearly reversible electrode kinetics with polycrystalline diamond and outer sphere redox systems [6–8, 10–13]. These results are unusual for a number of reasons. First, the diamond used in these experiments is a *p*-type semiconductor with a huge bandgap (5.54 eV). Direct exchange of majority carriers (holes in the valence band) with the redox system would be expected to require a considerable activation energy to bridge the depletion layer energy barrier. As a result of the large activation energy the exchange current densities at equilibrium should be extremely small. This is in contrast to the observation of nearly reversible electrode kinetics with outer sphere redox systems. Secondly, the current-potential characteristics do not agree with the diode properties expected for extrinsic, wide bandgap semiconductor electrodes. Instead, the current-potential curves are similar to those observed at metal electrodes [6–8, 10–14]. The results strongly suggest that interfacial bandgap states are mediating the electron exchange between *p*-type diamond and simple redox systems.

For semiconductors with simple redox systems, it has been shown that surface state mediated electron exchange may dominate over direct exchange with the majority carrier band if the “Fermi-level” of the redox system is sufficiently far below the bottom of the conduction band (*n*-type semiconductor) or above the top of the valence band (*p*-type) [15]. The current-potential characteristics change from diode-type to metal-type with increasing density of mediating surface states. Such changes in electrode kinetics have been demonstrated by Os- kam *et al* [16] for *p*-type GaAs provided with gold islands on the semiconductor

surface. Frank *et al.* showed that surface states play an important role in the charge transfer kinetics at TiO_2 electrodes [17].

The interfacial admittance for a semiconductor/redox system has been calculated for the case of direct and surface state mediated exchange [18]. It was shown that one can clearly distinguish between direct and surface state mediated electron exchange and that kinetic parameters may be extracted from analysis of the electrochemical admittance. In this chapter, the electrochemical admittance of electrodes of *p*-type homoepitaxial layers of CVD diamond ((100) and (110) faces) in aqueous solutions of $\text{Fe}(\text{CN})_6^{3-/4-}$, and $\text{Fe}^{3+/2+}$, are presented and analyzed on the basis of a model, similar to that previously presented [15, 18]. It follows from this analysis that surface state mediated electron exchange accounts for the interfacial admittance, and is responsible for the nearly reversible electrode kinetics with (100) and (110) faces of diamond and simple redox systems.

3.2 Results

In Fig. 3.1, the current potential characteristics of a (110) *p*-type diamond electrode in a solution containing $\text{Fe}(\text{CN})_6^{3-/4-}$ is plotted on a logarithmic scale vs. overpotential ($\eta = V - V_{eq}$). Both cathodic and anodic currents increase steeply with increasing overpotential. Mass transport limitation is reached at overpotentials larger than 0.4 volt. It is clear that the current density does not increase exponentially with the overpotential. In Figs 3.2a-f complex plane plots of the interfacial impedance measured at several overpotentials with the (110) electrode in $\text{Fe}(\text{CN})_6^{3-/4-}$ solution are presented, with the measuring frequency $\omega (= 2\pi f)$ as a parameter (the solid circles are fits to an equivalent circuit that will be introduced in the discussion section (Fig.3.6b)).

The current potential-characteristics for the (110) oriented electrode in a solution containing $\text{Fe}^{3+/2+}$, are shown in Fig. 3.3. The overpotential needed to obtain diffusion limitation of the current is larger than in the case of $\text{Fe}(\text{CN})_6^{3-/4-}$. Fig 3.4.a-f shows the corresponding complex plane impedance plots for the (110)-oriented electrode.

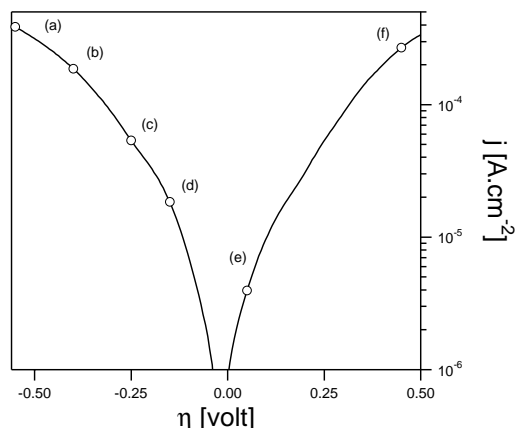


FIGURE 3.1. Current-potential characteristics of a (110) oriented electrode in a solution containing $0.01 \text{ M Fe(CN)}_6^{3-} / 0.01 \text{ M Fe(CN)}_6^{4-}$, plotted vs. overpotential ($\eta = V - V_{eq}$) on a logarithmic scale. The potentials at which the measurements shown in Fig. 3.2 have been performed are indicated in the plot.

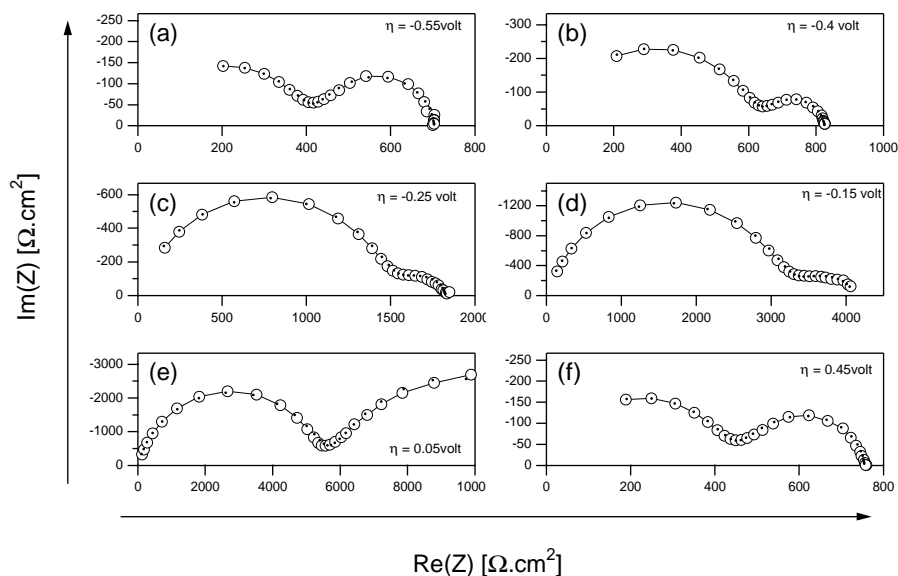


FIGURE 3.2. Electrochemical impedance of a (110) oriented electrode in a solution containing $0.01 \text{ M Fe(CN)}_6^{3-} / 0.01 \text{ M Fe(CN)}_6^{4-}$. $\eta = -0.55 \text{ volt}$ (a), $\eta = -0.4 \text{ volt}$ (b), $\eta = -0.25 \text{ volt}$ (c), $\eta = -0.15 \text{ volt}$ (d), $\eta = 0.05 \text{ volt}$ (e), $\eta = 0.45 \text{ volt}$ (f).

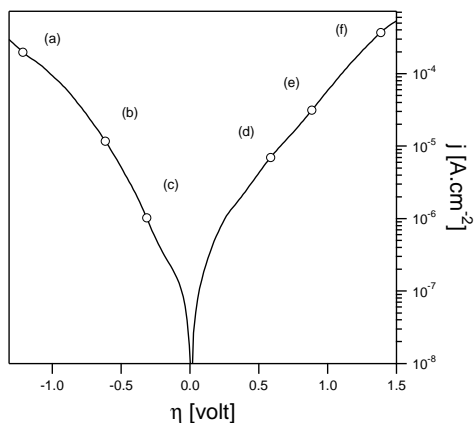


FIGURE 3.3. Current-potential characteristics of a (110) oriented electrode in a solution containing $0.01 \text{ M Fe}^{3+} / 0.01 \text{ M Fe}^{4+}$, plotted vs. overpotential ($\eta = V - V_{eq}$) on a logarithmic scale. The potentials at which the measurements shown in Fig. 3.4 were taken are indicated in the plot.

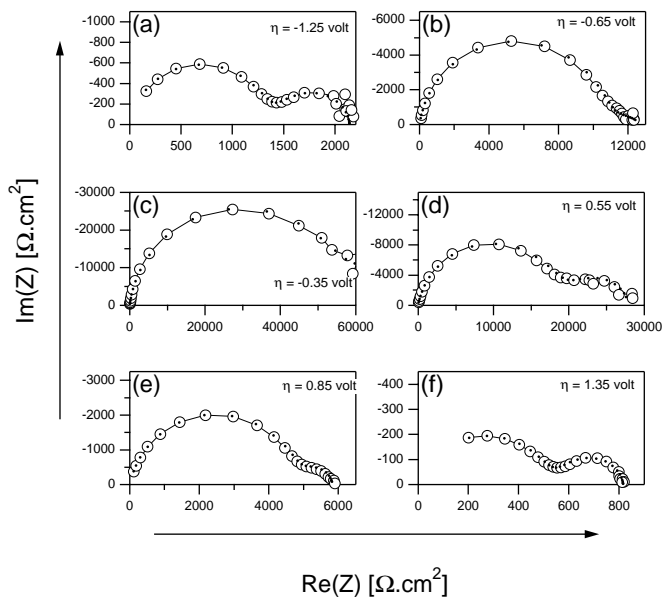


FIGURE 3.4. Electrochemical impedance of a (110) oriented electrode in a solution containing $0.01 \text{ M Fe}^{3+} / 0.01 \text{ M Fe}^{4+}$. $\eta = -1.25$ volt (a), $\eta = -0.65$ volt (b), $\eta = -0.35$ volt (c), $\eta = 0.55$ volt (d), $\eta = 0.85$ volt (e), $\eta = 1.35$ volt (f).

3.3 Discussion

From Figs. 3.1 and 3.3 it can be seen that $\log |j|$ rises steeply with increasing overpotential, until the current becomes limited due to transport of the oxidizing or reducing agent. For the $\text{Fe}(\text{CN})_6^{3-/4-}$ system, mass transport limitation is observed at an overpotential larger than 0.2 V (100-electrode), or 0.4 V (110-electrode), while 0.5 V is required for $\text{Fe}^{3+/2+}$ and 1.5 V for $\text{Ce}^{4+/3+}$ -solutions (both at 100-oriented electrodes). With $\text{Fe}^{3+/2+}$, diffusion limitation is not observed at the (110) electrode within the measured potential range (-1 to 2 V vs. SCE). Obviously, the $\text{Fe}(\text{CN})_6^{3-/4-}$ shows the most reversible, and $\text{Ce}^{4+/3+}$ the least reversible electrode kinetics. This is in agreement with what is observed at metal electrodes (see table 2.1, page 41).

The electrical impedance exhibits two distinct features in the [Im = neg], [Re = pos] quadrant, an RC-semicircle at relatively high frequencies and another feature in the lower frequency region, which can be described by an RC-semicircle deformed by a 45° 'onset' at higher frequencies. This onset dominates the second feature at large overpotentials, where the steady state current is limited by mass-transport (not shown).

The results given in chapter 2 of this thesis show that interfacial states are needed to explain the observed current-voltage behaviour. Fig. 3.5 introduces the model to explain the impedance results. We assume a uniform distribution of surface states $s(E)$ which mediate exchange of electrons between the valence band (VB) of p -type diamond and the redox system. The surface states exchange holes with the VB by a multiple tunneling process. Alternatively, the exchange may involve hopping [19], or inelastic, phonon-assisted tunneling [20].

To calculate the admittance we denote the electrical flux due to electrons tunneling from the valence band to empty surface states by j_c^{sc} ($j_c^{sc} < 0$), and that due to electrons tunneling from the surface states to empty states in the valence band (holes) by j_a^{sc} ($j_a^{sc} > 0$). Tunneling of electrons across the Helmholtz layer is assumed to occur iso-energetically and will be described in terms of the Marcus-Gerischer model [21, 22]. The electrical flux due to electrons passing from the occupied surface states to the empty levels of the oxidized species in solution (Ox) is denoted by j_c^H ($j_c^H < 0$); the flux of electrons tunneling from the reduced species in the solution (Red) is denoted by j_a^H ($j_a^H > 0$). The model does not account for concentration polarisation as this complicates the calculation considerably. Throughout the calculation we will use the notation and some of the results of the model introduced by Vanmaekelbergh [15, 18].

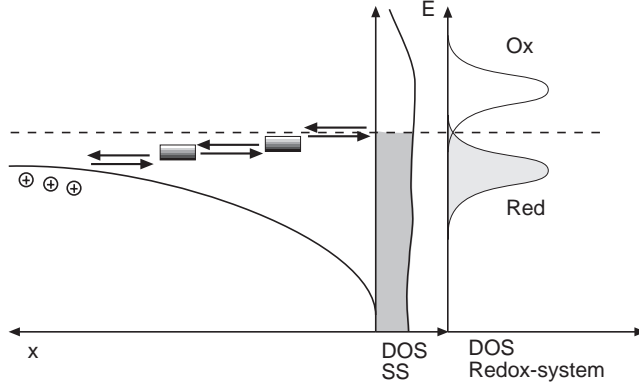


FIGURE 3.5. Model for charge transfer at the diamond/electrolyte interface. Surface states having a continuous distribution of surface states act as mediator for charge transfer between the diamond electrode and the redox system.

The surface charge of the diamond electrode due to occupied surface states is:

$$\Gamma = e \int_{E_V}^{E_F} s(E) \theta(E) dE \quad (3.1)$$

in which $s(E)$ is the density of interfacial bandgap states per unit of energy ($\text{cm}^{-2} \text{eV}^{-1}$), and θ is the occupancy of these states by electrons. The time derivative of the total surface charge is given by:

$$\frac{d\Gamma}{dt} = e \frac{d}{dt} \left[\int_{E_V}^{E_F} s(E) \theta(E) dE \right] = -j_c^{sc} - j_a^{sc} + j_c^H + j_a^H \quad (3.2)$$

If s does not depend strongly on energy, and if the surface state occupancy can be approximated by a function that has a value of one up to E_F and zero above E_F , eqn. 3.2 can be rewritten as :

$$\frac{d\Gamma}{dt} = es(E) \frac{d(E_F - E_V)}{dt} \quad (3.3)$$

In Appendix A, the electrochemical impedance corresponding to the model introduced above, is calculated by applying Kirchoff's law, and solving the partial differentials of the current and the surface charge with respect to the potential

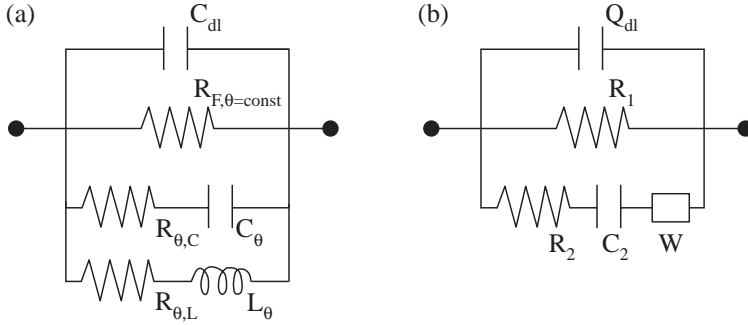


FIGURE 3.6. (a) Equivalent scheme corresponding to charge transfer via surface states [18] (b) Equivalent scheme used to fit the results in Figs. 3.2, 3.4 and 3.7.

drop in the depletion and in the Helmholtz layer. The electrical equivalent circuit resulting from this calculation is shown in Fig 3.6a. The physical meaning of the elements will be discussed in the Appendix and below. It has to be remarked here that the $(R_{\theta,C}, C_{\theta})$ and $(R_{\theta,L}, L_{\theta})$ branches correspond to one loop in the impedance, since the time constant of both branches is the same [18]. Because of this they could be replaced by a single RC series connection (see Fig. 3.6b) whose time constant is:

$$\tau^{-1} = (R_{\theta}C_{\theta})^{-1} = [C_H + C_{sc}]^{-1} \frac{e}{k_B T} [(1 - \alpha)j_a^H + \alpha(-j_c^H) + \beta(j_a^{sc} - j_c^{sc})] \quad (3.4)$$

α and $(1 - \alpha)$ are the cathodic and anodic partial charge transfer coefficients for the reaction between the surface states and the redox-couple in solution and β is a coefficient determined by the exact nature of the tunneling process through the depletion layer between states in the valence band and the surface states. Furthermore, it is possible to calculate the Faradaic resistance for potentials sufficiently far from equilibrium:

$$R_F^{-1} = \frac{e}{k_B T} |j| \left(\frac{\beta[1-\alpha]}{[1-\alpha]+\beta} \right) \quad , \text{ anodic overpotential} \quad (3.5)$$

$$R_F^{-1} = \frac{e}{k_B T} |j| \left(\frac{\beta\alpha}{\alpha+\beta} \right) \quad , \text{ cathodic overpotential} \quad (3.6)$$

The experimental results could be fitted (see figures 3.2 and 3.4) by using the above mentioned equivalent circuit with a Warburg impedance added (to ac-

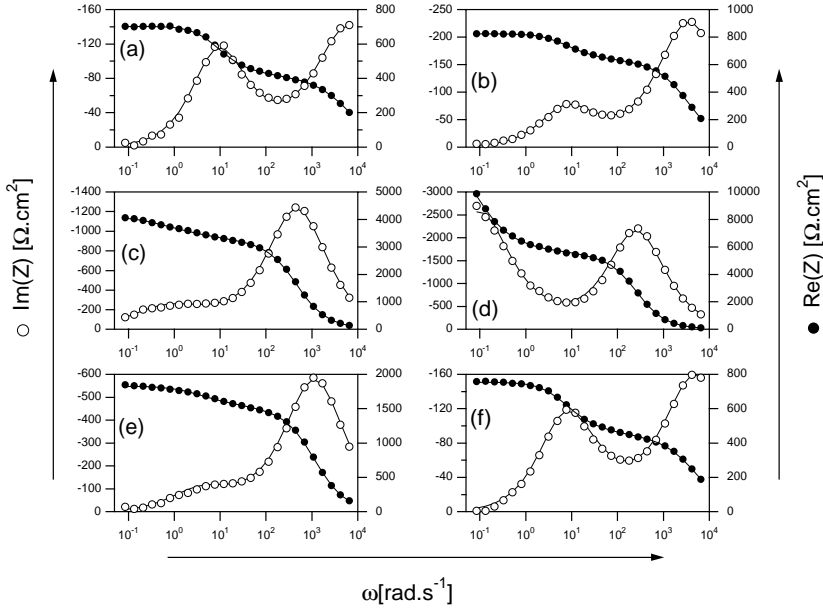


FIGURE 3.7. Bode representation of the results presented in Figs. 3.2. a-f together with fits to the equivalent scheme presented in Fig. 3.6b. The fits are presented by continuous lines.

count for concentration polarization effects), and the double layer capacitance replaced by a dispersive element (see Fig. 3.6b). Unfortunately, the somewhat arbitrary inclusion of the Warburg impedance (Fig. 3.6b) may cause a problem in the interpretation of τ^{-1} ; if the current is close to diffusion limitation τ^{-1} can differ from the value expected on the basis of equation 3.4. Because of this, we expect that equations 3.4, 3.5, and 3.6 will not be obeyed in the case of “fast” couples. A discussion of the origin of the frequency dispersion in the double layer capacitance can be found in chapter 2. In Fig. 3.7 a-f the results corresponding to Figs 3.2. a-f are represented as $\text{Im}[Z]$ and $\text{Re}[Z]$ vs. frequency, together with fits to the equivalent circuit presented in Fig. 3.6b. It is clear that the experimental results are well described by the modified circuit (Fig. 3.6b).

These results also suggest several tests of the model. At large anodic or cathodic overpotentials j_a^H and j_c^H can be approximated by $|j|$, so that, if α does not depend on electrode potential and β is not a strong function of potential, τ^{-1} should scale with $|j|$. Fig. 3.9a plots τ^{-1} for the measurements in the solution

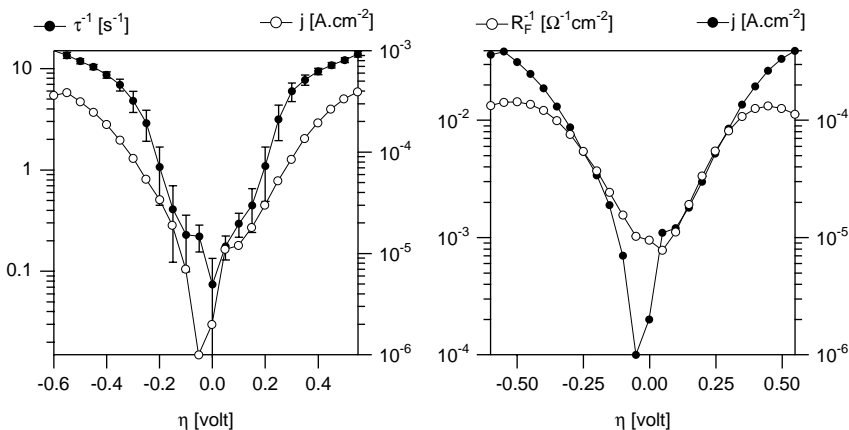


FIGURE 3.8. (a): Inverse time constant for the relaxation of surface states (left axis) as derived from the fits to the model circuit (Fig. 3.6b) of the data presented in Figs. 3.2a-f. The right axis shows the steady state current measured during the same experiment. The log axes show an equal number of decades for both the time constant and the steady state current. The error-bars are determined from the non-linear least squares fits. (b): R_F^{-1} (left axis). The right axis again shows the steady state current measured during the same experiment.

containing $\text{Fe}^{3+/2+}$ (Fig. 3.4). τ^{-1} clearly scales with $|j|$. From equation 3.4, it is possible to obtain a value for the Helmholtz layer capacitance, assuming that $C_{sc} \ll C_H$, $\alpha \approx 1/2$, and $\beta \approx 1/2$. From the results using $\text{Fe}^{3+/2+}$ a value of about $5 \times 10^{-5} \text{ F.cm}^{-2}$ follows. This is probably a reasonable value for a semiconductor electrolyte interface. The model also predicts that the inverse Faradaic resistance (R_1 in the scheme in Fig.3.6b) should also scale with the steady state current (equations 3.5 and 3.6). Fig. 3.9b shows that for the $\text{Fe}^{3+/2+}$ couple this is the case. Furthermore, we can check the constants of proportionality of R_F^{-1} to $|j|$. $R_F^{-1}/|j|$ is expected to be about 10 V^{-1} for $\alpha = 1/2$ and $\beta = 1/2$. In the case of $\text{Fe}^{3+/2+}$, a value of 8 V^{-1} is found, in accordance with the expectations.

Both tests yield unrealistic values in the case of $\text{Fe}(\text{CN})_6^{3-/4-}$ ($10^{-3} \text{ F.cm}^{-2}$ for C_H , and 100 V^{-1} for $R_F^{-1}/|j|$). This might be due to the fact that with $\text{Fe}(\text{CN})_6^{3-/4-}$ the current becomes mass transport limited even at modest overpotentials. Furthermore, equations 3.4, 3.5, and 3.6 predict a direct proportionality with the steady state current only if current in one direction can be neglected.

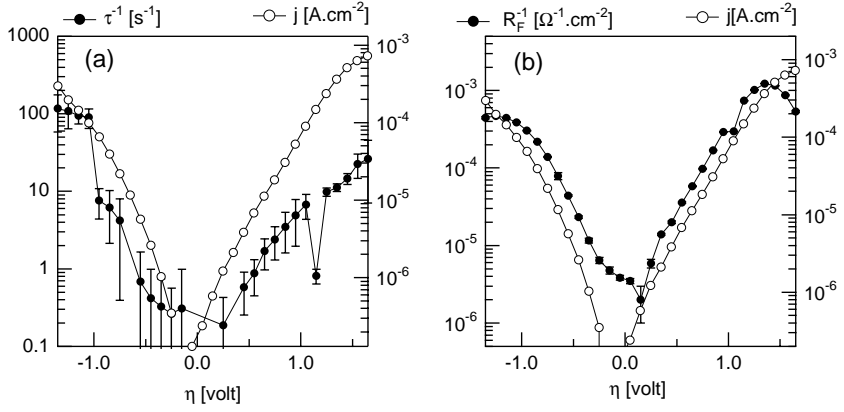


FIGURE 3.9. (a): Inverse time constant for the relaxation of surface states (left axis) as derived from the fits to the model circuit (Fig. 3.6b) of the data presented in Figs. 3.4a-f. The right axis shows the steady state current measured during the same experiment. The log axes show an equal number of decades for both the time constant and the steady state current. The error-bars are determined from the non-linear least squares fits. (b): R_F^{-1} (left axis). The right axis again shows the steady state current measured during the same experiment.

Therefore, the approximation does not apply if the overpotential is low. Both of the problems mentioned above lead to an underestimation of the current, which leads to an overestimation of C_H and $R_F^{-1}/|j|$.

We can only speculate about the nature of the surface states. Our measurements indicate that an intermediate state must be present at, or around the surface, in which charge can be stored. Candidates for such states are defects caused by growth phenomena, dangling bonds, H- or OH-groups, and impurity states (caused, for example, by B or N) near the surface.

3.4 Conclusions

The mechanism of charge transfer between homoepitaxial layers of CVD-grown diamond and simple one-electron redox systems has been investigated using electrochemical impedance spectroscopy. It was shown that the results can be

fitted using a scheme determined for charge transfer mediated by surface states. A theoretical description, derived for the impedance on the basis of a model proposed by Vanmaekelbergh [18], accounts for the results. Further research should cover a wider range of redox systems and doping densities, and elucidate the nature of the surface states involved in charge transfer.

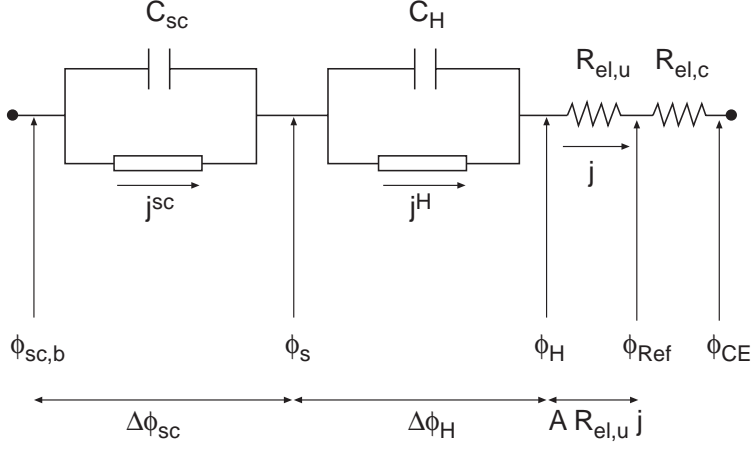


FIGURE 3.10. Scheme showing current and potential definitions used to calculate the impedance. For an explanation of the symbols see the text. Note that this scheme does not represent the actual impedance, as described by the schemes in Figs. 3.6.a-b.

Appendix A

The electrochemical cell with the diamond working electrode is shown schematically in Fig.3.10, in which:

$$\Delta\phi_{sc} = \phi^{sc,b} - \phi_s (< 0 \text{ for } p\text{-type diamond})$$

$$\Delta\phi_H = \phi^s - \phi_H$$

$$\Delta\phi = \Delta\phi_{sc} + \Delta\phi_H \quad (\text{A.1})$$

$\Delta\phi_H$ and $\Delta\phi_{sc}$ is the potential drop over the Helmholtz layer and depletion layer, respectively.

The potential of the diamond electrode with respect to the reference is:

$$\begin{aligned} V - V_{\text{Ref}} &= -\frac{1}{e} [E_F - E_{F,\text{Ref}}] = \phi_{sc,b} - \phi_{\text{Ref}} \\ &= \Delta\phi + A j R_{el,u} - (\phi_{\text{Ref}} - \phi_{\text{solution}}) \end{aligned} \quad (\text{A.2})$$

in which $R_{el,u}$ is the uncompensated electrolyte resistance (usually $\approx 10\Omega$), ϕ_{Ref} is the potential experienced by electrons in the metal wire inside the reference electrode, and $\phi_{solution}$ is the potential at the tip of the reference electrode.

Since $(\phi_{Ref} - \phi_{solution})$ is a constant determined solely by the thermodynamics of the reference electrode, it follows from eqn. A.2 that:

$$dV = -\frac{1}{e}dE_F = d\Delta\phi + AR_{el,u}dj \quad (A.3)$$

If $AR_{el,u}$ is sufficiently small,

$$dV = -\frac{1}{e}dE_F \approx d\Delta\phi \quad (A.4)$$

Application of Kirchoff's law gives :

$$j = j^H + C_H \frac{d\Delta\phi_H}{dt} \quad (A.5)$$

and :

$$j^{sc} + C_{sc} \frac{d\Delta\phi_{sc}}{dt} = j^H + C_H \frac{d\Delta\phi_H}{dt} \quad (A.6)$$

with :

$$\begin{aligned} j^{sc} &= j_c^{sc} + j_a^{sc} & (j_c^{sc} < 0, j_a^{sc} > 0) \\ j^H &= j_c^H + j_a^H & (j_c^H < 0, j_a^H > 0) \end{aligned}$$

On substitution of (A.1) in (A.6) it is found that :

$$\frac{d\Delta\phi_H}{dt} = (1 - \gamma_H) \frac{d\Delta\phi}{dt} + \frac{j^{sc} - j^H}{C_H + C_{sc}} \quad (A.7)$$

$$\text{with } \gamma_H = \frac{C_H}{C_H + C_{sc}} \quad (A.8)$$

Substitution of (A.7) in (A.5) gives :

$$j = (1 - \gamma_H)j^H + \gamma_H j^{sc} + C_{dl} \frac{d\Delta\phi}{dt} \quad (A.9)$$

in which C_{dl} is the total capacitance of the double layer ($C_H C_{sc} / (C_H + C_{sc})$). At equilibrium: $j^H \equiv 0$, $j^{sc} \equiv 0$, $d\Delta\phi/dt \equiv 0$. For a steady-state sufficiently far from equilibrium: $j^H \equiv j^{sc}$, $d\Delta\phi/dt \equiv 0$. Multiplying eqn. (A.7) by dt , using eqn. (3.2) and dividing by $d\Delta\phi$ gives :

$$\frac{d\Delta\phi_H}{d\Delta\phi} = (1 - \gamma_H) - \frac{1}{C_H + C_{sc}} \frac{d\Gamma}{d\Delta\phi} \quad (\text{A.10})$$

Γ is the total surface charge of the electrode and is given by eqn. (3.1); its time derivative is given by eqn. (3.2). Equation (A.10) is the equivalent of equation (54) in Ref. [15] for a wide distribution of surface states.

We derive the interfacial admittance starting from equation (A.5) (the small amplitude modulation of the respective variables is denoted by a superior tilde):

$$\tilde{j} = \tilde{j}^H + i\omega C_H \Delta\tilde{\phi}_H$$

, hence :

$$\begin{aligned} \frac{\tilde{j}}{\Delta\phi} &= \frac{\tilde{j}^H}{\Delta\phi} + i\omega C_H \frac{\Delta\tilde{\phi}_H}{\Delta\phi} \\ &= \left(\frac{\partial j^H}{\partial \Delta\phi_{sc}} \right)_{\Delta\phi_H} \times \left(1 - \frac{\Delta\tilde{\phi}_H}{\Delta\phi} \right) + \left(\frac{\partial j^H}{\partial \Delta\phi_H} \right)_{\Delta\phi_{sc}} \times \frac{\Delta\tilde{\phi}_H}{\Delta\phi} + i\omega C_H \frac{\Delta\tilde{\phi}_H}{\Delta\phi} \end{aligned} \quad (\text{A.11})$$

In principle, we should also consider concentration polarization. For reasons of simplicity we will not attempt this in the present paper. A generalised treatment of the role of concentration polarization in charge transfer reactions at semiconductor electrodes can be found in Ref. [23].

$\frac{\Delta\tilde{\phi}_H}{\Delta\phi}$ is calculated from eqn. (A.10)

$$\frac{\Delta\tilde{\phi}_H}{\Delta\phi} = (1 - \gamma_H) - [C_H - C_{sc}]^{-1} \frac{\tilde{\Gamma}}{\Delta\tilde{\phi}} \quad (\text{A.12})$$

Substitution of (A.12) into (A.11) gives:

$$\begin{aligned} Y(\omega) &= i\omega C_{dl} + \gamma_H \left(\frac{\partial j^H}{\partial \Delta\phi_{sc}} \right)_{\Delta\phi_H} + (1 - \gamma_H) \left(\frac{\partial j^H}{\partial \Delta\phi_H} \right)_{\Delta\phi_{sc}} \\ &\quad + \frac{-\tilde{\Gamma}}{\Delta\tilde{\phi}(C_H + C_{sc})} \left[i\omega C_H + \left(\frac{\partial j^H}{\partial \Delta\phi_H} \right)_{\Delta\phi_{sc}} - \left(\frac{\partial j^H}{\partial \Delta\phi_{sc}} \right)_{\Delta\phi_H} \right] \end{aligned} \quad (\text{A.13})$$

Equation (A.13) shows that the total interfacial admittance corresponds to an equivalent circuit with the double layer capacitance parallel to a resistance and a complex element. In this circuit the resistance corresponds to the Faradaic resistance with Γ constant. The complex element (Y_Γ) accounts for the impedance due to charge relaxation in the surface states. To derive the admittance, we have to calculate the complex term : $\frac{-\tilde{\Gamma}}{\Delta\tilde{\phi}(C_H+C_{sc})}$. We note that $\frac{d\Gamma}{dt}$ is a function of both $\Delta\phi_{sc}$ and $\Delta\phi_H$ and develop $\frac{d\Gamma}{dt}$ as :

$$\frac{d\Gamma}{dt} = F(\Delta\phi_{sc}, \Delta\phi_H) = \left(\frac{\partial F}{\partial \Delta\phi_{sc}} \right)_{\Delta\phi_H} d\Delta\phi_{sc} + \left(\frac{\partial F}{\partial \Delta\phi_H} \right)_{\Delta\phi_{sc}} d\Delta\phi_H \quad (A.14)$$

or for the harmonic component of the surface charge:

$$\frac{1}{\Delta\tilde{\phi}} \frac{d\tilde{\Gamma}}{dt} = i\omega \frac{\tilde{\Gamma}}{d\Delta\tilde{\phi}} = \left(\frac{\partial F}{\partial \Delta\phi_{sc}} \right)_{\Delta\phi_H} \frac{\Delta\tilde{\phi}_{sc}}{\Delta\tilde{\phi}} + \left(\frac{\partial F}{\partial \Delta\phi_H} \right)_{\Delta\phi_{sc}} \frac{\Delta\tilde{\phi}_H}{\Delta\tilde{\phi}} \quad (A.15)$$

Substitution of eqn. (A.12) into (A.15) yields after rearrangement:

$$\frac{-\tilde{\Gamma}}{\Delta\tilde{\phi}(C_H + C_{sc})} = \frac{\gamma_H \left(\frac{-\partial F}{\partial \Delta\phi_{sc}} \right)_{\Delta\phi_H} + (1 - \gamma_H) \left(\frac{-\partial F}{\partial \Delta\phi_{sc}} \right)_{\Delta\phi_H}}{\left[i\omega(C_H + C_{sc}) + \left(\frac{-\partial F}{\partial \Delta\phi_{sc}} \right)_{\Delta\phi_H} + \left(\frac{\partial F}{\partial \Delta\phi_H} \right)_{\Delta\phi_{sc}} \right]} \quad (A.16)$$

The third component of the interfacial admittance becomes:

$$Y_\Gamma = \left\{ \gamma_H \left(\frac{-\partial F}{\partial \Delta\phi_{sc}} \right)_{\Delta\phi_H} + (1 - \gamma_H) \left(\frac{-\partial F}{\partial \Delta\phi_{sc}} \right)_{\Delta\phi_H} \right\} \times \frac{i\omega\gamma_H + (C_H + C_{sc})^{-1} \left[\left(\frac{\partial j^H}{\partial \Delta\phi_H} \right)_{\Delta\phi_{sc}} - \left(\frac{\partial j^H}{\partial \Delta\phi_{sc}} \right)_{\Delta\phi_H} \right]}{i\omega + (C_H + C_{sc})^{-1} \left[\left(\frac{-\partial F}{\partial \Delta\phi_{sc}} \right)_{\Delta\phi_H} + \left(\frac{\partial F}{\partial \Delta\phi_H} \right)_{\Delta\phi_{sc}} \right]} \quad (A.17)$$

This component corresponds to an (R,C) series connection parallel to an (R,L) series connection with a single time constant for the relaxation of the surface charge. This time constant (τ) is given by:

$$\tau^{-1} = (C_H + C_{sc})^{-1} \left[\left(\frac{-\partial F}{\partial \Delta\phi_{sc}} \right)_{\Delta\phi_H} + \left(\frac{\partial F}{\partial \Delta\phi_H} \right)_{\Delta\phi_{sc}} \right] \quad (A.18)$$

To relate elements derived from our fits to physical quantities all the partial derivatives in the expression for the admittance are required. For this we need equation (3.2). If the density of surface states is not a strong function of energy in the energy range of interest we can use equation (3.3), and rewrite it as follows:

$$d\Gamma \approx esd(E_F - E_V) = -e^2 sd\Delta\phi_{sc} \quad (\text{A.19})$$

Calculation of the partial derivatives

We can assume that j^H does not depend strongly on $\Delta\phi_{sc}$ hence $\left(\frac{\partial j^H}{\partial \Delta\phi_{sc}}\right)_{\Delta\phi_H} \approx 0$. Furthermore, we can formally write $\left(\frac{\partial j^{sc}}{\partial \Delta\phi_{sc}}\right)_{\Delta\phi_H}$ as $;\frac{e}{k_B T} \beta (j_a^{sc} - j_c^{sc})$. β in this equation is a constant determined by the exact nature of the tunneling process through the depletion layer, and the density of surface states as a function of energy. We assumed that the ‘tunneling’ process has the same potential dependence for both directions. We can now write:

$$\begin{aligned} \left(\frac{-\partial F}{\partial \Delta\phi_{sc}}\right)_{\Delta\phi_H} &= \left[\frac{-\partial\{j^H - j^{sc}\}}{\partial \Delta\phi_{sc}}\right]_{\Delta\phi_H} = \left(\frac{\partial j^{sc}}{\partial \Delta\phi_{sc}}\right)_{\Delta\phi_H} \\ &= \frac{e}{k_B T} \beta (j_a^{sc} - j_c^{sc}) \end{aligned} \quad (\text{A.20})$$

and, since j^{sc} does not depend on $\Delta\phi_H$:

$$\begin{aligned} \left(\frac{\partial F}{\partial \Delta\phi_H}\right)_{\Delta\phi_{sc}} &= \left[\frac{\partial\{j^H - j^{sc}\}}{\partial \Delta\phi_H}\right]_{\Delta\phi_{sc}} = \left(\frac{\partial j^H}{\partial \Delta\phi_H}\right)_{\Delta\phi_{sc}} \\ &= \frac{e}{k_B T} [(1 - \alpha)j_a^H + \alpha(-j_c^H)] \end{aligned} \quad (\text{A.21})$$

$(1 - \alpha)$ and α in this equation are the transfer coefficients for the anodic and the cathodic process through the Helmholtz layer respectively. The total admittance can thus be written as:

$$\begin{aligned} Y(\omega) &= i\omega C_{dl} + (1 - \gamma_H) \frac{e}{k_B T} [(1 - \alpha)j_a^H + \alpha(-j_c^H)] \\ &+ \left\{ \gamma_H \frac{e}{k_B T} (j_a^{sc} - j_c^{sc}) - (1 - \gamma_H) \frac{e}{k_B T} [(1 - \alpha)j_a^H + \alpha(-j_c^H)] \right\} \\ &\times \frac{i\omega\gamma_H + (C_H + C_{sc})^{-1} \left\{ \frac{e}{k_B T} [(1 - \alpha)j_a^H + \alpha(-j_c^H)] \right\}}{i\omega + (C_H + C_{sc})^{-1} \frac{e}{k_B T} [(1 - \alpha)j_a^H + \alpha(-j_c^H) + \beta(j_a^{sc} - j_c^{sc})]} \end{aligned} \quad (\text{A.22})$$

This impedance corresponds to the scheme presented in Fig. 3.6. By taking the limit $\omega \rightarrow 0$ we can calculate the Faradaic resistance:

$$\begin{aligned} \lim_{\omega \rightarrow 0} (Y(\omega)) &= R_F^{-1} = (1 - \gamma_H) \frac{e}{k_B T} [(1 - \alpha)j_a^H + \alpha(-j_c^H)] \\ &+ \left\{ \gamma_H \frac{e}{k_B T} (j_a^{sc} - j_c^{sc}) - (1 - \gamma_H) \frac{e}{k_B T} [(1 - \alpha)j_a^H + \alpha(-j_c^H)] \right\} \\ &\times \frac{[(1 - \alpha)j_a^H + \alpha(-j_c^H)]}{[(1 - \alpha)j_a^H + \alpha(-j_c^H) + \beta(j_a^{sc} - j_c^{sc})]} \end{aligned} \quad (A.23)$$

If we assume that β is of the same order of magnitude as α , and $C_{sc} \ll C_H$, (A.23) reduces to:

$$R_F^{-1} = \frac{e}{k_B T} \beta (j_a^{sc} - j_c^{sc}) \times \frac{[(1 - \alpha)j_a^H + \alpha(-j_c^H)]}{[(1 - \alpha)j_a^H + \alpha(-j_c^H) + \beta(j_a^{sc} - j_c^{sc})]} \quad (A.24)$$

At potentials sufficiently far from equilibrium and with $\gamma_H \approx 1$ we can approximate (A.24):

$$R_F^{-1} = \frac{e}{k_B T} |j| \left(\frac{\beta[1 - \alpha]}{[1 - \alpha] + \beta} \right) \quad , \text{ anodic overpotential} \quad (A.25)$$

$$R_F^{-1} = \frac{e}{k_B T} |j| \left(\frac{\beta\alpha}{\alpha + \beta} \right) \quad , \text{ cathodic overpotential} \quad (A.26)$$

It is also very instructive to calculate the Faradaic resistance at equilibrium from equation (A.24). If in this case $2\beta j_{eq}^{sc} \gg j_{eq}^H$ eqn. (A.24) reduces to : $R_F^{-1} = (e/k_B T) j_{eq}^H$, the classic case for charge transfer at a metal electrode. This means that when charge transfer through the depletion layer is not in any way rate limiting, the kinetics of the total charge transfer reaction appear to be “metallic”. In the other limiting case ($2\beta j_{eq}^{sc} \ll j_{eq}^H$), eqn. (A.24) reduces to : $R_F^{-1} = (e/k_B T) \beta 2j_{eq}^{sc}$; the Faradaic resistance at equilibrium is only dependent on the kinetics of tunneling through the depletion layer, the concentration of valence band holes, and the concentration of surface states.

It can be shown that [18], within reasonable limits for the relevant parameters, the third part of the impedance will not be inductive. This allows the third part to be represented by an (RC) series connection with a single time constant τ . Because R from the RL series connection contributes to the Faradaic resistance, we must replace the resistance that is part of the first part of the admittance by the Faradaic resistance as calculated in equation (A.23). From equation (A.22) it follows that:

$$\tau^{-1} = [C_H + C_{sc}]^{-1} \frac{e}{k_B T} [(1 - \alpha)j_a^H + \alpha(-j_c^H) + \beta(j_a^{sc} - j_c^{sc})] \quad (\text{A.27})$$

References

- [1] Y. V. Pleskov, A. Y. Sakharova, M. D. Krotova, L. L. Bouilov, and B. V. Spitsyn, *J. Electroanal. Chem.* **228**, 19 (1987).
- [2] P. M. Natishan and A. Morrish, *Mater. Lett.* **8**, 269 (1989).
- [3] G. M. Swain, *J. Electrochem. Soc.* **141**, 3382 (1994).
- [4] H. B. Martin, A. Argoitia, U. Landau, A. B. Anderson, and J. C. Angus, *J. Electrochem. Soc.* **144**, L133 (1996).
- [5] R. DeClements, B. L. Hirsche, M. C. Granger, J. Xu, and G. M. Swain, *J. Electrochem. Soc.* **143**, L150 (1996).
- [6] N. Vinokur, B. Miller, Y. Avyigal, and R. Kalish, *J. Electrochem. Soc.* **143**, L238 (1996).
- [7] S. Alhashem, F. Chambers, J. W. Strojek, G. M. Swain, and R. Ramesham, *Anal. Chem.* **67**, 2812 (1995).
- [8] J. Xu, M. C. Granger, Q. Chen, J. W. Strojek, T. E. Lister, and G. M. Swain, *Anal. Chem. News & Feat.* **Oct. 1**, 591A (1997).
- [9] R. Ramesham and M. F. Rose, *Thin Solid Films* **300**, 144 (1997).
- [10] S. Alhashem, M. Granger, J. Xu, and G. M. Swain, Extended abstracts of the 187th - meeting of the electrochemical society, Reno, 860 (1995).
- [11] G. M. Swain, *Adv. Mater.* **6**, 388 (1994).
- [12] S. Yang, J. Zhu, Y. Yao, and Z. Zhang, *Advances in new diamond science and technology*, MYU, Tokyo, 741 (1994).
- [13] A. D. Modestov, Y. E. Evstefeeva, Y. U. Pleskov, V. M. Mazin, V. P. Varnin, and I. G. Teremetskaya, *J. Electroanal. Chem.* **431**, 211 (1997).
- [14] J. van de Lagemaat, G. Z. Cao, G. Jansen, D. Vanmaekelbergh, and J. J. Kelly, *Electrochem. Soc. Proc.* **95-21**, 103 (1995).
- [15] D. Vanmaekelbergh, *Electrochim. Acta* **42**, 1121 (1997).
- [16] G. Oskam, D. Vanmaekelbergh, and J. J. Kelly, *Electrochim. Acta* **38**, 1115 (1993).
- [17] S. N. Frank and A. J. Bard, *J. Am. Chem. Soc.* **97**, 7427 (1975).
- [18] D. Vanmaekelbergh, *Electrochim. Acta* **42**, 1135 (1997).
- [19] E. P. Visser, G. J. Bauhuis, G. Janssen, W. Vollenberg, W. J. P. van Enckevort, and L. J. Giling, *J. Phys.: Condens. Matt.* **4**, 7365 (1992).
- [20] R. Wiesendanger, *Scanning Probe Microscopy and Spectroscopy* (Cambridge University Press, Cambridge, 1994).
- [21] R. A. Marcus, *Angew. Chem. Int. Ed. Engl.* **32**, 1111 (1993).
- [22] H. Gerischer, *J. Phys. Chem.* **95**, 1356 (1991).

- [23] Z. Hens and W. P. Gomes, J. Phys. Chem. B **101**, 5814 (1997).

Chapter 4

Photoelectrochemical characterization of 6H-SiC

Abstract

Photoelectrochemical methods were used to characterize *n*-type 6H-SiC. The double layer capacitance obeyed the Mott-Schottky relationship over a large potential range (>6 volts band bending). The flatband-potential was found to depend on pH with a displacement of about 40 mV per unit pH. The minority carrier diffusion length determined from the potential dependence of the photocurrent was 30 nm. From the dependence of the photocurrent on the photon energy, the absorption coefficient $\alpha(h\nu)$ was determined using the Gärtner model. The results are in excellent agreement with spectra reported in literature. Sub-bandgap photocurrent with photons of energy down to 1.96 eV (≈ 1 eV below the bandgap) was also observed.

4.1 Introduction

Silicon carbide (SiC) has again become the focus of considerable attention because of its excellent material and electronic properties [1]. Current and potential uses of SiC include high-temperature and radiation-hard electronics, high power and high frequency devices, and opto-electronic applications such as blue-emitting diodes and UV-photodetectors. From the photoelectrochemical point of view, the interest has been in the field of photocatalysis [2, 3], water splitting [4, 5], photoetching of microstructures [6–8], chemomechanical polishing [9], and fundamental studies of electron exchange reactions between large bandgap semiconductors and one-equivalent redox-systems [10]. There is a need for suitable etching methods for SiC [3, 11, 12]; to date, no open circuit wet-chemical method is known [1]. Shor et al. showed that, using appropriate masking techniques and laser illumination, *n*-type SiC can be etched photoanodically yielding microstructures suitable for electronic applications [6]. The discovery of porous SiC by Shor et al., and the resulting improved photoluminescence has given the field an extra impulse [13–19]. Recently, we showed that the photon-to-current quantum efficiency for supra-bandgap light increases over several orders of magnitude upon porous etching (chapter 5 of this thesis, page 83 and [20]). It was shown that the increase in the sub-bandgap photocurrent yield is even more spectacular.

The growing interest in large bandgap semiconductors like SiC, GaN and diamond for use in opto-electronic applications stimulates fundamental research on their material properties. Photoelectrochemical techniques can provide essential information on the surface chemistry and properties such as the doping density and the minority carrier diffusion length. Unfortunately, research on SiC has either been performed on low-quality material (green coloured, indicating a large defect density) or using suspect contacting methods (e.g. In or Ga-In eutectics). The resulting uncertainty can easily be demonstrated by the large spread in flat-band potentials (V_{fb}) reported in literature. As can be seen from table 4.1, V_{fb} reported for acidic environments ranges from -1.25 to -0.7 volt vs. SCE.

There are several reports in the literature on the spectral response of SiC-photoanodes [3, 10, 11]. These measurements were performed in electrolyte solutions in which the semiconductor is photoanodically oxidized so that stability and reproducibility must be questioned. In the earliest work [10] a spectrum is only shown schematically. The measurements of Morisaki et al. [11] at high pH clearly suffer from oxide formation, as the authors themselves admit. In the most

TABLE 4.1. Flatband potentials vs. the Saturated Calomel Electrode (SCE) for 6H SiC as reported in the literature

pH	V_{fb}	solution	frequency	reference
0	-1.25	?	20 kHz	[3]
0.3	-0.9	0.5 M H_2SO_4	1 kHz	[12]
1	-0.7	?	?(method unknown)	[5]
1.3	-1.6	0.05 M H_2SO_4	250 kHz	[10]
13	-1.45→-1.65	0.1 M NaOH	1 kHz	[11]
13	-1.6	0.1 M NaOH	1 kHz	[12]
14	-1.8	?	20 kHz	[3]

recent work (Lauermann et al. [3]) the bandgap response is reproduced. However, a photocurrent is observed in almost the whole visible range, which does not inspire confidence in the quality of the material under study.

In this chapter, we present results on the photoelectrochemistry of high quality, low-doped, *n*-type 6H-SiC, obtained from Cree Research Inc. The quality of this material is illustrated by the fact that we could not observe anodic breakdown in HF solutions at a bias of up to 60 volts. The material we used in a previous publication [20] readily shows breakdown at about 5 volts. Furthermore, the material is colourless, as expected for a semiconductor with a bandgap of 3.1 eV [1]. As contacts we used Ti/Mo/Au or W/Au, which provide good Ohmic contacts [1].

Electrical impedance spectroscopy was used to determine the flat band potential (V_{fb}) in solutions of various pH values. The photocurrent was measured as a function of photon energy and applied potential in solutions containing an electron donor which is preferentially oxidized, thus preventing oxide formation. Results from these measurements yielded the absorption spectrum and the minority carrier diffusion length. These results are compared with those obtained from solid-state methods. Intensity-Modulated Photocurrent Spectroscopy (IMPS or opto-electrical admittance spectroscopy) experiments [21] were used to obtain insight into the mechanism of processes responsible for photocurrent losses (recombination). Finally, we report measurements of sub-bandgap photocurrent at energies as much as 1eV below the optical bandgap of 6H-SiC. The mechanism of the sub-bandgap photocurrent will be discussed.

4.2 Experimental

The 6H-SiC crystals were obtained from Cree Research Inc [22]. All measurements presented in this chapter were performed on squares (5×5 mm) cut from one colourless polished wafer with a listed doping density ($N_D - N_A$) of $8.2 \times 10^{16} \text{ cm}^{-3}$. The samples were provided with Ti/Mo/Au or W/Au contacts on the back (unpolished) side and were annealed at 750°C under nitrogen. This yields Ohmic contacts with a low contact resistance [1]. The samples were mounted with epoxy-resin in a PVC holder that could be used as a rotating electrode, with the polished Si (0001) face exposed to solution. Apiezon wax was used to protect the edges of the electrodes from exposure to the electrolyte.

The electrochemical set-up was a standard three electrode configuration, with the SiC as working electrode, a large Pt sheet as a counter electrode, and a saturated calomel electrode (SCE) as a reference ($V=0.242 \text{ V}$ vs. NHE). All potentials are given relative to SCE. The reference electrode was combined with a Pt-wire in parallel through a 20nF capacitor to avoid high frequency phase errors [23]. We used an EG&G PAR273A or PAR283 potentiostat, and a Solartron 1255a Frequency Response Analyzer (FRA). For the IMPS measurements an 8 W Coherent Innova 90 Argon-ion laser tuned at the 354 nm line was combined with an Isomet 1211 AOM to modulate the beam intensity by about 20%. The light intensity was monitored by a fast UV-sensitive photodiode. The laser beam was broadened using a beam expander to obtain uniform illumination of the SiC electrode. The light source used in the measurements of the wavelength dependence of the photocurrent yield was a 450 W high pressure Xe-lamp equipped with a Spex 1680 double-grating monochromator. Cut-off filters were used to absorb the high energy second order line of the monochromator in the long wavelength region of the spectra. For the sub-bandgap current measurements at 1eV below the optical bandgap of 6H-SiC, a 60 mW Spectra-Physics 127 He-Ne laser (632.8 nm \approx 1.96 eV) was employed.

All chemicals used were analytical grade. Solutions were prepared in doubly distilled water, and were deaerated by nitrogen or argon bubbling. Measurements were, in most cases, performed under thermostatic conditions at 25°C. For the photoelectrochemical experiments we used Fe^{2+} or ethanol containing solutions to prevent formation of thick oxide layers on the surface.

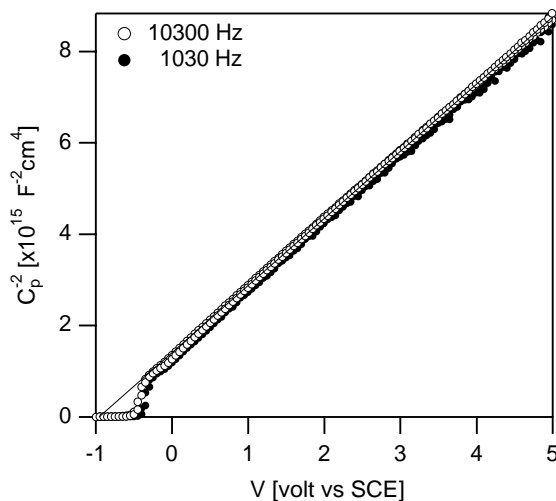


FIGURE 4.1. Plot of the inverse of the square of the parallel equivalent capacitance (C_p^{-2}) vs. electrode potential of 6H *n*-SiC in 1 M H₂SO₄. Measuring frequencies were 10.3 kHz and 1.03 kHz. The continuous line shows a linear fit.

4.3 Results and Discussion

4.3.1 Electrical Impedance Spectroscopy

Various papers report the results of electrical impedance measurements for the determination of doping density and flat band potentials of 6H-SiC. However all measurements of which we are aware were performed at only one frequency, which is extremely risky, especially for high defect density material. The doping density was not checked by an independent method so that comparison with the impedance method was not possible. The flat band potentials obtained from such measurements show a very large spread (see table 4.1). This is not surprising considering the electrode quality, the Ohmic contact (in some cases) and the reliance on a single measuring frequency. Furthermore, in many cases it was not clear which crystal face was exposed to the solution. Obviously, there can be a large difference between carbon and silicon faces.

Fig.4.1 shows our impedance results for *n*-type 6H-SiC in 1M H₂SO₄ solution (pH=0). The parallel equivalent capacitance (C_p) is plotted as C_p^{-2} vs. the applied potential V . The plots are linear up to 5 V and there is almost no frequency

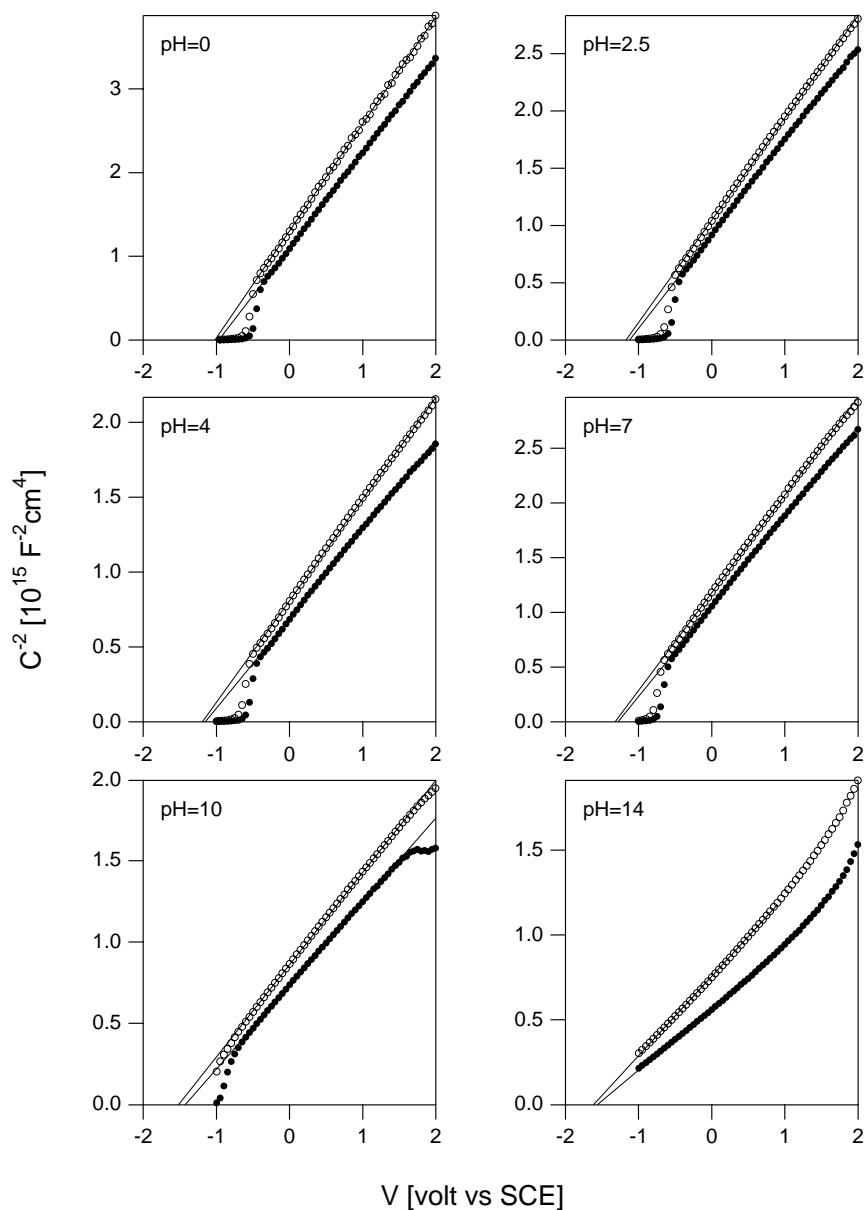


FIGURE 4.2. Overview of C_p^{-2} vs. V plots obtained at several pH values. Measuring frequencies were 10.3 kHz (open circles) and 1.03 kHz (filled circles). The continuous lines show linear fits. The solutions at intermediate pH values were buffered using phosphate.

dispersion. No appreciable current ($\ll 1$ nA) is observed in this range. The net doping density ($N_D - N_A$), obtained from the slope of the plot ($8.2 \cdot 10^{16} \text{ cm}^{-3}$), corresponds to the listed value. The error in the determination of the surface area and thus in the measured doping density is estimated to be about 5%. From Fig.4.1, it is also clear that, close to the flat-band potential, there is a considerable deviation from linearity. The capacitance at these potentials is much larger than that predicted by the Mott-Schottky theory. Such an increase of the capacitance can be explained by the presence of electronic surface states [24–26], which interact with majority carriers.

Fig.4.2 shows an overview of (C_p^{-2}, V) plots obtained at different values of solution pH. The intermediate pH values were obtained using phosphate buffers. Prior to each measurement the electrode was pretreated in 40%HF. This renders the surface of the electrode hydrophobic (H-terminated). After immersion in water the surface becomes hydrophilic, indicating the presence of OH groups. The (C_p^{-2}, V) plots are linear at all pH values. The frequency dispersion in these plots is slightly larger than in Fig.4.1. A shift of the flat-band potential to more negative values is observed as the pH is increased. In Fig.4.3 the flat-band potential obtained from the Mott-Schottky plots is plotted vs. pH. A linear fit (shown as a dot-dashed line) gives a pH dependence of 40 mV per unit pH. The dependence of V_{fb} on pH for 6H-SiC has previously been reported [3] but has not been examined in this detail. A pH dependence of the flat-band potential points to an adsorption/desorption equilibrium of protons or hydroxyl ions at the surface of the semiconductor, causing a change in the Helmholtz potential drop ($\Delta\phi_H$). Generally, a dependence of 59 mV per unit pH is expected. Indeed, this is often found for ionic semiconductors, and for covalent semiconductors covered with an oxide layer [24]. For strongly covalent semiconductors without an oxide V_{fb} is not expected to shift with pH. In the case of silicon (covered with a thin oxide), a weaker pH-dependence (30 mV per unit pH) is found [27], close to what we find with 6H-SiC. A Site-Binding model, developed by Yates et al. to explain this dependence [28], was worked out by Bousse et al. [29–31] (For an overview of the model see Ref. [32]). The Si-OH sites are assumed to be amphoteric, i.e. they can both accept a proton yielding an Si-OH_2^+ -group, and donate a proton, yielding a Si-O^- -group. The model relates the pH dependent part of the potential drop over the Helmholtz layer ($\Delta\phi'_H$) to pH via the following expression

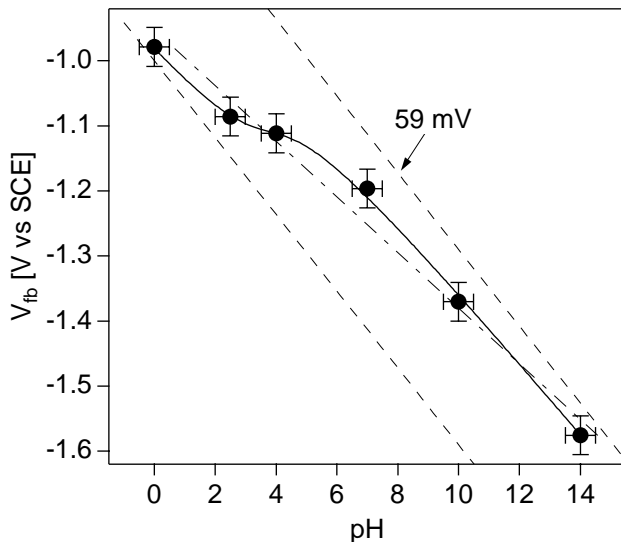


FIGURE 4.3. pH dependence of the flat-band potential. The points were taken from the x-axis intercepts of the plots of Fig.4.2. The error bars were estimated from the reproducibility of the experiments. The dashed lines have a slope of 59 mV per unit pH. The dot-dashed line is a linear fit of the points. The continuous line is a fit using equation (4.1).

$$2.303 (\text{pH}_{pzc} - \text{pH}) = \frac{e\Delta\phi'_H}{k_B T} + \sinh^{-1} \left(\frac{e\Delta\phi'_H}{k_B T} \frac{1}{\beta} \right) \quad (4.1)$$

pH_{pzc} is the pH at the point of zero charge and β , the sensitivity factor, is given by:

$$\beta = \frac{2e^2 N_s (K_a K_b)^{\frac{1}{2}}}{k_B T C_d} \quad (4.2)$$

in which N_s is the total density of sites at the interface between the oxide and the electrolyte, K_a and K_b are the acidity and the basicity constants of the Si-OH groups, and C_d the double layer capacitance. β can be seen as the reactivity of the surface: the higher β , the closer the pH dependence of V_{fb} will be to

59 mV. The continuous line in Fig. 4.3 shows a fit to equation 4.1 using the pH independent part of the potential drop over the Helmholtz layer at pH_{pzc} as an extra parameter. This parameter directly relates the flat-band potential to $\Delta\phi_H$ via $V_{fb} = \Delta\phi_H^0 + \Delta\phi_H$. The fit yields a value of 3.77 ± 0.36 for pH_{pzc} , and 0.28 ± 0.14 for β . Although it is clear that the number of experimental points is too low to draw firm conclusions, it is interesting to compare these results to those observed with SiO_2 (whose pH_{pzc} and β values are estimated to be about 2.2 and 0.14 respectively [30]). The value of β for SiO_2 is quite close to our value for SiC, indicating that the reactivity and the number of sites at the surface of the oxide are about the same as on SiO_2 . This result is not surprising since the oxide on the SiC surface probably resembles SiO_2 . The pH_{pzc} is different from that of SiO_2 .

Upon illumination of SiC at potentials positive from the flat band potential with the UV line (354 nm) of the Ar-laser, a reversible shift in the flat-band potential of about 0.12 volt to more positive potentials is observed. This implies that photogenerated holes are captured in surface states for a finite time, before being transferred to the solution; this leads to a shift of the Helmholtz potential. Such a photoanodic surface charge may induce surface recombination.

4.3.2 Photoelectrochemical measurements

When SiC is illuminated with UV light (354 nm Ar-laser), an anodic photocurrent is observed, that is strongly potential dependent. In Fig.4.4 the photocurrent is plotted as quantum yield (electrons per absorbed photon) vs. the depletion layer width, calculated from V_{fb} and $(N_D - N_A)$, obtained from the (C_p^{-2}, V) plot under illumination. At small band bending the quantum yield is low because of surface recombination. At higher band bending the plot shows a linear dependence on the depletion layer width. The absorption depth $1/\alpha$ at this wavelength ($20\mu\text{m}$) is still much larger than the sum of the depletion layer width W_{depl} ($\approx 100\text{nm}$) and the diffusion length L_p of holes; this results in a low quantum yield (10^{-3}). With $1/\alpha \gg W_{depl} + L_p$ the equation from the Gärtner model [33] reduces to:

$$\frac{j}{e\Phi} = 1 - \frac{\exp(-\alpha W_{depl})}{1 + \alpha L_p} = \frac{W + L_p}{1/\alpha} \quad (4.3)$$

The linear relationship observed at large band-bending implies that, at these potentials, only bulk recombination occurs. From the x -axis intercept of the linear part of the plot we can determine the minority carrier diffusion length (L_p),

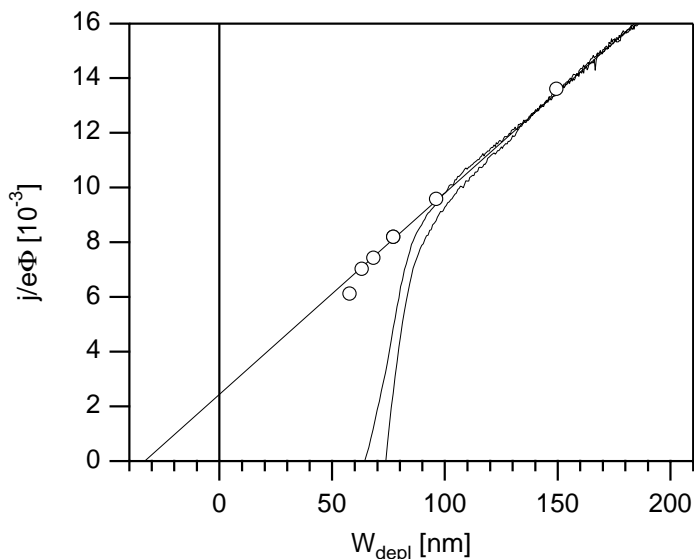


FIGURE 4.4. Plot of the photocurrent quantum yield vs. depletion layer width (obtained from the C_p^{-2} vs. V plot under illumination). The electrode was illuminated using the UV-line of an argon-ion laser (354 nm). The electrolyte was a 1M H_2SO_4 solution containing 0.05 M Fe^{2+} . The continuous line is a fit to the linear part of the curve ($W_{depl} > 110$ nm). The open circles show the high frequency limit obtained from the IMPS measurements (Fig. 4.5).

while the slope yields α [34–38]. L_p is found to be about 30 nm. This is at the low end of the range of values reported in the literature (30–144 nm [1, 39]).

4.3.3 IMPS-Measurements

IMPS-measurements were performed in the potential range in which the photocurrent quantum yield deviates from the limit expected from the Gärtner model. The results are shown in Fig.4.5 in the complex plane as a function of measuring frequency and applied potential. Y_{Im} , and Y_{Re} are the imaginary and the real parts of the opto-electrical admittance. Essentially, one flattened semi-circle is observed with a potential-dependent high and low frequency limit. As shown in Fig.4.4 by the open circles, the high frequency limit corresponds to the Gärtner-value, and reflects the fraction of the light absorbed in the retrieval layer of width $W_{depl} + L_p$. The radius of the semicircle corresponds to the part of the

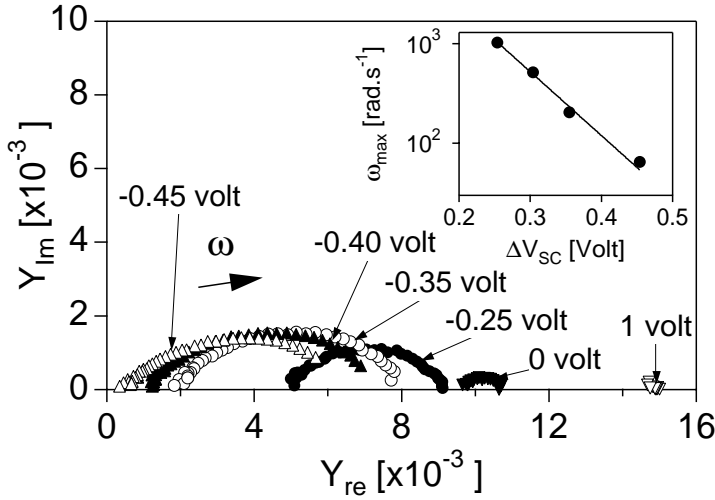


FIGURE 4.5. IMPS plots of 6H *n*-SiC in 1M H₂SO₄ solution containing 0.05 M Fe²⁺. Y_{Re} and Y_{Im} are the real and the imaginary parts of the opto-electrical admittance. The potentials at which the measurements were taken are indicated by arrows. The frequency increases from left to right for each 'semicircle'. Measurement frequencies ranged from 0.1 Hz to 10 kHz. The insert shows the frequencies at which the IMPS plot shows a maximum plotted vs. V_{sc} ($=V-V_{fb}$).

photocurrent that is lost by recombination via surface states or in the depletion layer [34, 40–44]. Since the high-frequency limit of the opto-electrical admittance plotted vs. the depletion layer width in Fig.4.4 agrees with the Gärtner relationship, it can be concluded that recombination in the depletion layer is negligible compared to recombination via surface states.

The characteristic frequency (ω_{max}) at which the opto-electrical admittance shows a maximum depends on the electrode potential. The inset in Fig.4.5 shows that ω_{max} decreases with decreasing band-bending. According to the model of Vanmaekelbergh [41], $\omega_{max} = \beta_n n_s + \beta_p p_s$, where β_n and β_p are the rate constants for electron and hole capture in the surface states, and n_s and p_s the surface concentrations of electrons and holes. If $\beta_n n_s \gg \beta_p p_s$, ω_{max} is expected to decrease with decreasing band-bending giving a slope $\frac{d \log \omega_{max}}{d \Delta \phi_{sc}} = -1$. $\Delta \phi_{sc}$ is the potential drop in the semiconductor, i.e. the band-bending. A value of -2/3 is found.

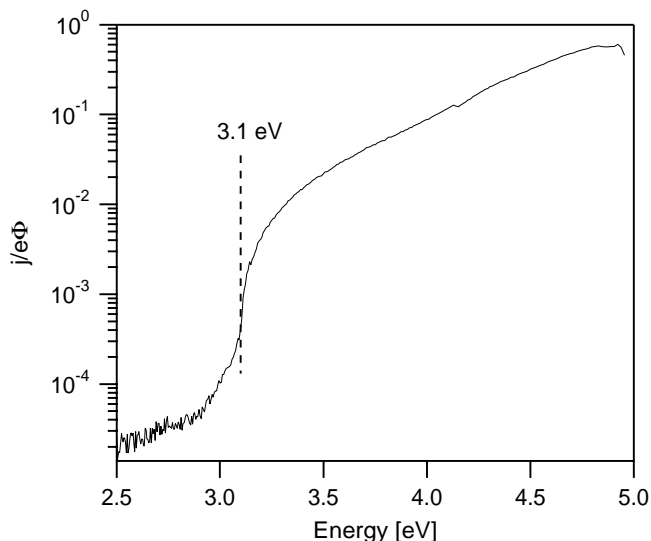


FIGURE 4.6. Photocurrent quantum yield as a function of photon energy. The electrolyte was a 1 M H_2SO_4 solution containing 5% ethanol. The potential was +1.5 V vs. SCE.

Very probably this is due to the fact that in the recombination range both $\Delta\phi_{sc}$ and $\Delta\phi_H$ change with the applied potential.

4.3.4 Photocurrent quantum yield

Fig. 4.6 shows a spectrum of the photocurrent quantum yield obtained in a solution containing ethanol as a stabilizer. The quantum yield was obtained by comparing the photocurrent to that measured with an n -type GaAs electrode, and correcting for reflection losses using literature data [45, 46]. The potential was chosen such that surface recombination was absent. Using these data, the complete Gärtner equation and the value for L_p obtained from the measurements shown in Fig. 4.4, we calculated the absorption coefficient α as a function of photon energy. The results are shown in Fig. 7 as $\alpha^{1/2}$ vs. $h\nu$, together with the absorption spectrum for this modification of SiC reported by Choyke [47], and Philipp [48]. The agreement is strikingly good.

The experimental plot clearly reproduces the most important features of the absorption spectrum. The positions of the fundamental absorption edges as

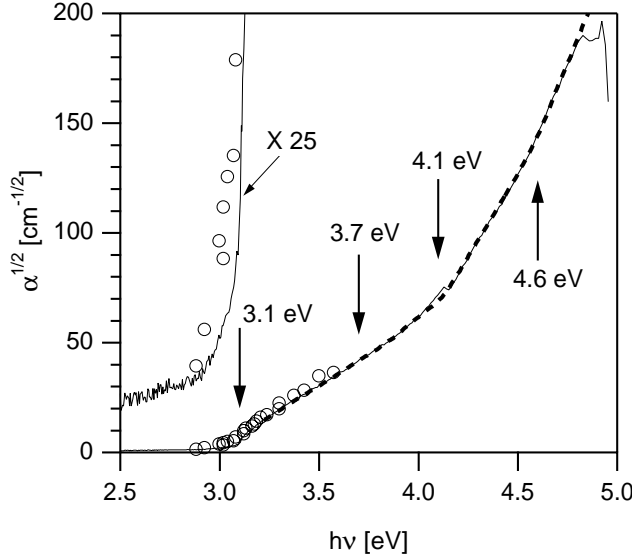


FIGURE 4.7. Calculated absorption coefficient vs. photon energy. The continuous line was obtained from the present measurements. The dashed line is taken from Ref. [47], the open circles are taken from Ref. [48]. The numbers indicate the positions of the fundamental absorption edges. An enlargement of the first indirect absorption region is also shown.

identified by Choyke et al. [47], are indicated by arrows. The figure also shows the bandgap region enlarged, together with data from the literature for this region [48]. Again, the agreement is very good. This supports the reliability of our estimates of the band-bending from the (C_p^{-2}, V) plots and of L_p from the Gärtner relationship.

As shown in Fig. 4.6 there is a substantial sub-bandgap photocurrent. The magnitude of this photocurrent shows an approximately exponential dependence on photon energy. Chazalviel et al. also observed an exponential dependence of the sub-bandgap quantum yield for Si [49]; this was explained with a wide distribution of surface states, from which thermal injection of charge carriers into one of the bands occurs. To investigate this intriguing phenomenon we measured the photocurrent using light from a He-Ne laser (632.8 nm \approx 1.96 eV). Fig. 4.8 shows the response to a square pulse of light shortly after immersion of the electrode in the electrolyte solution. The photocurrent response con-

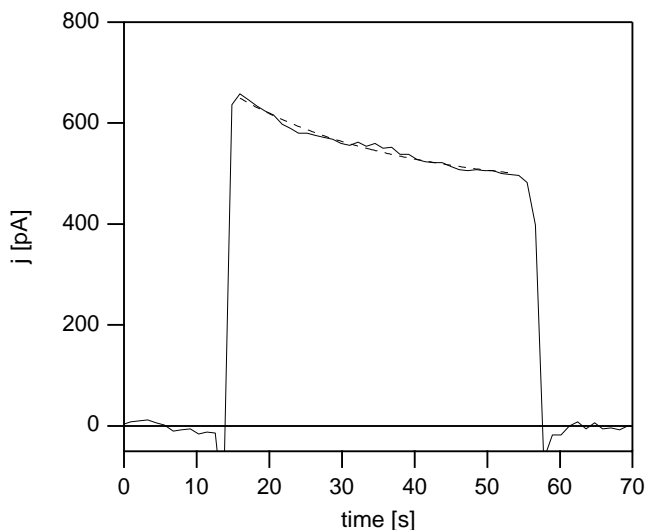


FIGURE 4.8. Photocurrent transient observed upon illumination of a 6H *n*-SiC electrode in 1M H₂SO₄ with light from a He-Ne laser ($h\nu = 1.96$ eV).

sists of two parts, one strongly time-dependent, the other time-independent (in the time frame of this measurement). Although the photocurrent is very small (10^{-10} A) it is striking that it is observed at all, considering the huge difference between the bandgap (3.1 eV) and the energy of the light (1.96 eV). The time-dependent part vanishes after several minutes of illumination, and returns only if the electrode is etched in HF solution to remove surface oxide. This part of the photocurrent is obviously due to surface processes.

The time-independent photocurrent proved to be strongly dependent on potential. Fig. 4.9 shows the sub-bandgap quantum yield as a function of the band bending (open circles) together with results obtained for bandgap light (354 nm). It is seen that extrapolation to the horizontal axis yields the same value for the minority carrier diffusion length (L_p) in both cases. This implies that the sub-bandgap photocurrent is due to a bulk (as opposed to a surface) process. From the plot in Fig. 4.9 the absorption coefficient is found to be 0.28 cm^{-1} . This value is probably a factor of 2 too high because of reflection at the back contact (the thickness of the samples is about 0.3 mm). This sub-bandgap effect is unlikely to be due to two-photon absorption because the quantum yield is not strongly dependent on the light intensity. The large difference (1 eV) between the excita-

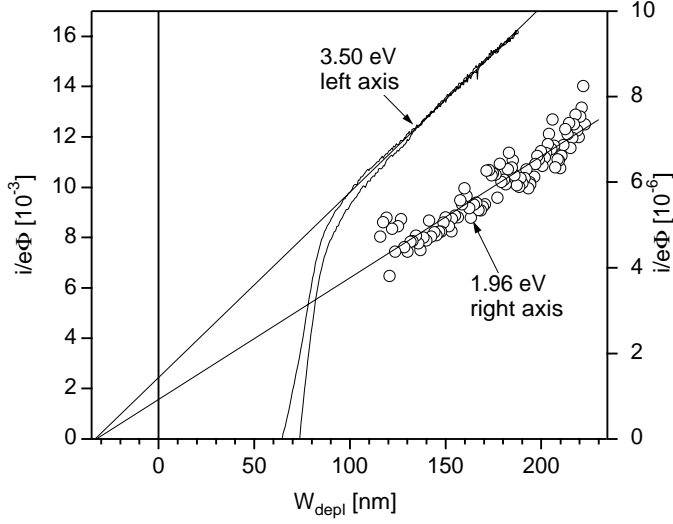


FIGURE 4.9. Dependence of the sub-bandgap photocurrent quantum yield on depletion layer width. The data from Fig. 4.4 are shown for comparison. As can be seen the x-axis intercept of a linear fit yields the same value for the hole diffusion length as obtained with bandgap light.

tion light energy and the bandgap means that escape of a localized carrier in the bandgap to the valence or conduction band by a thermally activated process is also highly unlikely. It is much more plausible that the sub-bandgap photocurrent is due to two consecutive optical transitions, one from a valence band state to a localized state in the bandgap, and a second from the localized state to a conduction band state. In this way consecutive absorption of two photons via an intermediate state leads to an electron in the conduction band, and a hole in the valence band.

4.4 Conclusions

(C_p^{-2}, V) plots of *n*-type 6H-SiC showed that the Mott-Schottky relationship is obeyed over a large potential range (>5 volts). Considerable deviation from linearity was observed close to the flat-band potential, indicating the presence of surface states.

The dependence of the flatband potential on solution pH is explained by the presence of a thin native oxide, and adsorption and desorption of protons and/or hydroxyl ions. The exact pH dependence points to the presence of a proton-exchange mechanism, in which amphoteric -OH groups play a role.

From the potential dependence of the photocurrent a hole diffusion length of 30 nm was found. The absorption spectrum obtained by measuring the photocurrent quantum yield as a function of photon energy agrees quantitatively with literature spectra. The results of IMPS show that, besides bulk recombination, recombination also occurs via surface states.

A sub-bandgap photocurrent was observed, even at a photon energy of 1 eV below the bandgap. This photocurrent consists of two parts. The time-dependent part is probably due to light absorption involving surface states, and vanishes after several minutes of illumination. The time-independent part is attributed to consecutive absorption of two photons, mediated by localized bandgap states in the bulk material.

References

- [1] G. L. Harris, *Properties of Silicon Carbide* (INSPEC EMIS Datareviews No13, Exeter, 1995).
- [2] T. Inoue, A. Fujishima, and S. Konishi, *Nature* **277**, 638 (1979).
- [3] I. Lauer mann, R. Memming, and D. Meissner, *J. Electrochem. Soc.* **144**, 73 (1997).
- [4] J. O. M. Bockris and K. Uosaki, *J. Electrochem. Soc.* **124**, 1348 (1977).
- [5] T. Inoue and T. Yamase, *Chem. Lett* 869 (1985).
- [6] J. S. Shor and A. D. Kurtz, *J. Electrochem. Soc.* **141**, 778 (1994).
- [7] J. S. Shor and R. M. Osgood, *J. Electrochem. Soc.* **140**, L133 (1993).
- [8] J. S. Shor, X. G. Zhang, and R. M. Osgood, *J. Electrochem. Soc.* **139**, 1213 (1992).
- [9] L. Zhou, V. Audurier, P. Pirouz, and J. A. Powell, *J. Electrochem. Soc.* **144**, L161 (1997).
- [10] M. Gleria and R. Memming, *J. Electroanal. Chem.* **65**, 163 (1975).
- [11] H. Morisaki, H. Ono, and K. Yazawa, *J. Electrochem. Soc.* **131**, 2081 (1984).
- [12] A. Manivannan, A. Fujishima, and G. V. Subba Rao, *Ber. Bunsenges. Phys. Chem.* **92**, 1522 (1988).
- [13] J. S. Shor, I. Grimberg, B.-Z. Weiss, and A. D. Kurtz, *Appl. Phys. Lett.* **62**, 2836 (1993).
- [14] T. Matsumoto, J. Takahashi, T. Tamaki, T. Futiga, and H. Mimura, *Appl. Phys. Lett.* **64**, 226 (1994).
- [15] A. O. Konstantinov, C. I. Harris, and E. Janzén, *Appl. Phys. Lett.* **65**, 2699 (1994).
- [16] A. Takazawa, T. Tamura, and M. Yamada, *Jpn. J. Appl. Phys.* **32**, 3148 (1993).
- [17] L.-S. Liao, X.-M. Bao, Z.-F. Yang, and N.-B. Min, *Appl. Phys. Lett.* **66**, 1382 (1995).

- [18] A. O. Konstantinov, A. Henry, C. I. Harris, and E. Janzén, *Appl. Phys. Lett.* **66**, 2250 (1995).
- [19] C. I. Harris, A. O. Konstantinov, C. Hallis, and E. Janzén, *Appl. Phys. Lett.* **66**, 1501 (1995).
- [20] J. van de Lagemaat, M. Plakman, D. Vanmaekelbergh, and J. J. Kelly, *Appl. Phys. Lett.* **69**, 2246 (1996).
- [21] E. A. Ponomarev and L. M. Peter, *J. Electroanal. Chem.* **396**, 219 (1995).
- [22] Cree, Research Inc. 2810 Meridian Parkway Suite 176 Durham NC 27713 USA .
- [23] F. Mansfeld, S. Lin, C. Chen, and H. Shih, *J. Electrochem. Soc.* **135**, 906 (1988).
- [24] S. R. Morrison, *Electrochemistry at semiconductor and oxidized metal electrodes* (Plenum, New York, 1980).
- [25] E. H. Nicollian and A. Goetzberger, *Bell. Syst. Tech. J.* **46**, 1055 (1967).
- [26] G. Oskam, D. Vanmaekelbergh, and J. J. Kelly, *Electrochim. Acta* **38**, 301 (1993).
- [27] M. J. Madou, B. H. Loo, K. W. Frese, and S. R. Morrison, *Surf. Sci.* **108**, 135 (1981).
- [28] D. E. Yates, S. Levine, and T. W. Healy, *J. Chem. Soc. Faraday. Trans. I* **70**, 1807 (1974).
- [29] L. Bousse, N. F. de Rooij, and P. Bergveld, *Surf. Sci.* **135**, 479 (1983).
- [30] L. Bousse, N. F. de Rooij, and P. Bergveld, *IEEE Trans. Electr. Dev.* **30**, 1263 (1983).
- [31] L. Bousse and P. Bergveld, *J. Electroanal. Chem.* **152**, 25 (1983).
- [32] M. J. Madou and S. R. Morrison, *Chemical Sensing with Solid State Devices* (Academic Press, Boston, 1989).
- [33] W. W. Gärtner, *Phys. Rev.* **116**, 84 (1959).
- [34] R. Peat and L. M. Peter, *Appl. Phys. Lett.* **51**, 328 (1987).
- [35] A. Etcheberry, M. Etman, B. Fotouhi, J. Gastron, J.-L. Sculfort, and P. Lemasson, *J. Appl. Phys.* **53**, 8867 (1982).
- [36] J. Li, R. Peat, and L. M. Peter, *J. Electroanal. Chem.* **165**, 41 (1984).
- [37] B. L. Wheeler, G. Nagasubramanian, and A. J. Bard, *J. Electrochem. Soc.* **131**, 1038 (1984).
- [38] J. P. Stagg, *J. Appl. Phys.* **53**, 3680 (1982).
- [39] V. S. Ballandovich and G. N. Violina, *Sov. Phys. Semicond.* **15**, 959 (1981).
- [40] A. R. de Wit, D. Vanmaekelbergh, and J. J. Kelly, *J. Electrochem. Soc.* **139**, 2508 (1992).
- [41] D. Vanmaekelbergh, A. R. de Wit, and F. Cardon, *J. Appl. Phys.* **73**, 5049 (1993).
- [42] J. Li and L. M. Peter, *J. Electroanal. Chem.* **193**, 27 (1985).
- [43] W. J. Albery, P. N. Bartlett, and C. P. Wilde, *J. Electroanal. Chem.* **134**, 2486 (1987).
- [44] G. H. Schoenmakers, D. Vanmaekelbergh, and J. J. Kelly, *J. Phys. Chem.* **100**, 3215 (1996).
- [45] B. E. Wheeler, *Sol.St.Comm.* **4**, 173 (1966).
- [46] D. E. Aspnes and A. A. Studna, *Phys. Rev. B* **27**, 985 (1983).
- [47] W. J. Choyke and L. Patrick, *Phys. Rev.* **172**, 769 (1968).
- [48] H. R. Philipp, *Phys. Rev.* **111**, 440 (1958).
- [49] J.-N. Chazalviel, M. Stefenel, and T. B. Truong, *Surf. Sci.* **134**, 865 (1983).

Chapter 5

Photoelectrochemistry of porous 6H-SiC

Abstract

SEM(Scanning Electron Microscopy) micrographs of *n*-type silicon carbide(SiC) anodized in HF solution showed a highly porous layer having structures with dimensions of about 50 nm. The capacitance of the porous electrodes revealed a huge surface area. The photocurrent quantum yield of a porous SiC/electrolyte diode is spectacularly enhanced with respect to that of a flat diode for light absorbed in the indirect bandgap and for sub-bandgap light.

5.1 Introduction

Silicon carbide (SiC) is currently receiving wide attention because its unique material and electrical properties [1–4] make it suitable for application in electronic devices operating at very high temperatures and high power levels. Recently Shor and co-workers [1] showed that, by anodization under UV illumination, 6H-SiC could be made porous with structural units in the 5–150 nm size range. The material properties are changed considerably by this treatment. Matsumoto and co-workers [2] observed an intense blue-green luminescence from porous SiC prepared in a similar way. Konstantinov and co-workers also prepared porous SiC by anodization in the dark [3, 4] and observed an enormous increase of the interfacial capacitance at small band bending, indicating a corresponding increase of the area of the semiconductor/electrolyte interface. Ern  et al. found the same effect with GaP made porous by anodization in sulphuric acid solution [5, 6]. Furthermore, a marked enhancement of the quantum yield was observed for light absorbed in the indirect transition.

In this chapter we present results of capacitance and photocurrent measurements with porous 6H-SiC electrodes formed by anodic etching in HF solution. As for GaP, the quantum yield for light absorbed in the indirect transition (>2.9 eV) increased greatly. The increase of the sub-bandgap photocurrent was even more spectacular.

5.2 Experimental

The samples studied in this work, *n*-type 6H-SiC single crystals doped with nitrogen at a concentration of about $5 \times 10^{18} \text{ cm}^{-3}$, were prepared by high temperature recrystallization. The (0001) face was exposed to the solution. For the electrochemical measurements a standard three electrode configuration was used with a saturated calomel electrode (SCE) as a reference and a large area platinum sheet as the counter electrode. Electrical impedance measurements were carried out using a set-up consisting of an EG&G Par 273A potentiostat and a Solartron SI1255 frequency response analyzer. The light source for the photocurrent measurements was either a Coherent Ar-ion laser (355 nm) line, or a 500W Xe lamp equipped with a SPEX 1680 double monochromator. The samples were made porous by anodization in the dark in an aqueous 1M HF solution at a current

density of about $20 \text{ mA} \times \text{cm}^{-2}$ (total passed charge $0.02 - 12 \text{ C} \times \text{cm}^{-2}$). The cell potentials under these conditions ranged from 4-5 V vs. SCE.

5.3 Results

Figure 5.1a shows a SEM micrograph of an untreated surface. Figure 5.1b shows a micrograph of an etched sample after about 12 C cm^{-2} has been passed. The difference is striking. While the unetched surface is flat, the etched surface is clearly porous, showing columnar structures with dimensions of the order of 50nm. The capacitance-potential ($C - V$) curves were measured in $1 \text{ M H}_2\text{SO}_4$ before and after anodization. In figure 5.2 results are shown for an etch charge of 2.2 C cm^{-2} . The $C_p^{-2} - V$ plot of a flat electrode complies with the Mott-Schottky relationship, showing a flat-band potential of -0.7 V vs SCE . At small band bending ($V < 0.5 \text{ V}$) the capacitance of the porous electrode is orders of magnitude larger than that of the flat electrode. At this band bending the inner edge of the depletion layer follows the contours of the porous structure. The capacitance, which is proportional to the area of the inner edge of the depletion layer, is hence very large. At sufficiently strong band bending the porous structure becomes completely depleted and, since the inner edge of the depletion layer is in the non-porous substrate, the measured capacitance tends to that of a flat electrode [3, 5, 6]. From the value of the band bending at which the capacitance of the porous electrode starts to deviate from that of the flat electrode, one can get an indication of the size of the porous structures. From the results in figure 5.2 we estimate a value of about 40 nm. This is in agreement with the value obtained from the SEM micrograph (figure 5.1b).

From figure 5.3 it is clear that the capacitance for a relatively small band bending ($V = -0.5 \text{ volt}$) increases considerably as a function of etch charge. Note that an etch charge of 1 C cm^{-2} and a porosity of 25% corresponds to a porous layer of about $1 \mu\text{m}$ in thickness. This shows that by anodic etching μm -thick porous layers can be formed.

The photocurrent of $n\text{-SiC}$ electrodes was measured in aqueous ferrous sulfate solutions ($\text{pH} = 0$). The Fe^{2+} -ions act as scavenger for the photogenerated holes and hence prevent photoanodic oxidation and passivation. The photocurrent-potential curve of a flat electrode illuminated with 355 nm light shows poor photodiode characteristics. The quantum yield is extremely low (10^{-3}) due to bulk and surface recombination. With a porous SiC electrode the

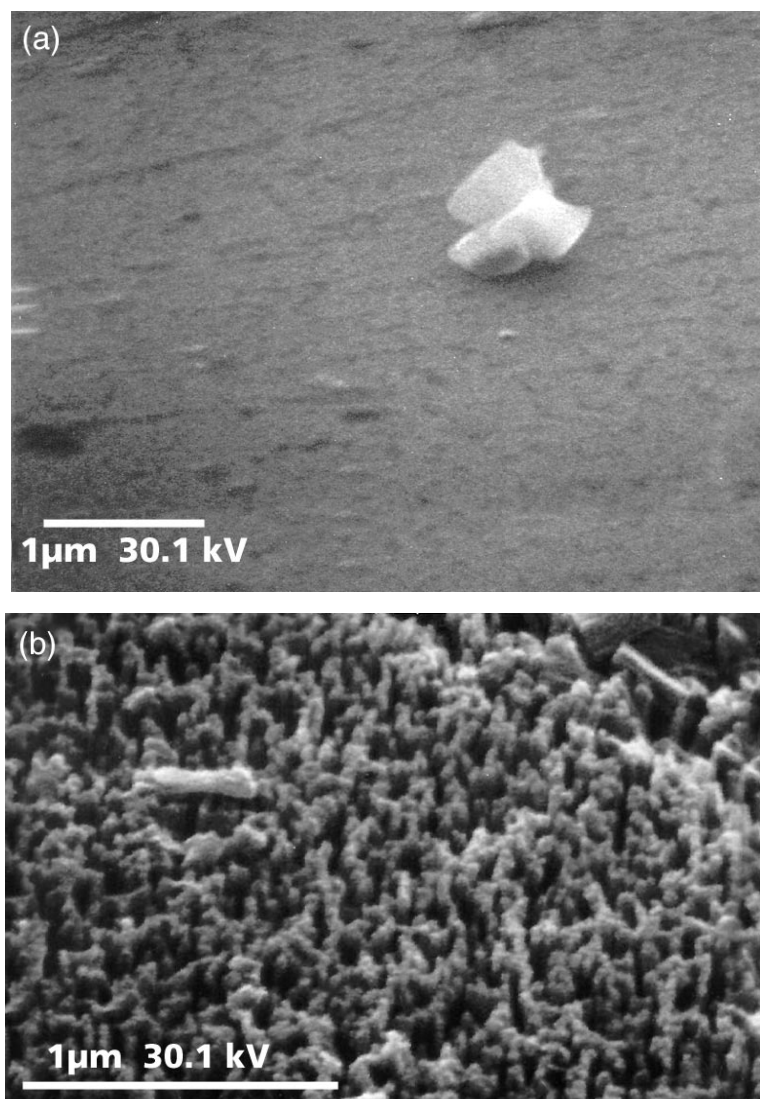


FIGURE 5.1. SEM micrographs of an *n*-SiC sample. (a) Unetched surface (protected by a Teflon-sticker). The white object is a dust particle that was used to focus the electron microscope. (b) After passing 12 C cm^{-2} in HF solution. In both micrographs the white bar corresponds to $1\mu\text{m}$.

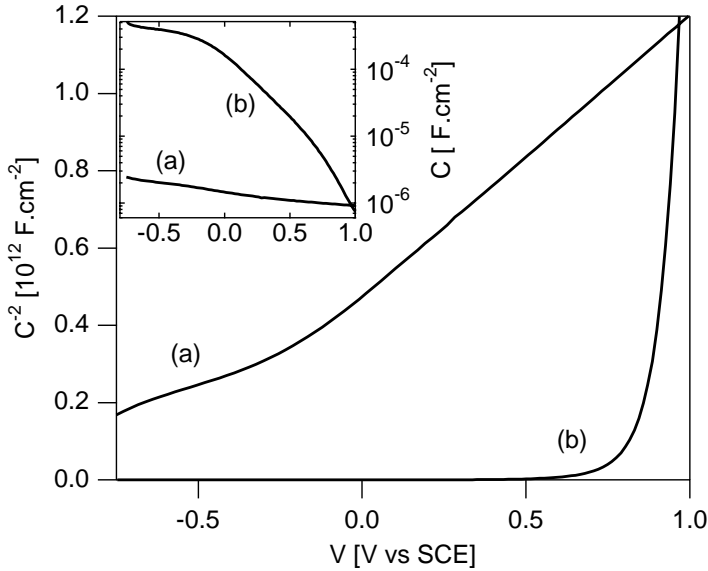


FIGURE 5.2. Mott-Schottky plots of n -SiC in 1M H_2SO_4 solution measured at 1kHz, for a) unetched electrode, b) a porous electrode anodized in HF to a charge of 2.2 C cm^{-2} . The inset shows the same data with the capacitance plotted on a log scale.

photocurrent is substantially larger in the entire potential range. The quantum yield was determined by comparing the photocurrent of the SiC electrode (j_{SiC}) with the limiting photocurrent of an n -GaAs electrode (j_{GaAs}), measured under the same conditions. The results were corrected for differences in reflection, using the data in [7, 8]. As GaAs is a direct semiconductor, its quantum yield is expected to be one in the measured energy range. Fig.5.4 shows that the quantum yield ($j_{\text{SiC}}/j_{\text{GaAs}}$) increases very strongly with increasing thickness of the porous layer. For example, an etch charge of 12 C cm^{-2} gives an enhancement of two orders of magnitude.

Figure 5.5 shows $j_{\text{SiC}}/j_{\text{GaAs}}$ as a function of the energy of the incident photons for a flat SiC photoanode and for two porous photoanodes. The quantum efficiency of the flat electrode is very low for the indirect transition ($2.9 \rightarrow 4.4 \text{ eV}$). The increase at higher energy can be attributed to a second (in)direct transition [9]. The porous photoanodes show a much larger quantum yield in the entire

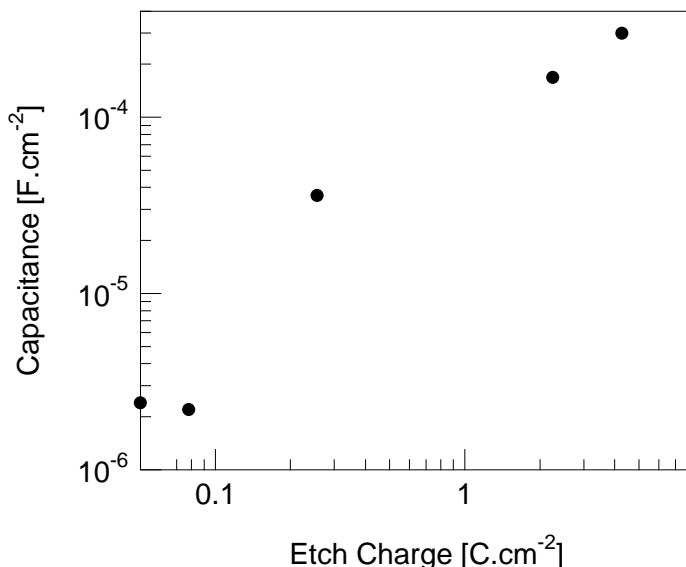


FIGURE 5.3. Interfacial capacitance of *n*-SiC plotted as a function of etching charge in 1M HF solution. The capacitance was measured in a 0.5 M H₂SO₄ solution at -0.5 V(SCE)

supra-bandgap region. An even more striking effect is found for sub-bandgap light.

5.4 Discussion

For a photodiode, minority carriers generated within a distance from the surface equal to sum of the width of the depletion layer and the diffusion length, escape recombination and can reach the electrolyte contact. For an unetched SiC photoanode the penetration depth of light absorbed in the indirect transition is much larger than this retrieval length. At 355 nm this depth is $1/(1200 \text{ cm}^{-1} [10]) \approx 8 \mu\text{m}$, while the width of the depletion layer is typically 20 nm. Consequently most electron-hole pairs recombine in the bulk and the photocurrent quantum yield is very low. At 355 nm the quantum yield would be 2×10^{-3} . The measured value of about 4×10^{-3} agrees rather well with this prediction.

The size of the structures of the porous SiC electrodes is about 40 nm. The quantum yield was measured at a band bending of 1.2eV ($V=+0.5 \text{ V}$) for which

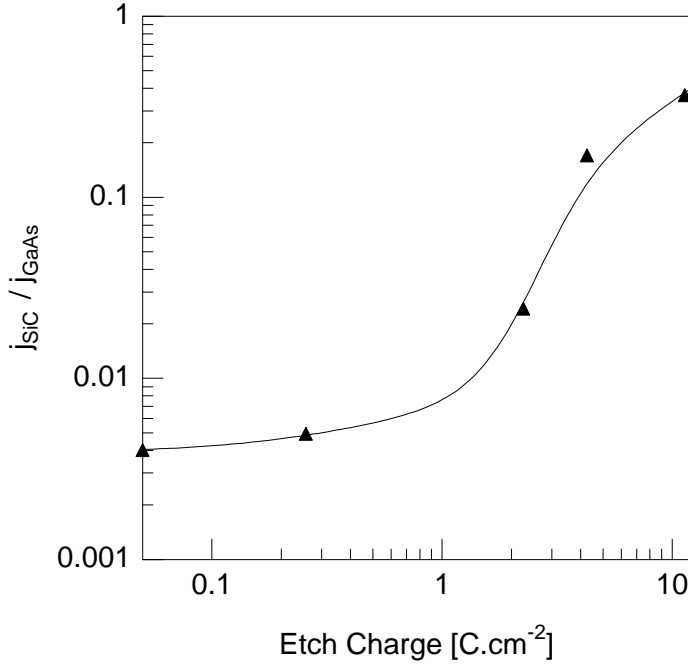


FIGURE 5.4. Photocurrent quantum yield of n -SiC measured at 355 nm (≈ 3.51 eV) in a 100 mM $Fe(SO_4)$, 0.5 M H_2SO_4 -solution, plotted as a function of etching charge. For the definition of j_{SiC} / j_{GaAs} see the text.

the minimum value for the retrieval length (equal to the width of the depletion layer) is 20 nm. As a consequence, holes, photogenerated in the porous structure, are always within the retrieval length from the surface and hence escape bulk recombination. Due to light scattering within the porous structure the photons are more effectively absorbed than in a flat electrode. In this way one can understand why the quantum yield has increased considerably on etching a porous layer of about $2\mu m$ ($2.2 C cm^{-2}$) in thickness, while $1/\alpha$ is typically $8\mu m$. On further etching, the quantum yield increases even further with increasing thickness of the porous layer and eventually reaches a value close to one (see figure 5.5, $12 C cm^{-2}$). A similar reasoning has been used to explain the increase of the quantum efficiency for light absorbed in the indirect transition of GaP photoanodes [5, 6].

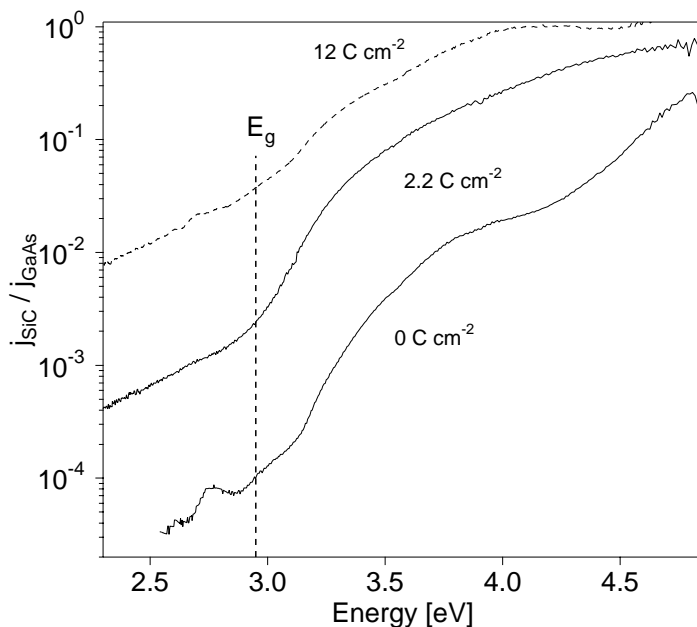


FIGURE 5.5. Photocurrent quantum yield of n -SiC vs. photon energy. The measurements were done in a 100 mM $\text{Fe}(\text{SO}_4)$, 0.5 M H_2SO_4 solution at 0.5 V(SCE). Data is shown for an unetched electrode, and two porous electrodes (2.2 and 12 C cm^{-2}).

The striking increase of the quantum yield for sub-bandgap photocurrent needs further explanation. In principle, sub-bandgap photocurrent can arise from the presence of bandgap states either in the bulk or at the surface. When an electron is excited from a sub-bandgap bulk state, a localized hole is formed. For photocurrent to flow, this hole must be thermally released to the valence band before recombination. When an electron is excited at the surface, a hole is localized in a surface state which may be directly involved in charge transfer. In a porous electrode, sub-bandgap light can be more effectively absorbed due to scattering and due to the greatly increased volume density of surface states. A more detailed description of the enhanced photocurrent response of porous photoanodes has been given by Iranzo-Marín *et al* [11].

5.5 Conclusions

Like previous work by Ern  et al. [5, 6], this work shows that bulk recombination, responsible for significant losses in photodiodes of indirect semiconductors, can be avoided by making the semiconductor porous. In this way interpenetrating semiconductor/liquid or semiconductor/metal networks may form a basis for development of solar cells based on low quality or indirect semiconductors.

References

- [1] J. S. Shor, I. Grimberg, B.-Z. Weiss, and A. D. Kurtz, *Appl. Phys. Lett.* **62**, 2836 (1993).
- [2] T. Matsumoto, J. Takahashi, T. Tamaki, T. Futiga, and H. Mimura, *Appl. Phys. Lett.* **64**, 226 (1994).
- [3] A. O. Konstantinov, C. I. Harris, and E. Janz n, *Appl. Phys. Lett.* **65**, 2699 (1994).
- [4] A. O. Konstantinov, A. Henry, C. I. Harris, and E. Janz n, *Appl. Phys. Lett.* **66**, 2250 (1995).
- [5] B. H. Ern , D. Vanmaekelbergh, and J. J. Kelly, *Adv. Mater.* **7**, 739 (1995).
- [6] B. H. Ern , D. Vanmaekelbergh, and J. J. Kelly, *J. Electrochem. Soc.* **143**, 305 (1996).
- [7] B. E. Wheeler, *Sol.St.Comm.* **4**, 173 (1966).
- [8] D. E. Aspnes and A. A. Studna, *Phys. Rev. B* **27**, 985 (1983).
- [9] W. J. Choyke and L. Patrick, *Phys. Rev.* **172**, 769 (1968).
- [10] H. R. Philipp, *Phys. Rev.* **111**, 440 (1958).
- [11] F. Iranzo-Mar n, M. A. Hamstra, and D. Vanmaekelbergh, *J. Electrochem. Soc.* **143**, 1137 (1996).

Chapter 6

Excitonic effects in the photoluminescence of GaN studied at the semiconductor/electrolyte interface

Abstract

Results of *in-situ* photoluminescence experiments on the GaN/electrolyte interface are reported. In particular, the dependence of the photoluminescence yield on the photon energy of the exciting light was studied. In these spectra, clear evidence for excitonic absorption was observed. Variation of the electrode potential proved to be a useful tool in distinguishing between free electron-hole pair generation and exciton creation. The spectra showed the presence of the three known excitons in GaN. The exciton binding energy was determined to be 27 ± 1 meV.

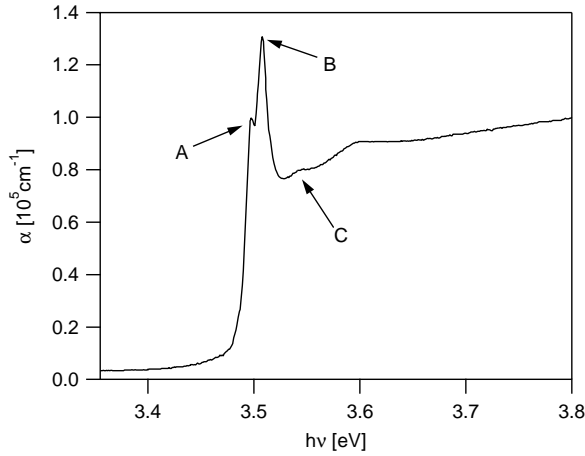


FIGURE 6.1. Low temperature (10K) absorption spectrum of a $0.38\ \mu\text{m}$ thick GaN sample. The positions of the A, B, and C excitons are indicated by arrows. The data was taken from [9].

6.1 Introduction

The wurtzite polytypes of InN, GaN, and AlN with direct bandgaps of 1.9 eV, 3.4 eV and 6.2 eV, respectively, are of considerable interest for opto-electronic applications at wavelengths ranging from the red well into the UV. Devices made of GaN are expected to be radiation hard, chemically and physically stable, and suitable for high power operation [1].

Light emitting GaN diodes were demonstrated already in 1970 [2, 3]. Recently, a “stable” UV laser diode based on GaN that operated for up to 6 hours at room temperature at 17 mW has been reported [4]. GaN based laser diodes emitting in the visible region of the spectrum have also been fabricated [3]. Blue and UV lasers are important for the next generation of information storage media.

From a fundamental point of view GaN is particularly interesting. Because of their large binding energy ($> 20\ \text{meV}$) [5]), it should be possible to observe excitons directly at room temperature. While exciton emission has been reported for photoluminescence experiments [6, 7] (see below), an exciton contribution in absorption [6, 7] and photoconductivity [8] is only indicated by a weak peak in the onset of the spectrum.

Because of the three valence bands in wurtzite semiconductors, three exciton lines are generally observed. Figure 6.1 shows a low temperature absorption spectrum (10K) taken from Ref. [9]. The region around 3.5 eV is dominated by sharp excitonic resonances. Above 3.7 eV the spectrum reflects the direct band-band transition. The shoulder in the spectrum at 3.6 eV can be attributed to indirect exciton-phonon absorption [9]. When the temperature is raised, the excitonic peaks broaden and merge. At room temperature, they can still be observed, but their exact energetic positions can only be obtained by fitting procedures.

In this chapter, it will be shown that excitonic effects play an important role in the photoelectrochemistry of GaN. We describe how excitons in GaN can be studied by making use of the properties of the semiconductor/electrolyte interface. The possibility of manipulating the depletion layer inside the semiconductor by means of the electrode potential proves to be a valuable tool to distinguish between excitonic and band-band absorption processes. The results are presented in two parts. First, photoluminescence (PL) and photoelectrochemical experiments are described with a view to characterizing our GaN samples (section 6.3) and establishing the potential distribution at the semiconductor/electrolyte interface (section 6.4). These results form the basis for the study of excitonic processes as observed in the photoluminescence excitation experiments (section 6.5). Surprisingly, the focus of attention in *in-situ* luminescence measurements in photoelectrochemistry has been on emission characteristics; little or no work has been done on excitation spectroscopy.

Not much is known about the (photo)electrochemistry of GaN. Kocha *et al.* [10] showed the pH dependence of the flat band potential to be close to Nernstian (60mV/pH), indicating the presence of an oxide layer at the surface. Furthermore, the photocurrent spectrum was measured. A few authors have investigated the possibility of photoetching GaN with UV light [11–14]. In general, highly anisotropic etching with μm sized features can be obtained with the photoanodic method. In an appendix to this chapter we describe for the first time porous GaN obtained by photoetching.

6.2 Experimental

The epitaxial layers were grown at the Fraunhofer Institut für Angewandte Festkörperphysik by MOCVD on sapphire ($\alpha\text{-Al}_2\text{O}_3$) substrates using a 30 nm AlN buffer layer to reduce stress in the GaN [15]. The as grown layers were *n*-

type. The layers were co-doped with Si, that acts both as a donor (when it is on a Ga-site) [16] and a deep acceptor (on a N-site) [1]. The density of uncompensated donors is $6 \times 10^{17} \text{ cm}^{-3}$. The surfaces are (0001) oriented and are Ga-terminated [15]. Ohmic contacts were made by microwave sputtering of Ti/Al/Ni/Au (15/300/40/200 nm), on the upper surface of the samples, which were then glued on copper rods. A thin copper wire and silver paste was used to connect the Ohmic contacts to the copper rod. This assembly was mounted in a PVC holder. The contacts and the copper were protected from the electrolyte solution by Apiezon resin, leaving about 5 mm^2 GaN exposed. This assembly was mounted as a working electrode in an electrochemical cell with a Saturated Calomel Electrode (SCE) as reference. The SCE was connected parallel to a platinum wire through a 20pF capacitance to minimise high frequency phase shift errors [17]. Potentials are given with respect to SCE. A large area platinum sheet served as a counter electrode. The cell was controlled by means of an EG&G PAR273A or a PAR283 potentiostat. The electrical impedance measurements were performed with a Solartron SI1255 FRA in conjunction with the previous set-up.

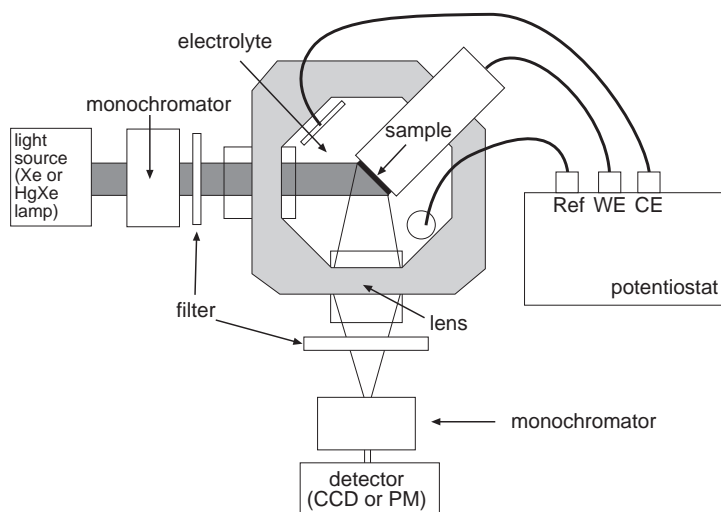


FIGURE 6.2. Schematic overview of the set-up used in the *in-situ* photoluminescence experiments

A schematic overview of the set-up used for the *in situ* luminescence experiments is given in figure 6.2. The electrochemical cell, made from perspex, was fitted with entry holes for the sample and the other electrodes. Light enters through a quartz window and illuminates the sample. Light emitted by the sample is collected by a quartz lens, and focussed on the detection system. The excitation source was a 500 W Xe or 150 W HgXe lamp in conjunction with a Spex 1680 0.22m double monochromator (resolution < 0.1 nm) or an Oriel 77250 1/8m single monochromator (resolution ≈ 1 nm). The detection system was either a Spex 1680 0.22m double monochromator with a Hamamatsu R928 PM-tube (resolution < 0.1 nm) or an Oriel Instaspec IV CCD camera with a 1/8m spectrograph (model 77400) (resolution ≈ 0.5 nm). Cut-off and bandpass filters were used to minimise second-order effects in the detection system. All spectra are corrected for lamp output and detector efficiency.

The solutions were prepared from analytical grade reagents and doubly distilled water. The surface of the electrode was cleaned by dipping in HCl before each measurement.

6.3 Photoluminescence characterization of the GaN samples

The materials were characterized using photoluminescence spectroscopy, current-voltage measurements in aqueous solutions, capacitance-voltage measurements, and photocurrent measurements. Fig. 6.3 shows a typical room temperature photoluminescence spectrum of an epitaxial layer of GaN. A small peak is observed at 3.4 eV due to recombination of (donor-bound) excitons [18] or a band-band transition [7]; we refer to this as the near band edge transition. The origin of the small peak at 3.2 eV is unclear. The strong band at 2.2 eV is commonly referred to as the yellow luminescence [7, 19]. The origin of this transition is still the subject of speculation [20–24]. Most likely it is due to defects caused by the Si-dopant, for example by Ga-vacancies [25]. The intensity of this line is strong indicating that our material is defect-rich. We make extensive use of the high intensity of the yellow luminescence as a probe for absorption processes later in this chapter.

Fig. 6.4 shows photoluminescence spectra for different temperatures. At 4.3 K the spectrum is dominated by a donor-acceptor transition at 3.255 eV with clear phonon-replicas. At higher temperatures the peak series disappears. Four

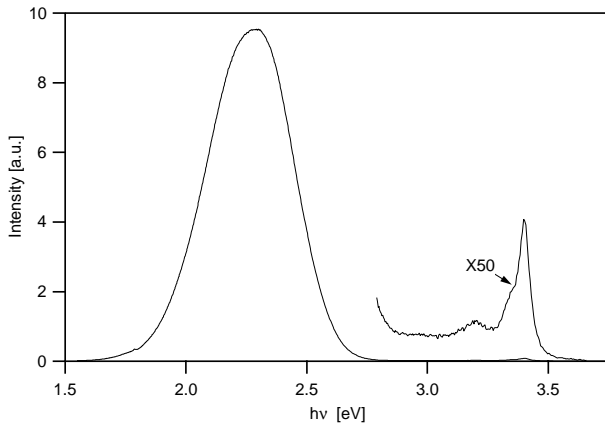


FIGURE 6.3. Room temperature photoluminescence of the epitaxial layers used in this study. Excitation was performed at 4 eV. The luminescence peak at 3.4 eV is caused by exciton or band-band recombination. The large peak observed at 2.2 eV is defect luminescence, probably caused by the Si-dopant

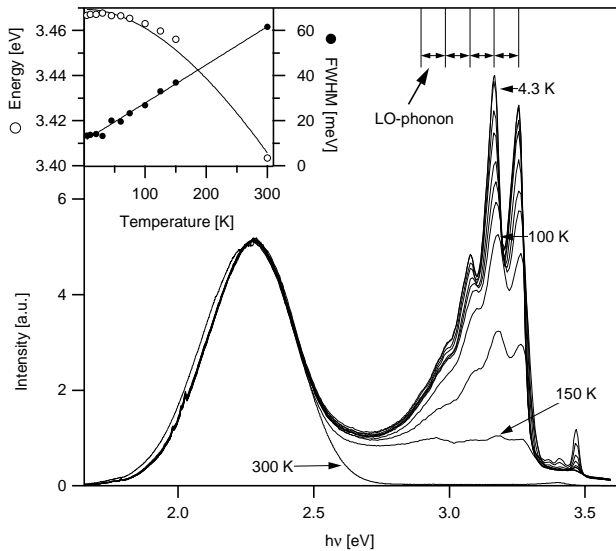


FIGURE 6.4. Temperature dependence of the photoluminescence of an epitaxial layer of GaN. Excitation was performed at 4 eV. The spectra have been normalised with respect to the intensity of the yellow luminescence line. The inset shows the position of the exciton-recombination peak, and its full-width at half maximum (FWHM) as a function of temperature. The peak series observed at and below 3.3 eV is caused by donor-acceptor pair recombination. The separation of the peaks is given by the LO phonon energy of the material [26].

phonon replicas are distinguishable. The spacing between the replicas yields the LO (longitudinal optical) phonon energy of the host lattice [26]. We find an LO phonon energy of 90 meV ($=725 \text{ cm}^{-1}$). This is in excellent agreement with the literature value of 726 cm^{-1} [1, 27–29]. It is probable that the donor is the native defect level, and that the acceptor is supplied by the Si impurity. The native defect level has an energy of 30 meV below E_C , and the Si acceptor of 225 meV above E_V [1]. Subtracting these values from the bandgap at 4 K (3.50 eV [1]) gives an expected energy of the transition of 3.245 eV. The zero phonon peak is observed at 3.255 eV. The difference between these two values is small enough to suggest that the active pair is formed by Si and the native defect level.

The yellow luminescence does not appear to be dependent on temperature. The position of the near band-edge transition is temperature dependent. The inset in figure 6.4 shows the temperature dependence of its position and full-width at half maximum (FWHM) as obtained from fitting near band-edge spectra with a combination of 3 Voigt-profiles. As for most semiconductors, the position can be described by the phenomenological Varshni equation for the temperature dependence of the bandgap of most semiconductors [1, 9, 26, 30]: $E_g(T) = E_g(T = 0) - \frac{\alpha T^2}{\beta + T}$.

6.4 Photoelectrochemical characterization of the GaN/electrolyte interface

Figure 6.5 shows the parallel capacitance plotted as C_p^{-2} vs V for an epitaxial layer of n-type GaN in a 0.5 M H_2SO_4 solution. In a large potential range, the capacitance obeys the linear Mott-Schottky relationship, proving that a majority carrier depletion layer is formed. The doping density obtained from the slope of the plot at 316.2 Hz $= 6 \times 10^{17} \text{ cm}^{-3}$. This value corresponds to that determined by the growers. The flat band potential (V_{fb}) is estimated at $-0.8 \pm 0.05 \text{ V}$ vs SCE. This is in good agreement with the results of Kocha *et al.* [10]. The insert of Fig. 6.5 shows the dark current measured under the same conditions plotted on a log scale as a function of potential. As expected, diode characteristics are observed with low reverse currents ($\approx 100 \text{ nA.cm}^{-2}$).

Figure 6.6 shows the photocurrent density of the GaN electrode in 0.5 M H_2SO_4 solution as a function of applied potential. The photon energy used for this experiment (4 eV) is well above the bandgap and thus generates free charge carriers. Photocurrent is observed if the electrons and holes are effectively sep-

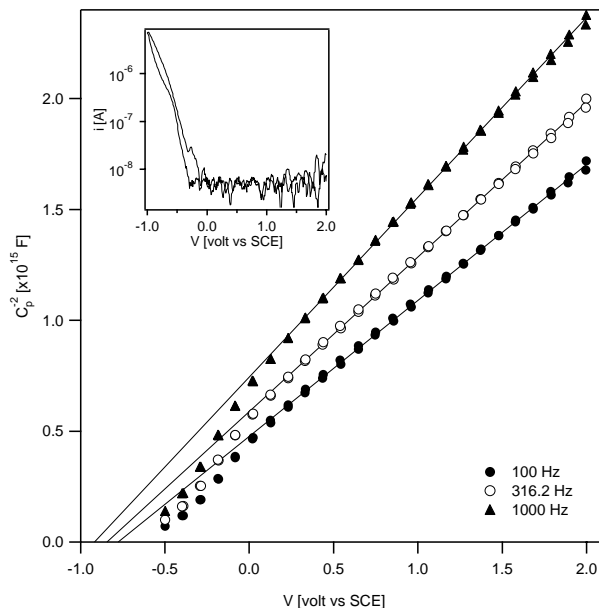


FIGURE 6.5. C_p^{-2} vs. V plot of an epitaxial layer of GaN in 0.5 M H_2SO_4 (pH=0). The insert shows the current voltage plot as $|i|$ vs electrode potential.

arated and the minority carriers (holes in this case) are transferred across the semiconductor/electrolyte interface. The onset of photocurrent at -0.5 V is followed by a sharp increase and a levelling-off above +0.5 V. Since no etching of the semiconductor was observed and we have no evidence for significant oxide formation, the reaction must be the oxidation of water ($2 \text{H}_2\text{O} + 4h^+ \rightarrow \text{O}_2 + 4\text{H}^+$).

The potential dependence of the the photocurrent can be described by the simple Gärtner model (see also section 1.2.3, page 20), which considers generation, migration and diffusion of charge carriers. The generation rate at a depth x is given by $-d\phi/dx$ where $\phi(x) = \phi(0) \exp(-\alpha x)$ (The Lambert-Beer law); $\phi(0)$ is the photon flux at the surface ($x = 0$), $\phi(x)$ is the flux at depth x and α is the absorption coefficient. The penetration depth of the light is given by $1/\alpha$. Two processes contribute to charge separation. Electron-hole pairs, created within the depletion layer, are separated by the strong electric field. The minority carriers migrate to the surface, the majority carriers to the bulk; this occurs extremely fast on a ps time scale [31, 32]. It is clear that the width of the space charge layer

W_{depl} will be important. The width is determined by the band bending $V - V_{fb}$ (V is the applied potential):

$$W = \left(\frac{2\epsilon\epsilon_0(V - V_{fb})}{eN_D} \right)^{1/2} \quad (6.1)$$

where ϵ is the dielectric constant of the solid, and N_D the donor density. Because of the effective charge separation within the depletion layer, the concentration of minority carriers at the bulk edge of this layer is low. Minority carriers generated within a diffusion length L_p of the edge can reach the depletion layer by diffusion and so contribute to the current. L_p is related to the minority carrier lifetime τ by $L_p = \sqrt{D_p\tau}$. D_p is the diffusion constant of the minority carriers given by the Einstein equation: $D_p = \mu_p \frac{k_B T}{e}$, in which μ_p is their mobility. The distance $W = W_{depl} + L_p$ is therefore the width of the layer within which charge separation occurs. Electrons and holes due to photons absorbed deeper in the solid recombine and do not contribute to the photocurrent. The quantum yield defined as the number of charge carriers passed in the external circuit for each photon absorbed is determined by the flux of minority carriers arriving at the surface and by losses due to surface recombination. For the Gärtner model in which surface recombination is disregarded the quantum yield is given by [33]:

$$\frac{j}{e\phi(0)} = 1 - \frac{\exp(-\alpha W_{depl})}{1 + \alpha L_p} \quad (6.2)$$

where j is the photocurrent and e the elementary charge. A plot of $-\ln(1 - j/e\phi(0))$ versus W_{depl} should give a straight line with a slope α and an intercept $\ln(1 + \alpha L_p)$. The insert in Fig. 6.6 shows such a plot. A straight line is observed for $W_{depl} > 50$ nm. The y -axis intercept yields a hole diffusion length of ≈ 10 nm. From the slope, a value for α of $1.6 \cdot 10^5 \text{ cm}^{-1}$ is obtained, in fair agreement with the literature data for this energy: $1.4 \cdot 10^5 \text{ cm}^{-1}$ [5]. When $W_{depl} < 50$ nm, less photocurrent is observed than expected from equation 6.2. This is an indication for surface recombination which only occurs at low band bending, when the concentration of conduction band electrons at the surface is high.

Figure 6.7 shows the photocurrent as a function of photon energy for an n -GaN photoanode in 0.5 M H_2SO_4 solution at three different electrode potentials. At more negative potentials and photon energies below the bandgap, the photocurrent is low. At around the bandgap the photocurrent increases sharply, saturating at 3.45 eV. As expected, the photocurrent is strongly dependent on elec-

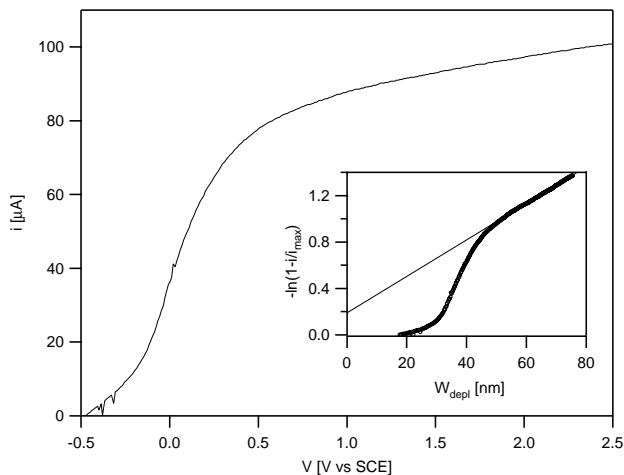


FIGURE 6.6. Photocurrent vs voltage measured on an epitaxial layer of GaN in 0.5 M H_2SO_4 (pH=0). Light with photons of 4.0 eV was used. The insert shows the same data plotted as $-\ln[1 - j/j_{\max}]$ vs depletion layer width (W_{depl}) as calculated from equation 6.1.

trode potential. However, in the sub gap range (< 3.4 eV) a strong increase of the photocurrent is observed for the more positive electrode potentials. The sub gap photocurrent can be due to several processes, including tail state absorption, or absorption by the donor-acceptor pairs (see Fig. 6.4). The results presented in section 6.5 of this chapter, do suggest however that it may be due in part to more effective exciton breakup at higher potentials.

The photoluminescence intensity I_{PL} measured at 2.2 eV (the yellow luminescence) is shown as a function of potential in Fig. 6.8 for an excitation energy of 4 eV. In contrast to the photocurrent the intensity is low at positive potentials and increases to a limiting value at negative potentials. The potential dependence follows directly from the Gärtner model. Electron-hole pairs which are not effectively separated recombine and can give rise to light emission. From Eq. 6.2 it follows that:

$$I_{PL} = \frac{\kappa\phi(0)}{1 + \alpha L_p} \exp(-\alpha W_{\text{depl}}) \quad (6.3)$$

where κ is the ratio of radiative and non-radiative recombination. I_{PL} gives a maximum $I_{PL,\max}$ for $W_{\text{depl}} = 0$ so that $I_{PL}/I_{PL,\max} = \exp(-\alpha W_{\text{depl}})$. The insert

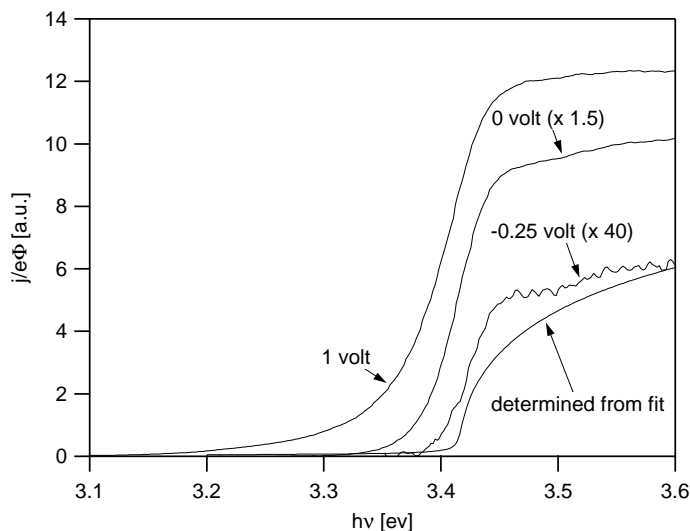


FIGURE 6.7. Photocurrent through the n-GaN/electrolyte interface as a function of photon energy. Electrolyte: 0.5 M H_2SO_4 . The photocurrent at -0.25 and 0 V is not drawn. The smooth line is the response calculated from fits such as that shown in figure 6.10.

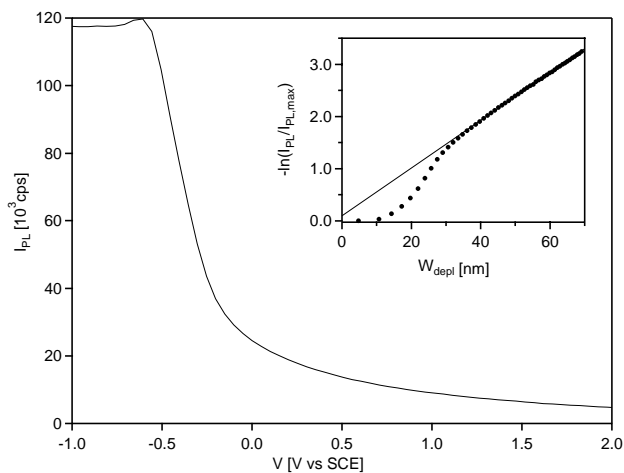


FIGURE 6.8. Intensity of the yellow luminescence as a function of electrode potential. Excitation at 4.0 eV. The insert shows the same data as $-\ln(I_{PL}/I_{PL,max})$ vs W_{depl} as calculated from equation 6.1.

of figure 6.8 shows that a plot of $-\ln(I_{PL}/I_{PL,max})$ vs. W_{depl} is linear for $W_{depl} > 35$ nm (compare with the insert in Fig. 6.6). The slope of the linear part yields a value of $4.5 \cdot 10^5 \text{ cm}^{-1}$ for α . This value is slightly larger than that determined from the photocurrent-potential relationship. It is however of the correct order of magnitude, and probably within the experimental error from the previously mentioned value. As expected from equation 6.3, the axis intercept of the linear part is almost zero.

6.5 Excitonic effects in the luminescence of GaN electrodes

In the previous section it was shown that the photocurrent and photoluminescence emission due to supra bandgap light can be well described by the dead layer model (equations 6.2 and 6.3). In this section, the dependence of the photoluminescence intensity at 2.2 eV (the yellow luminescence) on the photon energy of the exciting light (excitation spectrum) and the band bending will be discussed.

Excitation spectra of the yellow luminescence are given in Fig. 6.9 for various values of the applied potential. All spectra show an onset at about 3.35 eV, followed by a maximum at about 3.44 eV and a strong decrease at higher photon energy. The spectra depend only slightly on potential in the range -1.0 to -0.5 volt (i.e. close to the flat band value at -0.8 V). At more positive potentials corresponding to depletion a marked decrease in emitted intensity is observed. In addition, at large band bending a sharp peak develops in the spectra in the onset range at around 3.42 eV.

Photons with an energy larger than the bandgap (≈ 3.41 eV) generate free electrons and holes. Yellow luminescence is due to recombination via defect centres as is clear from the discussion in section 6.3. Two variables are important for determining the shape of the excitation spectra in this range: the penetration depth of the light (which depends on the photon energy) and the thickness of the charge separation layer (which depends on the applied potential). At negative potentials the semiconductor is close to the flat band condition. Since there is no depletion layer present in the semiconductor, migration of charge carriers is not important. Minority carriers generated within a diffusion length of the electrolyte interface can undergo non-radiative surface recombination. Electrons and holes generated beyond this region, whose dimension is independent of potential, will give rise to luminescence. Since the penetration depth of light

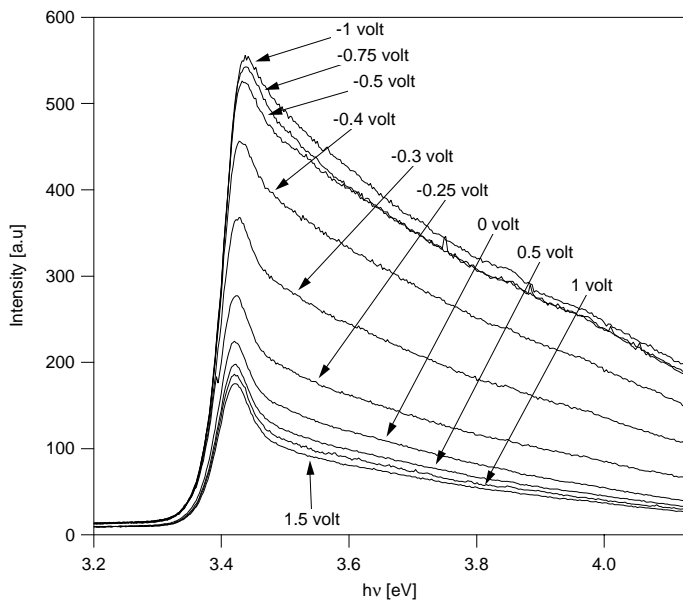


FIGURE 6.9. Photoluminescence excitation spectra as a function of applied potential. The emission was monitored at 2.2 eV.

decreases with increasing photon energy, the emission also decreases markedly. At more positive potentials the electric field of the depletion layer plays an important role in separating the electrons and holes, thus giving rise to photocurrent and reducing the emission intensity (the Gärtner model). For fixed α the emission intensity depends on potential via the depletion layer width (see also Fig. 6.8). For a fixed potential, the emission decreases with increasing photon energy, as described above.

The excitation spectrum of our GaN in air resembles closely that measured in electrolyte solution at negative potentials suggesting that in this case little or no electric field is present at the surface under illumination.

Exciton absorption is expected to be important in the onset of the excitation spectrum. Our results suggest that the peak in the spectrum, most pronounced at positive potentials, is due to excitonic processes. This implies that excitons can decay directly at defect sites giving yellow luminescence. The result indicates that while recombination of free charge carriers can be effectively suppressed by the electric field of the depletion layer, radiative recombination due to exciton

relaxation is less sensitive to the electric field present in the depletion layer. Relaxation of the exciton at defect centres must compete effectively with ionization followed by fast separation of the electron-hole pair. The fact that excitons must first be ionized before electron-hole pair separation takes place is an important difference with electron-hole pairs generated by band-band absorption. It is interesting to note that Liu *et al* [34] report a pronounced peak in the photovoltage spectrum of a GaN solid state device. They also attribute the peak to excitonic absorption.

To model the system the response generated by band-band absorption is first calculated. Equation 6.4 gives the absorption coefficient due to a direct transition [26, 34] ($i = \sqrt{-1}$).

$$\alpha_{dir} \propto \text{Real}((E - E_g + i\Gamma_{gap})^{1/2}) \quad (6.4)$$

The parameter Γ_{gap} is a temperature broadening factor introduced to avoid a discontinuity in the absorption spectrum at E_g . In principle, we should include separate contributions from the three valence bands, but to keep the model tractable, we use a single expression. Absorption by excitons is described by a Lorentzian line-shape [26, 34, 35] (equation 6.5). The linewidth of the transition is proportional to Γ_{exc} .

$$\alpha_{exciton,i} \propto \frac{1}{(E - E_{exc,i})^2 + \Gamma_{exc,i}} \quad (6.5)$$

In the following we will assume that the probability of observing luminescence from an exciton created in the depletion layer is the same as in the field-free region (we will show later that this is not entirely the case). The direct band-band absorption is, of-course, influenced by the width of the charge separation layer in which absorption does not lead to luminescence, but to photocurrent. This causes a loss term in the photoluminescence intensity of the form $e^{-\alpha W}$, W being the width of the charge separation layer ($W_{depl} + L_p$). Note that this is an approximation of the Gärtner equation (Equation 4.3), that only applies if L_p is small with respect to $1/\alpha$. Since $1/\alpha$ is typically of the order of 0.1-10 μm [5, 9], and $L_p \approx 10$ nm (see fig. 6.8), this assumption is reasonable, but becomes invalid when the absorption coefficient is high (far above E_g). We furthermore assume that absorption deeper than a certain length d , does not lead to luminescence. This is caused by non-radiative decay due to the high defect density deep in the

epitaxial layer (close to the interface with the AlN, and the sapphire) and the finite thickness of the epitaxial layer (1-2 μm). This consideration leads to a loss term of the form : $1 - e^{-\alpha d}$. Equation 6.6 gives the photoluminescence intensity as a function of excitation photon energy. The c 's in this equation are constants that take into account the probability of observing photoluminescence from the different excitonic absorptions, relative to the band-band absorption. From absorption measurements it is known that three excitons can contribute to the overall spectrum (see Fig. 6.1). In principle, the excitonic absorption should be included in the $1 - e^{-\alpha d}$ term and the $e^{-\alpha W}$ term. However, should we do this, the model becomes very complicated, since we will then need to calculate the complete absorption spectrum. To keep the model manageable, we separate the excitonic contributions from the band-band contribution.

$$I_{\text{PL}} \propto \sum_i c_{exc,i} \alpha_{exc,i} + [1 - e^{-\alpha_{dir} d}] e^{-\alpha_{dir} W} \quad (6.6)$$

Figure 6.10 shows that a fit of a photoluminescence excitation spectrum to equation 6.6 is excellent from 3.35 to 3.7 eV. Above this energy the fit deviates from the measured values, probably due to the extra transition that is known to occur in GaN at around 4 eV [5], or to the approximation of the Gärtner equation used in the fit. Below 3.35 eV, the fit is less satisfactory because the assumption of the $1 - e^{-\alpha d}$ loss term is probably simplistic at low absorption coefficients; we do not take into account reflection and interference effects. All three excitons are revealed in the fit.

Various parameters can be determined from the fit. We find $E_g = 3.416$ eV, $\Gamma_{gap} = 2.2$ meV, $E_{exc,A} = 3.389$ eV, $E_{exc,B} = 3.410$ eV, $E_{exc,C} = 3.496$ eV. The broadening parameters $\Gamma_{exc,i}$ are about 20 meV for all three exciton peaks. From these values an A exciton binding energy ($E_g - E_{exc,A}$) of 27 ± 1 meV is determined, which is in good agreement with the literature value of 25 meV [34]. Since we simplified the response due to band-band absorption, we cannot determine the binding energies of the other two excitons from the present fits.

In our model we assumed that the excitonic contributions to the spectral response do not depend on the electrode potential. This is however not entirely the case. Figure 6.11 shows the integrated intensity from the excitonic peaks, obtained by fitting the spectra to equation 6.6. At potentials in the vicinity of V_{fb} the contribution of the excitonic process is constant. At electrode potentials more positive than -0.5 V the intensity decreases, becoming constant at around

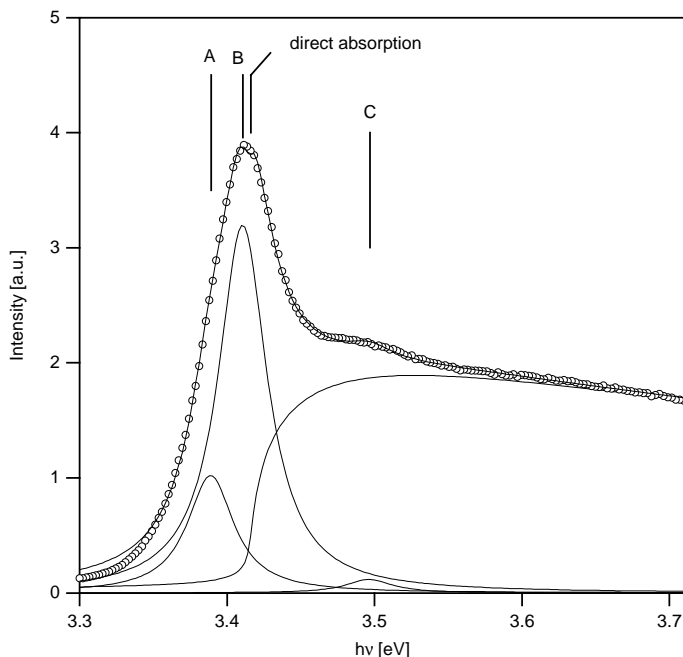


FIGURE 6.10. Fit of the in-situ photoluminescence excitation spectrum at an electrode potential of 1 V. The positions of the exciton transitions and the band-band transition are indicated in the figure. The continuous line through the data points (open circles) is a fit to equation 6.6. The other lines show the band-band transition and the excitonic peaks.

0 V. It must be remarked here that when the electrode is illuminated with higher energy photons (4 eV) a much stronger potential dependence of the photoluminescence (see Fig. 6.8 and 6.11) is observed which is described by equation 6.3. The potential dependence shown in Fig. 6.9 clearly cannot be described by this equation.

Unfortunately, the mathematics needed to explain the precise potential dependence of the luminescence intensity caused by exciton absorption is rather complex, since the probability of ionizing an exciton is field dependent, and the electric field is position dependent. This leads to a probability of observing photoluminescence that is position dependent. Because of this, we will not attempt to describe accurately the influence of electrode potential on the luminescence. We can, however, draw up a simple model. If we take for the probability of excitonic absorption inside the charge separation layer leading to photolumines-

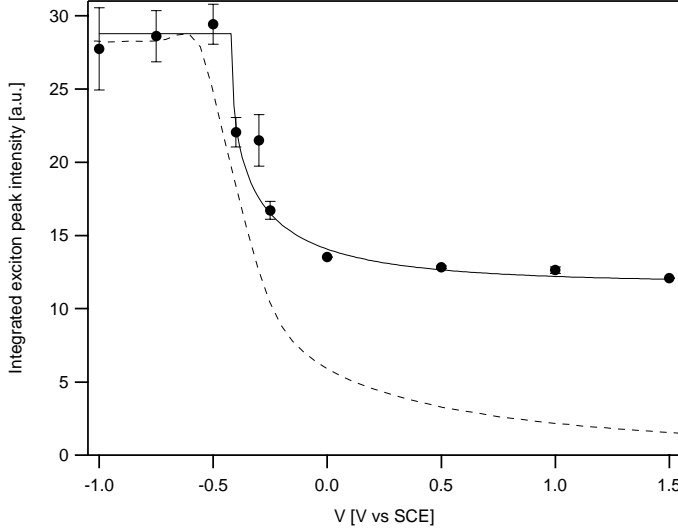


FIGURE 6.11. Integrated intensity of the exciton related peaks (obtained by fitting the spectra shown in figure 6.9 to equation 6.6) as a function of applied potential. The potential dependence of the yellow luminescence under excitation with 4.0 eV light is shown as a reference (see Fig. 6.8).

cence a constant P , the photoluminescence due to excitons coming from the charge separation layer will be proportional to: $P(1 - \exp(-\alpha W))$. The luminescence intensity coming from deeper than the charge separation layer is proportional to: $\exp(-\alpha W)$. Combination of the two terms leads to :

$$\frac{I_{PL}}{I_{PL,max}} = (1 - P)e^{-\alpha W} + P \quad (6.7)$$

The continuous line in figure 6.11 shows a fit to this equation. The experimental data are well described by this crude model, notwithstanding the fact that we totally neglect the electric field dependence of the ionization probability of the exciton. From the fit it follows that P is about 0.4. Since the excitons have a certain probability of becoming ionized, a contribution from excitonic absorption is also expected in the photocurrent spectra. In section 6.4 it was shown that, at large band bending there is a considerable sub bandgap photocurrent. To illustrate this, figure 6.7 includes a calculated photocurrent spectrum based on the assumption that only the band-band transition contributes to the pho-

to current. It is clear that, especially at positive potentials, the photocurrent is markedly higher than expected. Creation of excitons inside the charge separation layer can very likely lead to photocurrent.

6.6 Conclusions

In this chapter, results of *in-situ* photoluminescence and photoelectrochemical experiments on the GaN/electrolyte interface are reported. The capacitance of the GaN/electrolyte interface obeys the Mott-Schottky relationship, indicating that a depletion layer is formed inside the material. From an analysis of the photocurrent-potential curve under illumination with 4.0 eV light a hole diffusion length of 10 nm was estimated. The photoluminescence using the same excitation source is determined entirely by the width of the depletion and diffusion layer. Furthermore, the dependence of the photoluminescence yield on the photon energy of the exciting light was studied. In these spectra, clear evidence for excitonic absorption is observed. Variation of the electrode potential proved to be invaluable in distinguishing between direct free electron-hole pair generation and exciton creation. The spectra show the presence of the three known excitons in GaN. The exciton binding energy is determined to be 27 ± 1 meV.

Appendix: porous GaN

During the course of the measurements described in the present chapter, a rather serendipitous discovery was made that GaN could be made porous by anodic etching. Figure 6.12 shows the surface of an as-grown GaN. The small dark spots are micro-pipes that are often observed on gas phase grown wurtzite semiconductors [16]. Fig. 6.13a shows the surface of GaN after prolonged illumination with UV (4.0 eV) light in a 0.5 M H_2SO_4 solution containing 10 % v/v ethanol under continuous cycling of the potential between -1 and 2 V. The layer has clearly become porous. This does not happen when the solution does not contain ethanol. Figure 6.13b shows the porous layer at a higher magnification. It is clear that the structures are very small ($< 50\text{nm}$). Quantum confinement effects were not observed in the photoluminescence emission spectrum. The photoluminescence excitation spectrum shows a slight shift towards higher energies. This can be due to a decrease in the probability that exciton absorption leads to luminescence. The chemistry of the etching process is still obscure. One would expect that ethanol would lead to stabilization of the photocurrent (the reason it was added to the solution) because it can be oxidised to ethanoic acid. Strangely enough, the opposite seems to happen.

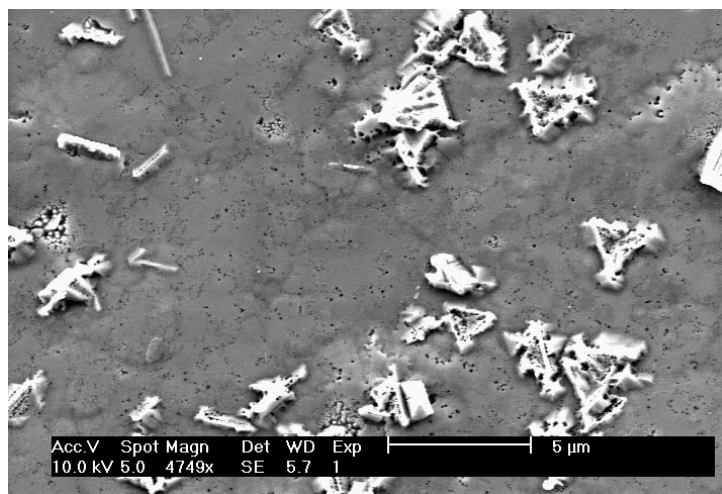


FIGURE 6.12. SEM micrograph of an unetched GaN layer. The dark spots are micro-pipes, that probably extend throughout the epitaxial layer.

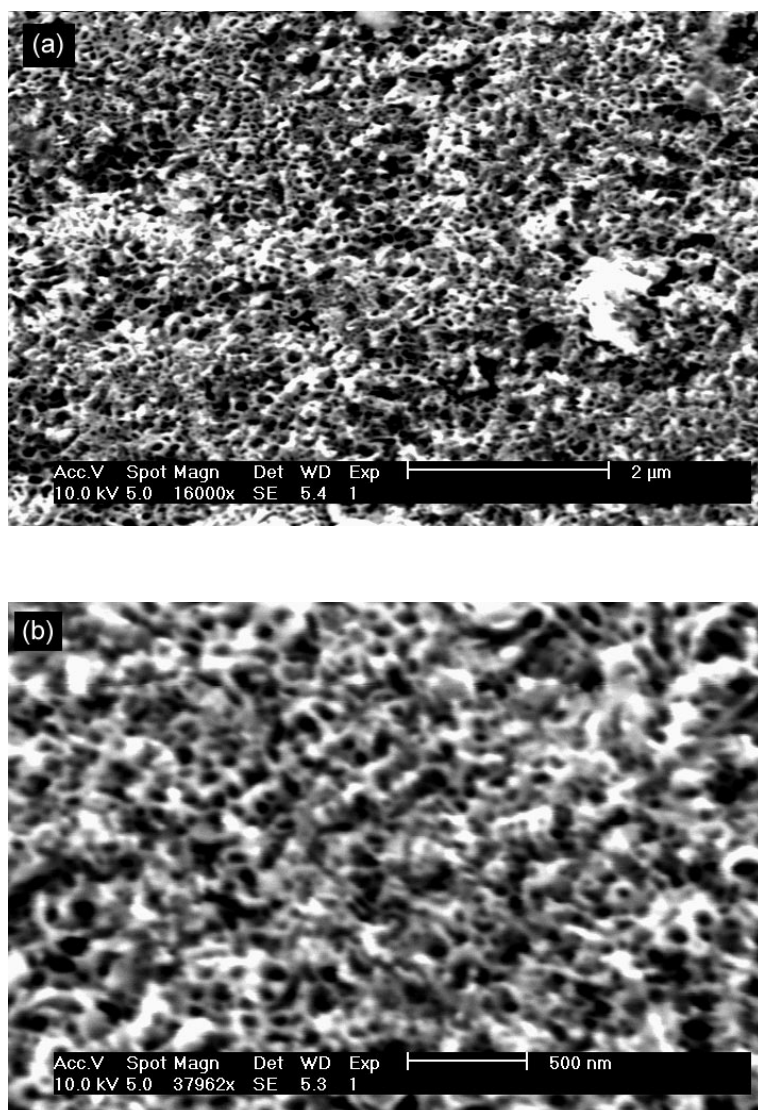


FIGURE 6.13. SEM micrographs of n-GaN that was exposed to prolonged illumination with UV light in 0.5 M H_2SO_4 / ethanol 10:1

References

- [1] S. Strite and H. Morkoç, *J. Vac. Sci. Techn. B* **10**, 1237 (1992).
- [2] J. I. Pankove, E. A. Miller, and J. E. Berkeyheiser, *RCA Rev.* **32**, 383 (1970).
- [3] G. Fasol, *Science* **272**, 1751 (1996).
- [4] M. P. Mack, A. C. Abare, M. Aizcorbe, P. Kozodoy, S. Keller, U. Mishra, L. A. Coldren, and S. P. DenBaars, *Mater. Res. Soc. Internet J.* **2**, Article 41 (1997), available at : <http://nsr.mij.mrs.org/2/41/>.
- [5] J. F. Muth, J. Lee, I. K. Shmagin, R. M. Kolbas, H. C. Jr., B. P. Keller, U. K. Mishra, and S. P. DenBaars, *Appl. Phys. Lett.* **71**, 2572 (1997).
- [6] M. Smith, J. Y. Lin, H. X. Jiang, and M. A. Khan, *Appl. Phys. Lett.* **71**, 635 (1997).
- [7] E. F. Schubert, I. D. Goepfert, W. Grieshaber, and J. M. Redwing, *Appl. Phys. Lett.* **71**, 921 (1997).
- [8] K. Kornitzer, K. Thonke, R. Sauer, M. Mayer, M. Kamp, and K. J. Ebeling, *J. Appl. Phys.* **83**, 4397 (1998).
- [9] A. J. Fischer, W. Shan, J. Song, Y. C. Chang, R. Horning, and B. Goldenberg, *Appl. Phys. Lett.* **71**, 1981 (1997).
- [10] S. S. Kocha, M. W. Peterson, D. J. Arent, J. M. Redwing, M. A. Tischler, and J. A. Turner, *J. Electrochem. Soc.* **142**, L238 (1995).
- [11] C. Youtsey, I. Adesida, and G. Bulman, *Appl. Phys. Lett.* **71**, 2151 (1997).
- [12] C. Youtsey, I. Adesida, and G. Bulman, *Electron. Lett.* **33**, 2 (1997).
- [13] S. Yoshida, *J. Cryst. Growth* **181**, 293 (1997).
- [14] M. Ohkubo, *Jpn. J. Appl. Phys.* **36**, L955 (1997).
- [15] M. Seelmann-Eggebert, J. L. Weyher, H. Obloh, H. Zimmerman, A. Rar, and S. Porowski, *Appl. Phys. Lett.* **71**, 2635 (1997).
- [16] H. Morkoç, S. Strite, G. B. Gao, M. E. Lin, B. Sverdlov, and M. Burns, *J. Appl. Phys.* **76**, 1363 (1994).
- [17] F. Mansfeld, S. Lin, C. Chen, and H. Shih, *J. Electrochem. Soc.* **135**, 906 (1988).
- [18] D. C. Reynolds, D. C. Look, B. Jogai, V. M. Phanse, and R. P. Vaudo, *Sol. St. Comm.* **103**, 533 (1997).
- [19] J. I. Pankove and J. A. Hutchby, *J. Appl. Phys.* **47**, 5387 (1976).
- [20] H. Liu, J. G. Kim, M. H. Ludwig, and R. M. Park, *Appl. Phys. Lett.* **71**, 347 (1997).
- [21] P. Hacke and H. Okushi, *Appl. Phys. Lett.* **71**, 524 (1997).
- [22] T. Monteiro, E. Pereira, M. R. Correia, C. Xavier, D. Hofmann, B. K. Meyer, S. Fischer, A. Cremades, and J. Picqueras, *J. Lumi.* **72-74**, 696 (1997).
- [23] I.-H. Lee, I.-H. Choi, C. R. Lee, and S. Noh, *Appl. Phys. Lett.* **71**, 1359 (1997).
- [24] H. M. Chen, Y. F. Chen, M. C. Lee, and M. S. Feng, *Phys. Rev. B* **56**, 6942 (1997).
- [25] K. Saarinen, T. Laine, S. Kuisma, J. Nassilä, P. Hautojärvi, L. Dobrzynski, J. M. Baranowski, K. Pakula, R. Stepeniewski, M. Wodjak, A. Wysmolek, T. Suski, M. Leszczynski, I. Grzegory, and S. Porowski, *Phys. Rev. Lett.* **79**, 3030 (1997).

-
- [26] J. I. Pankove, *Optical processes in semiconductors* (Dover publications Inc., New York, 1975).
 - [27] H. G. Grimmeiss and B. Monemar, J. Appl. Phys. **41**, 4054 (1970).
 - [28] R. Dingle and M. Ilegems, Solid State Commun. **9**, 175 (1971).
 - [29] R. Dingle, D. D. Sell, S. E. Stokowski, and M. Ilegems, Phys. Rev. B **4**, 1211 (1971).
 - [30] Y. P. Varshni, Physica **34**, 149 (1967).
 - [31] F. Willig, K. Bitterling, K.-P. Charlé, and F. Decker, Ber. Bunsenges. Phys. Chem. **88**, 374 (1984).
 - [32] F. Willig, Ber. Bunsenges. Phys. Chem. **92**, 1312 (1988).
 - [33] W. W. Gärtner, Phys. Rev. **116**, 84 (1959).
 - [34] W. Liu, M. F. Li, S. J. Chua, Y. H. Chang, and K. Uchida, Appl. Phys. Lett. **71**, 2511 (1997).
 - [35] R. J. Elliott, Phys. Rev. **108**, 1384 (1957).

Samenvatting

De ontwikkeling van halfgeleidertechnologie heeft een enorme invloed op de ontwikkeling van de samenleving gehad in de laatste tientallen jaren. Silicium gebaseerde geïntegreerde circuits hebben hun weg gevonden naar een grote variëteit aan huishoudelijke apparaten zoals magnetrons, wasmachines, hifi apparatuur en zelfs stofzuigers. Ze worden onder andere toegepast in auto's, in mobiele telefoons en in videocamera's. Het meest sprekende voorbeeld van de halfgeleider revolutie is wel de personal computer. Toenemende miniaturisatie heeft het mogelijk gemaakt dat de hedendaagse PC's krachtiger zijn dan de supercomputers van tien jaar geleden. De ontwikkeling van de halfgeleider laser heeft belangrijke technologische innovaties zoals de compact disc mogelijk gemaakt. Een zeer belangrijke toepassing van halfgeleiders is de omzetting van zonnelicht. Er wordt wereldwijd gestreefd naar de vervanging van fossiele brandstoffen door schonere alternatieven. Zonnecellen op basis van halfgeleiders zijn in staat om goedkoop en schoon energie te leveren.

Ondanks de grote toepassingsmogelijkheden van silicium heeft dit materiaal belangrijke nadelen. De smalle indirecte bandafstand (1.1 eV) maakt het minder geschikt voor licht emitterende elementen, en voor hoge temperatuur elektronica. Tevens is het zeer gevoelig voor chemische invloeden.

Betere materialen zijn nodig voor het inzetten van elektronica in agressieve omstandigheden. Door verbeteringen in kristalgroeitechnieken zijn recentelijk een aantal grote bandafstand halfgeleiders beschikbaar gekomen die chemisch zeer stabiel zijn. Enkele voorbeelden zijn diamant, silicium carbide en de III-V nitrides (GaN, AlN, InN). Deze materialen zijn veelbelovend [1], en in het laboratorium zijn al vele toepassingen gerealiseerd. Een CCD (Charge Coupled Device) is reeds gefabriceerd in SiC [2]. Een dergelijk device kan bijvoorbeeld worden toegepast in UV astronomie. Al enige tijd zijn blauw licht emitterende diodes gebaseerd op SiC commercieel beschikbaar [3]. Diamant kan mogelijk worden toegepast als zogenaamde "koude kathode" in vlakke display panelen [4, 5]. Met de III-V nitrides kunnen stabiele diode lasers in het blauw en het UV vervaardigd worden [6, 7]. Dergelijke lasers zijn van groot belang voor de verdere vergroting van de informatiedichtheid van optische informatiedragers (CD's, DVD's e.d.).

Hoewel de chemische stabiliteit van deze materialen een groot voordeel is voor toepassingen is het een groot nadeel voor de verwerking. Normale processtappen zoals schoonmaken, etsen, polijsten en metallisering zijn moeilijk. Het is duidelijk dat er meer informatie nodig is over de fysische eigenschappen en de oppervlaktechemie van deze materialen. Dit proefschrift beschrijft een (foto)elektrochemische studie van deze onderwerpen voor drie grote bandafstand halfgeleiders: diamant, silicium carbide en gallium nitride. Deze hebben bandafstanden van respectievelijk 5.54, 3.02 en 3.41 eV.

In hoofdstuk 2 wordt de elektrodekinetiek van één-kristallijne diamant elektrodes in oplossingen van simpele (één electron) redox systemen beschreven. De diamantelectrodes werden vervaardigd uit homoepitaxiale CVD lagen. Omdat diamant een zeer grote bandafstand heeft kan men verwachten dat ladingsuitwisseling met de oplossing moeilijk is. Dit blijkt niet het geval te zijn. De stroom-potentiaal curves lijken op die van metaal elektrodes. Het gedrag valt te verklaren wanneer ladingsoverdracht geholpen wordt door de aanwezigheid van oppervlaktetoestanden. In hoofdstuk 3 wordt de kinetiek beter bestudeerd met behulp van elektrische impedantiespectroscopie.

In hoofdstuk 4 wordt een photoelektrochemische studie van SiC elektrodes in waterige oplossingen gepresenteerd. Uit het verband tussen grensvlak-capaciteit en potentiaal kan met grote precisie de doteringsdichtheid worden bepaald. Uit het verband tussen de vlakke band potentiaal en de pH van de elektrolytfase kan worden afgeleid dat aan het oppervlak Si-OH groepen voorkomen die protonen uitwisselen met de oplossing. Verder kan uit fotostroom-potentiaal en gemoduleerde fotostroom (IMPS) metingen de diffusielengte van minderheidsladingsdragers worden bepaald. Voorts blijkt het zeer goed mogelijk om uit de fotostroom als functie van de energie van het licht het absorptiespectrum van SiC te bepalen.

Door te anodiseren in HF oplossingen kan SiC sterk poreus worden gemaakt. In hoofdstuk 5 worden resultaten gepresenteerd van metingen aan poreus SiC. SEM foto's laten zien dat een zeer poreuze laag verkregen kan worden met structuren met dimensies in de orde van 50 nm. De fotostroom opbrengst voor licht geabsorbeerd in de indirecte overgang en voor sub-bandafstand licht van een poreus SiC/elektrolyt diode is spectaculair verbeterd ten opzichte van die van een vlakke diode.

Tenslotte worden in hoofdstuk 6 resultaten beschreven van fotoelektrochemische metingen aan GaN elektrodes. Allereerst wordt de potentiaal distributie aan het halfgeleider/elektrolyt grensvlak bepaald met behulp van fotoluminescentie

en fotoelektrochemische experimenten. Met behulp van deze resultaten kunnen *in-situ* fotoluminescentie excitatie spectra begrepen worden. Uit deze spectra blijkt duidelijk dat exciton absorptie bij kamertemperatuur optreedt. Door de karakteristieke eigenschappen van het halfgeleider/elektrolyt systeem kunnen de excitonische absorptieprocessen onderscheiden worden van de band-band absorptie.

Referenties

- [1] C. Jongeneel, *Elektronici houden van diamant* (Volkskrant, 20 december, 1997).
- [2] S. T. Sheppard, M. R. Melloch, and J. J. A. Cooper, IEEE Elec. Dev. Lett. **43**, 1 (1996), see the device at: <http://yake.ecn.purdue.edu/~shepman/SiC-CCD.html>.
- [3] <http://www.cree.com>.
- [4] P. Ball, Nature **381**, 116 (1996).
- [5] K. Okano, S. Koizumi, S. R. P. Silva, and G. A. J. Amaratunga, Nature **381**, 140 (1996).
- [6] M. P. Mack, A. C. Abare, M. Aizcorbe, P. Kozodoy, S. Keller, U. Mishra, L. A. Coldren, and S. P. DenBaars, Mater. Res. Soc. Internet J. **2**, Article 41 (1997), available at : <http://nsr.mij.mrs.org/2/41/>.
- [7] G. Fasol, Science **272**, 1751 (1996).

List of publications

- ☉ J. van de Lagemaat, G.Z. Cao, G. Janssen, D. Vanmaekelbergh, and J.J. Kelly, "*Electrochemical Investigation of single crystalline semiconducting CVD diamond films*", *Electrochem. Soc. Proc.* **95-21**, 103 (1995)
- ☉ D. Vanmaekelbergh, J. van de Lagemaat, R.E.I. Schropp, "*Observation and explanation of quantum efficiencies exceeding unity in amorphous silicon solar cells*", *Sol. Ener. Mat. Sol. Cells* **41/42**, 537 (1996).
- ☉ J. van de Lagemaat, M. Plakman, D. Vanmaekelbergh, J.J. Kelly, "*Enhancement of the light-to-current conversion efficiency in an n-SiC/solution diode by porous etching*", *Appl. Phys. Lett.* **69**, 2246 (1996). (Chapter 5 of this thesis)
- ☉ D. Vanmaekelbergh, F. Iranzo-Marín, J. van de Lagemaat, "*Transport of photogenerated charge carriers through crystalline GaP networks investigated by intensity modulated photocurrent spectroscopy*", *Ber. Bunsenges. Phys. Chem.* **100**, 616 (1996)
- ☉ D. Vanmaekelbergh, P.E. de Jongh and J. van de Lagemaat, "*Dynamics and transport of photogenerated charge carriers in nanostructured semiconductor electrodes*", *Electrochem. Soc. Proc.*, **97-20**, 72 (1997)
- ☉ J. van de Lagemaat, D. Vanmaekelbergh, J.J. Kelly, "*Photoelectrochemical Characterization of 6H-SiC*", *J. Appl. Phys.* **83**, 6089 (1998) (chapter 4 of this thesis)
- ☉ D. Vanmaekelbergh, J. van de Lagemaat, R.E.I. Schropp, F. Cardon, "*Thermally enhanced quantum efficiency in hydrogenated amorphous silicon p-i-n photodiodes studied by Intensity Modulated Photocurrent Spectroscopy*", *Phil. Mag. B.*, accepted for publication.
- ☉ J. van de Lagemaat, D. Vanmaekelbergh, J.J. Kelly, "*Electrochemistry of homoepitaxial CVD diamond. Part I: Energetics and electrode kinetics in aqueous electrolytes*", *J. Electrochem. Soc.* submitted for publication. (Chapter 2 of this thesis)

- © J. van de Lagemaat, D. Vanmaekelbergh, J.J. Kelly, "*Electrochemistry of homoepitaxial CVD diamond Part II: Mechanism of electron exchange with simple redox systems*", J. Electrochem. Soc. submitted for publication. (Chapter 3 of this thesis)
- © J. van de Lagemaat, D. Vanmaekelbergh, J.J. Kelly, "*Excitonic effects in the photoluminescence of GaN studied at the semiconductor/electrolyte interface*", to be published. (Chapter 6 of this thesis)

Tenslotte

Als ik dit schrijf is het 23:24. Ergens tijdens het grote stress gebeuren dat proefschrift schrijven wordt genoemd. Waarschijnlijk zal ik dit niet nu in een keer afschrijven (aangezien je het enige stuk van een proefschrift dat bijna iedereen leest goed moet overdenken ;)). Ik denk aan alles wat er gebeurd is in 4 jaar. Kan ik me herinneren hoe de situatie 4 jaar geleden was ? Kan ik me herinneren hoe de jaren tot op dit moment zijn verlopen ? Kan ik me herinneren wat er voor die tijd gebeurd is ? Als ik me in beginsel moet beperken tot de dingen die met mijn promotie te maken heb moet ik beginnen vijf jaar geleden. Mijn klein bijvakje bij Erik Meulenkamp over hypochloriet reductie aan GaAs. Dit was mijn introductie in de halfgeleider electrochemie. Erik, bedankt voor de zeer enthousiasmerende inleiding. Tevens voor het mij leren van de beginselen van IMPS. Het was het IMPSen dat waarschijnlijk het enthousiasme in Daniël opwekte om me te vragen voor een IMPS onderzoek naar amorf silicium zonnecellen. Een onderwerp waarvan we de genoegens en de frustraties nog tot ver in mijn promotie hebben mogen smaken. Als ik dit schrijf is het artikel nog steeds niet gepubliceerd (Red. inmiddels heb ik per email vernomen dat het bij de drukker is. Wellicht is het wel gepubliceerd voordat ik ben gepromoveerd!). Op Daniël kom ik later nog terug.

Dit was ook ongeveer de tijd dat Ben op het lab was. Ik kan me nog urenlange discussies over allerlei onderwerpen bedenken. Ik heb voor weinig mensen zoveel respect als voor jouw gekregen, Ben. Je onzekerheden over de te volgen weg tot de oplossing van het probleem, je vaak geniale oplossingen voor praktische en theoretische problemen, en de snelheid waarmee je in de enorme stapels papier precies het goede artikel kon vinden. Mijn stapels zijn nog niet half zo hoog, maar ik doe er zeker twee keer zo lang over. Ik heb me vaak laten inspireren door de plakband/afgeknipt vergiet oplossingen die ik vaak nog jaren later in laatjes in het lab vond.

Het is inmiddels al weer een aantal dagen later dat ik dit schrijf (2 juli). Inmiddels is het proefschrift af, en morgenochtend breng ik het naar de drukker. Alleen dit laatste stuk moet nog gebeuren. Wellicht het moeilijkste stuk omdat bijna iedereen het leest. Worden de mensen boos als ik ze vergeet? Ik zie nu net dat ik nog vier pagina's moet volschrijven om aan een meervoud van 16 pagina's te komen.

Ik heb enorm veel te danken aan John. Niet alleen als promotor, maar ook als enthousiasmerende factor. Af en toe was het “laissez-faire” management niet de allerbeste oplossing voor mij, maar aan de andere kant heeft de enorme vrijheid ook duidelijk vruchten afgeworpen. Ik denk dat ik een typisch voorbeeld ben van de U-curve promovendus; één van je theorieën. Ik vond het geweldig met je samen te werken, en hoop dat in de toekomst nog af en toe voort te zetten (al die ongepubliceerde data).

De andere grote kracht achter het geheel was Daniël. Je zei gisteren dat ik geen dankwoord hoefde te schrijven, en dat de vakgroep eerder mij voor alle computerhulp zou moeten bedanken. Ik ben het daar niet mee eens. Ik heb meer te danken aan jouw begeleiding, dan jij aan mijn computerhulp. Dat laatste is namelijk (voor mij althans) tamelijk triviaal. Bovendien heb ik een hekel aan computers. Ik heb vaak genoten van onze discussies tijdens werkbijeenkomsten (naar ik later hoorde onze vakgroepsgenoten niet erg), en het zogenaamde Daniël effect. Dit is een op de vakgroep zeer bekend effect, en komt op het volgende neer. De promovendus is in discussie met Daniël en brengt een idee naar voren: “zou het niet kunnen dat ...”. Daniël: “Nee natuurlijk niet, lees nog eens wat boeken over basiselektrochemie!.” Vervolgens twee dagen later komt Daniël naar de promovendus toe: “Zeg ... , zou het niet zo kunnen zijn dat ...”. Hier moet dan wel bij gezegd worden dat Daniël dan wel een bijna compleet uitgewerkt model al heeft. Dit soort communicatiestoornissen (en zeker ook de omgekeerde vorm trouwens!) zijn vaak voorgekomen. Ik hoop je in de toekomst nog vaak te zien, en je zeker ook een keer in Denver te ontvangen voor een trip door Amerika.

Geert, bedankt voor al die keren dat we samen koffiedronken en M&M's aten, voor de lol tijdens de reis naar Amerika, voor je relativiserende levenshouding en voor het zijn van een vriend.

Francesco, I loved to work with you in the time you were a post-doc in our lab. The work we and Mariska and Daniël did together was wonderful, but alas it did not end up in this thesis. It was lovely to visit you and your parents in Barcelona and Tarragona. I and Mariska hope to do it again sometime this year. It is very nice to have you as a friend, and as a witness on my wedding. If you have the time please come and visit me in the states.

René, ik vindt het te gek je als vriend, als medestudent, en zelfs als collega mee te maken. Ik heb zeer veel lol met je gehad, en hoop dat in de toekomst voort te zetten. Helaas zullen we niet meer elke dag met elkaar op kunnen fietsen. Verder wil ik Petra bedanken voor het tafeltennisen en de vele “mopper-gesprekken”.

Je zult het niet geloven, maar er zijn wetenschappelijke gebieden waarin ik tegen je op kijk. De rest van de mensen die meegeweest zijn op het wandeltochtje in Zwitserland: Ard, Mathilde, Karin, Ris, Detlef, en Wicher, bedank ik ook voor de heerlijke vakantie.

Mijn verdere collega's op het lab en al die studenten die hier in de loop der tijd zijn gestationeerd geweest wil ik bedanken voor de leuke sfeer en voor de roddels. Monique, Hilda, en Arjan als kamergenoten voor de rust, en het telefonist(e) spelen. Voorts wil ik Hans Ligthart bedanken voor al zijn technische hulp, zijn enorme inzet en tevens zijn humor. Johan van der Linden wil ik bedanken voor de elektrotechnische kennis, en al de informatie over de geschiedenis van het lab. Alle andere technici ben ik uiteraard ook zeer dankbaar. Onze secretaresses, Jessica en Clarien ben ik dankbaar voor de gezelligheid en de roddels, en natuurlijk de secretariële ondersteuning. Jessica in het bijzonder voor het regelen van taart op onze verjaardagen. Mijn studente Maaïke Plakman ben ik dankbaar voor het doen van leuke metingen aan poreus SiC. De resultaten van je onderzoek zitten verwerkt in hoofdstuk 5.

Ik wil ook alle mensen van het lab van Ris bedanken voor hun vriendschap met Ris, en mij.

I would like to thank the people of wavemetrics for developing Igor. This excellent program has been instrumental in finishing this thesis. Thanks for letting me betatest your software. Often the betaversion contained just what I needed, when I needed it.

Voorts zijn er een heleboel mensen die hebben gezorgd dat de materialen die in dit proefschrift gebruikt worden, er kwamen of bruikbaar gemaakt werden. Ik zal ze hieronder opnoemen: G. Verspui van het Philips Centre for Fabrication Technology voor de SiC samples, C.J. Geenen van Philips Research voor het maken van SEM-opnamen, H.C. Donkersloot (Philips Research) voor het maken van Ohmse contacten op onze SiC wafers en op onze diamanten. Voorts bedank ik G. Janssen en G.Z. Cao voor het maken van de diamant CVD lagen, and J.L. Weyher for providing us with the GaN layers.

Nu ik het lab zo'n beetje gehad heb, kom ik in andere regionen. Van mijn familie wil ik Dick, Tara, en Feyona bedanken voor het naast familie zijn voornamelijk vrienden zijn. Ali, Jaap en Angelique wil ik bedanken voor al de steun de afgelopen tientallen jaren. En de rest van mijn familie, en natuurlijk mijn pas aangeworven extra familie, wil ik natuurlijk ook bedanken.

De jongens van de warande helpdesk (Jeroen en de rest) wil ik bedanken voor de nodige afleiding en ergernis (niet werkende computers) het afgelopen jaar.

Mijn huisgenoten voor het zo tolerant zijn over mijn laksheid wat betreft schoonmaakbeurten, en voor de gezellige spelletjesavonden, samen eten etc.

Paul, John en Gido ben ik oneindig dankbaar voor het samen muziek maken, de nachten in het fort voor het opnemen van PAT! en voor jullie vriendschap. Ik ga jullie en de muziek missen.

Paul is een bijzonder geval. Had je drie jaar geleden niet plots voor mijn deur gestaan met de vraag of ik met je muziek wilde maken, dan was er waarschijnlijk niet veel van dit proefschrift terecht gekomen. Het nachtenlange praten over de wereld, de natuur, mensen en over muziek zal ik nooit vergeten. Je bent mijn beste vriend geworden, en ik weet zeker dat ik jou bijna nog het meest ga missen aan de andere kant van de oceaan. Ook Cis zal ik enorm missen. Ik hoop dat jullie snel eens langskomen, dan kan ik wat terugdoen voor die laatste weken dat jullie me in leven hebben gehouden met vitaminerijk voedsel. Ik weet al zeker dat ik vaak langs zal komen in Andijk om eens goed uit te rusten, en wat met hout en muziekinstrumenten te spelen.

Ik wil ook graag Henkie, Winnetou, Pingu en Galileo bedanken voor hun liefde.

Als laatste, maar verreweg de belangrijkste noem ik Ris. Al sinds 1990 vriendjes, vanaf de eerste paar dagen in de collegebanken. De verliefdheid is eigenlijk nooit opgehouden. Sinds kort zijn we zelfs getrouwd, en miljoen blijft maar groeien. Als ik terugdenk aan al die leuke dingen die we meegemaakt hebben, aan wat je allemaal voor me hebt gedaan schiet mijn gemoed enigszins vol. Ik hoop nog veel meer met je mee te maken in de toekomst, in dit enorme avontuur dat leven wordt genoemd. Baboea Rissie: 1♥⁶.



Curriculum Vitae

De auteur van dit proefschrift werd geboren in Schoonhoven op 8 mei 1972. In 1990 haalde hij het VWO diploma aan de Libanon Scholengemeenschap te Rotterdam. In dat zelfde jaar verhuisde hij naar Utrecht om te beginnen met de studie Scheikunde. In 1991 behaalde hij het propedeuse diploma. Zijn onderzoeksjaar bestond uit drie onderdelen: twee bijvakken en een hoofdvak. Voor zijn eerste bijvak deed hij onderzoek in de vakgroep gecondenseerde materie naar de kinetiek van hypochloriet-reductie aan GaAs. Zijn tweede bijvak werd gedaan aan de vakgroep anorganische chemie, en behelsde een UHV-studie naar de oxidatie en reductie kinetiek van koper-nanodeeltjes op silicium. Tijdens zijn hoofdvak deed hij onderzoek naar het transport van ladingsdragers in amorf silicium zonnecellen met behulp van gemoduleerde fotostroom spectroscopie. Dit onderzoek was een samenwerking van de werkgroep gecondenseerde materie met de vakgroep Atoom en Grenslaag Fysica (AGF). Dit onderzoek heeft 2 publicaties opgeleverd (zie pagina 119). Het Doctoraal-examen werd afgelegd op 28 augustus 1994.

Per 1 september 1994 is hij vervolgens begonnen als OIO gefinancierd door SON/NWO binnen de werkgroep gecondenseerde materie van het Debye Instituut, Universiteit Utrecht. Hier deed hij onderzoek naar de elektrochemie van grote bandgap halfgeleiders. De belangrijkste resultaten hiervan zijn in het voorliggende proefschrift vastgelegd. Tevens deed hij onderzoek naar de dynamica van ladingsdragers in poreus gallium phosphide.

Delen van het werk werden gepresenteerd tijdens de 188th meeting van de Electrochemical Society, Chicago, 1995, de Third European Workshop on Electrochemical Processing of Semiconductors, Paris, France, 1996, en de 192nd meeting of the Electrochemical Society and 48th annual meeting of the International Society of Electrochemistry, Paris, France, 1997. Naast het onderzoek begeleidde hij derde- en vierdejaars studenten bij experimenteel onderzoek, eerstejaars studenten bij hun synthese en analysepractica, en tweedejaarsstudenten bij hun Fysisch Chemisch Meten practica.

*There once was a man who said : “ God
Must think it exceedingly odd
If he finds that this tree
Continues to be
When there’s no one about in the Quad.”*

Monsignor Ronald Knox

*“Dear Sir, your astonishment’s odd.
I am always about in the Quad.
And that’s why the tree
Will continue to be
Since observed by yours faithfully, GOD.”*

unknown author